Title
Fundamental Studies on Unique Doping Mechanisms in Organic Semiconductors

Author
Cao, David Xi

Publication Date
2020

Peer reviewed|Thesis/dissertation

UNIVERSITY OF CALIFORNIA

Santa Barbara

Fundamental Studies on Unique Doping Mechanisms in Organic Semiconductors

A dissertation submitted in partial satisfaction of the

requirements for the degree Doctor of Philosophy

in Chemistry

by

David Xi Cao

Committee in charge:

Professor Thuc-Quyen Nguyen, Chair

Professor Michael Chabinyc

Professor Martin Moskovits

Professor Lior Sepunaru

June 2020

The dissertation of David Xi Cao is approved.

_____

Michael Chabinyc

_____

Martin Moskovits

_____

Lior Sepunaru

_____

Thuc-Quyen Nguyen, Committee Chair

June 2020

Fundamental Studies on Unique Doping Mechanisms in Organic Semiconductors

by

David Xi Cao

ACKNOWLEDGEMENTS

In the midst of my Ph.D., there were many instances where I wondered if it was worth it. The struggle is not unique—many students experience feelings of doubt and self-worth, especially coming from our time as undergraduate students where hard work translated directly to measurable successes, a correlation that does not always hold up when doing research. In the middle of those moments, I'm so grateful to my parents, who in all seasons continued to encourage me to complete the Ph.D. and supported me with verbal affirmation and coolers full of food. My wife, Susan, was and is an endless well of encouragement and support, often spending late nights with me on the phone from thousands of miles away as I finished up experiments in lab. Even as she pursued her own studies to obtain a PharmD., she found time to talk and comfort me with hugs. She makes me laugh and reminds me to pursue the dreams and paths I feel that God has laid out for me. My grandparents, who have always been there to support me and remind me that things will work out in the end. My friends from college, Tim Tiambeng, Joseph Kim, Bryan Xie, and Gregory Chan, all of whom also pursued some sort of doctoral degree whether philosophical or professional, were also a big source of my emotional support as we pushed and encouraged each other to persevere. My little sister Jessica, the right-brained one in the family, would recommend concerts I should attend in Santa Barbara and brought me peace through music. Through our conversations, she also makes me laugh, and reminds me of life outside of the lab. My friends from church, of which there are many and scattered all over the state, have been steadfast in their support, encouraging me from near and far.

On campus, my Ph.D. would not have been possible with the support of my thesis advisor Prof. Thuc-Quyen Nguyen. I'm grateful for her taking me on in her lab, and for the guidance and direction she has given me these past 5 years. She keeps a well-stocked lab and has provided me with opportunities to present and conduct research abroad. I am also grateful to Prof. Martin Moskovits, who has supported me in my teaching pursuits both formally as my mentor for the certificate in college and university teaching, and informally through serendipitous conversations. Conversations with him were uplifting and reminded me of why I pursued a Ph.D. in the first place. Prof. Gui Bazan, during his time at UCSB, served as a sort of second thesis advisor to me, providing research advice and access to facilities and supplies I needed to complete my work. He's been gracious with his time, making it a point to talk to

me even if it meant while on a walk to another meeting he had. During my advancement exam, my committee member Prof. Michael Chabinyc asked great, probing questions about my research that helped me think more deeply about the underlying processes going on. In hindsight, I wish I had spoken to him more. I am also grateful to Prof. Lior Sepunaru, who stepped up towards the very tail end of my Ph.D. to serve on my thesis committee following Prof. Bazan's departure. His willingness to listen to me, and ask me to speak before he does while maintaining his own metrics for success was very refreshing.

I've also been mentored by many former students and postdocs: Prof. Hung Phan, Dr. Niva Ran, Dr. Zach Rengert, Dr. Sam Collins, Prof. Yuanyuan Hu, Dr. Mike Heiber, Dr. Nate Kirchhofer, Prof. Seojin Ko, Kenny Liao, Dr. Caitlin McDowell, Prof. Takashi Okubo, Dr. Lijiao Ren, Dr. Joachim Vollbrecht, and Dr. Brett Yurash, who have provided me with a huge wealth of technical knowledge and tips during my time here. During my earlier years, I'm particularly indebted a few particular individuals. Hung taught me how to use multiple instruments including the vacuum probe station and the AFM and reminded me "the most important thing when doing AFM is patience". Sam showed a group of us how to clean substrates, use the spin coater, the evaporator, and showed me some data processing procedures on the AFM. Niva was constant in sharing her wealth of knowledge, her connections, and her advice with me, on bus rides to and from our homes downtown. Mike introduced me to Igor Pro, the data processing software used for the figures throughout this thesis and taught me some coding basics. Yuanyuan, whose confidence in my budding AFM skills encouraged me and resulted in my first co-author paper during my Ph.D. Viktor, whose deep fundamental knowledge of physics guided us chemists in our work with impedance spectroscopy and related electrical measurements.

My Ph.D. would not have been possible without the expertise and synthetic collaborative efforts of Matthew Wong, Dr. Cheng-Kang Mai, and Dr. Dirk Leifert. Dr. Cheng-Kang Mai first synthesized CPE-K, the material which I have worked with the most during my time at UCSB. Matthew Wong supported him in his synthetic efforts, and also provided me much of the material I worked with. Dr. Dirk Leifert drove the synthesis and initial studies into Lewis acid doping of various polymers and made grams worth of polymer for our work. I also dabbled in the realm of theoretical chemistry, and had some great discussions with Andrew Rowberg about this, a fellow Ph.D. student and choir colleague. My friend Michael Häggmark

who knows a lot of different things about a whole range of topics would help point me in the right direction when I would be trying to figure out things to which I was unsure where to turn to first. I'm also extremely grateful to instrument facility staff who trained me and oversaw the maintenance and care of shared facilities crucial to my work. Amanda Strom and Rachel Behrens who work in the MRL trained me on the TGA-MS and DSC respectively. Alexander Mikhailovsky helped us keep so many instruments up and running from the UV-vis-nIR, to the evaporator, to computers running LabView, and helped me with a Raman measurement that I wanted to try. Tom Mates trained me on the XPS instrument and entertained my requests for off-the-wall experiments like cooling samples down to −150 °C.

I've also had the privilege of collaborating with scientists abroad, in particular those in the Supramolecular Systems group at Humboldt University in Berlin, Germany. Prof. Norbert Koch was kind enough to agree to let me work with and get training on PES techniques applicable to my work including XPS, UPS and IPES. During my time, I was supervised by Dr. Ahmed Mansour who also taught me about PES techniques and the intricacies that come with working on such equipment, and Dominique Lungwitz, a masters student who ran experiments with us. Dr. Mansour also ensured that I was welcomed by the group and took his lunches with me while I was there.

It's also been a joy to work with my current lab mates—Prof. Viktor Brus, Sangmin Chae, Jirat Chatsirisupachai, Alana Dixon, Zhifang Du, Kelsey Harrison, Jianfei Huang, Akchheta Karki, Erin Lewis, Alexander Lill, Dr. Tung Nguyen, Patchareepond Panoy, Shafket Rasool, Nora Schopp, Max Schrock, Hiba Wakidi, Hao Yang, and Sangcheol Yoon. Each of their unique personalities and perspectives have made the lab a brighter and more joyous place to work. Members of my cohort, Alex and Akchheta, have been a special source of comfort as we shared meals and many of the same experiences together in our journey to our Ph.D.'s. My office mates both past and present, Prof. Viktor Brus, Sangmin Chae, Alana Dixon, Zhifang Du, Sangcheol Yoon, Dr. Brett Yurash, Ben Luginbuhl, Akchheta Karki, Dr. Seojin Ko, Prof. Takashi Okubo, Eunjeong Jeong, Dr. Mike Heiber, Dr. Joachim Vollbrecht, and Carolina Espinoza, have borne intimate witness to my moments of happiness and frustration, and have been a source of support through it all. In particular, I want to thank Prof. Viktor Brus, Dr. Joachim Vollbrecht, and Zhifang Du who are more than happy to be sources of help and distraction when things are not going as planned in lab. Alana Dixon, who brings

brightness and light to our office. Ben Luginbuhl, a deep well of knowledge and expertise on everything from instruments to theory. Carolina Espinoza, who tells truth with grace.

I've also had the privilege of mentoring younger students, both undergraduate and graduate, who have been an inspiration to me as they pushed beyond the boundaries of knowledge first provided to them. I've directly supervised Peter Santiago and Simon Biberger, both of whom are in graduate school now and who have helped me renew my own efforts and interest in my work through their dedication and findings. I've also had the joy of helping many others informally, from the AFM wizard Max who has supplanted my skills on the instrument, to the meticulously detailed and hard-working Carolina now pursuing her own Ph.D., to the kind and eager Eunjeong.

While not directly related to my thesis, I also completed the requirements for the Certificate in College and University Teaching. Throughout that process, I met incredible teacher-scholars such as Prof. Lisa Berry and Dr. Mindy Colin who encouraged me in my pursuit of a teaching career while also providing me with the resources and guidance to succeed. Interacting with them felt like taking a breath of fresh air, helping me to refocus and remain energized in pursuit of my goal to become teaching faculty.

Last but definitely not least, to the community in Santa Barbara and all those who work in it, thank you. Over the years, I have gotten to know quite a few of the SBMTD bus drivers. One time, upon hearing that I'm doing work on renewable energy systems, one of the bus drivers mentioned that what I'm doing is really important. But without the bus drivers faithfully making their rounds at their appointed time, I would not be able to get to campus to do my work. Without truck drivers, we would have no food, fuel, and supplies. Without everyone in the community, there would be no research, and no Ph.D. Thank you all, and let us continue to do our best in our vocations and our lives.

This dissertation was supported by the National Science Foundation (NSF) Graduate Research Fellowship Program (GRFP), the Mananya Tantiwiwat Fellowship, a UC Santa Barbara Regents' Fellowship in Chemistry and Biochemistry, and the U.S. Department of Energy Award No. DE-SC0017659. Through my graduate studies, I was also awarded a travel fellowship from the Dow Materials Institute and the Materials Research Laboratory, and a UCSB Doctoral Student Travel Grant.

VITA OF DAVID XI CAO
June 2020

EDUCATION

Bachelors of Science in Chemistry with Honors. *Cum Laude*. University of California, Irvine, June 2014

Doctor of Philosophy in Chemistry, University of California, Santa Barbara, June 2020 (expected)

PUBLICATIONS

9. **Cao, D. X.,** Yan, H., Brus, V. V., Wong, M. S., Bazan, G. C., Nguyen, T.-Q. Old Technique, New Understanding – How Conductive Atomic Force Microscopy Can Be Used to Visualize Energy Transfer from Bacteria for Microbial Fuel Cells. *Submitted.*

8. **Cao, D. X.,** Leifert, D., Brus, V. V., Wong, M. S., Phan, H., Yurash, B., Koch, N., Bazan, G. C., Nguyen, T.-Q. The Importance of Sulfonate to the Self-doping Mechanism of the Water-Soluble Conjugated Polyelectrolyte PCPDTBT-SO3K. *Mater. Chem. Front. 2020, online*

7. Tsokkou, D., Peterhans, L., **Cao, D. X.,** Mai, C.-K., Bazan, G. C., Nguyen, T.-Q., Banerji, N. Excited State Dynamics of a Self-Doped Conjugated Polyelectrolyte. *Adv. Funct. Mater.* 2019, online.

6. Huang, J., Lee, J., Vollbrecht, J., Brus, V. V., Dixon, A. L., **Cao, D. X.,** Zhu, Z., Du, Z., Wang, H., Cho, K., Bazan, G. C., Nguyen, T.-Q. A High-Performance Solution-Processed Organic Photodetector for Near-Infrared Sensing. *Adv. Mater*. 2019, online.

5. Yurash, B., **Cao, D. X.,** Brus, V. V., Leifert, D., Wang, M., Mansour, A., Lungwitz, D., Dixon, A., Seifrid, M., Santiago, P., Koch, N., Bazan, G. C., Nguyen, T.-Q. Towards Understanding the Doping Mechanism of Organic Semiconductors by Lewis Acids. *Nat. Mater*. 2019, online.

4. Vollbrecht, J., Brus, V. V., Ko, S- J., Lee, J., Karki, A., **Cao, D. X.,** Cho, K., Bazan, G. C., Nguyen, T. Q. Quantifying the Nongeminate Recombination Dynamics in Nonfullerene Bulk Heterojunction Organic Solar Cells. *Adv. Energ. Mater*. 2019, online.

3. Yurash, B., Leifert, D., Reddy, G. N. M., **Cao, D. X.,** Biberger, S., Brus, V. V., Seifrid, M., Santiago, P. J., Köhler, A., Chmelka, B. F., Bazan, G. C., Nguyen, T. Q. Atomic-Level Insight into the Postsynthesis Band Gap Engineering of a Lewis Base Polymer Using Lewis Acid Tris(pentafluorophenyl)borane. *Chem. Mater.* 2019, online.

2. Hu, Y., **Cao, D. X.,** Lill, A. T., Lang, J., Di, Chong-An., Gao, Xike., Sirringhaus, H., Nguyen, T. Q. Effect of Alkyl-Chain Length on Charge Transport Properties of Organic Semiconductors and Organic Field-Effect Transistors. *Adv. Electron. Mater.* **1800175,** 1–8 (2018).

1. Wong, J. L., Higgins, R. F., Bhowmick, I., **Cao, D. X.,** Szigethy, G., Ziller, J. W., Shores, M. P., Heyduk, A. F. Bimetallic iron-iron and iron-zinc complexes of the redox-active ONO pincer ligand. *Chem. Sci.* **7,** 1594–1599 (2015).

AWARDS

2018	Outstanding Service to the Department
2017	ACS Nano Letters Best Oral Presentation, UC Chemical Symposium
2015	Phi Lambda Upsilon Chemistry Honors Society

FELLOWSHIPS AND GRANTS

2018	UC Santa Barbara Doctoral Student Travel Grant
2017	Mananya Tantiwiwat Fellowship
2017	DowMI/MRL Winter-Spring 2017 Travel Fellowship
2016	National Science Foundation Graduate Research Fellowship Program
2015	UC Santa Barbara Regents' Fellowship in Chemistry and Biochemistry

SELECTED PRESENTATIONS

2019	*Investigation into Various Lewis Acids' doping effect on PCPDTBT*. Oral Presentation. **CPOS (Center for Polymers and Organic Solids) Meeting, 2019.** UC Santa Barbara
2018	*Towards understanding the fundamental doping mechanism of PCPDTBT-SO_3K.* Poster Presentation. **Gordon Research Conference: Hybrid Electronic and Photonic Materials and Phenomena, 2018.** Hong Kong SAR, China.
2018	*Poop to Power*. Oral Presentation. **Grad Slam, 2018.** UC Santa Barbara Graduate Division
2018	*Doping of Lewis basic polymers with Lewis acids*. Oral Presentation. **CPOS (Center for Polymers and Organic Solids) Meeting, 2018.** UC Santa Barbara
2017	*Poop to Power*, Oral Presentation. **Lunch and Learn, 2017.** UC Santa Barbara
2017	*Towards Understanding Doping of CPE-K*. Oral Presentation. **CPOS (Center for Polymers and Organic Solids) Meeting, 2017.** UC Santa Barbara
2017	*Probing* G. sulfurreducens' *electron transport on the nanoscale via conducting atomic force microscopy*. Oral Presentation. **University of California Chemical Symposium, 2017.** Lake Arrowhead, CA

2016	*Probing nanoscale charge transfer from bacteria via cAFM and CPEs*. Oral Presentation. **CPOS (Center for Polymers and Organic Solids) Meeting, 2016.** UC Santa Barbara

RESEARCH EXPERIENCE

2018	*Supramolecular Systems, Department of Physics, Humboldt-Universität zu Berlin, Berlin, Germany.* **Supervisor: Prof. Norbert Koch** Guest researcher studying the effects of different Lewis acids on a series of nitrogen and sulfur containing organic semiconducting polymers *via* photoelectron spectroscopy.
2015 – 2020	*Center for Polymers and Organic Solids, Department of Chemistry, University of California, Santa Barbara, CA.* **Supervisor: Prof. Thuc-Quyen Nguyen** Worked on multiple projects including: developed novel combinations of established techniques to analyze electron transfer efficiency and mechanism between electrogenic bacteria and the underlying substrate, and determined the fundamental doping mechanism of a variety of conjugated polymers to make them conductive for organoelectronic applications.

TEACHING EXPERIENCE

Spring 2020	**Teaching Assistant.** UC Santa Barbara. *Chem 153, Advanced Analytical Chemistry Laboratory*
Winter 2020	**Teaching Assistant.** UC Santa Barbara. *Chem 1BL, General Chemistry Laboratory*
Fall 2019	**Teaching Assistant.** UC Santa Barbara. *Chem 110L, Introductory Biochemistry Laboratory*
Summer 2019	**Primary Instructor of Record.** Santa Barbara City College. *Chem 104, Fundamentals of General, Organic, and Biological Chemistry*
Spring 2019	**Instructor of Record.** Santa Barbara City College. *Chem 155, General Chemistry*
Spring 2018	**Teaching Assistant.** UC Santa Barbara. *Chem 153, Advanced Analytical Chemistry Laboratory*
Fall 2017	**Instructor of Record.** Santa Barbara City College. *Chem 101, Introductory Chemistry Laboratory, and Chem 155, General Chemistry Laboratory*
Spring 2017	**Teaching Assistant.** UC Santa Barbara. *Chem 153, Advanced Analytical Chemistry Laboratory*

ABSTRACT

Fundamental Studies on Unique Doping Mechanisms in Organic Semiconductors

by

David Xi Cao

A world that runs on electronic devices is here to stay. The widespread use of electronic devices in our everyday life has ensured their staying power, while also driving new innovation towards improving everything from the power output of batteries, the computing power of CPUs, and the mechanical flexibility of our devices. Most of our current electronics are built in large part using silicon thanks to our robust ability to create precisely doped p- and n-type silicon wafers that allow for the creation of p-n junctions that underlie the heart of modern electronics. One drawback however to silicon-based devices is their relative mechanical inflexibility. Given recent trends towards wearable electronics and flexible sensors that can be used for biological applications, development of conductive, flexible organic semiconductors can fill a market and technological need. In addition, organic semiconductors have the potential to be lower in cost and take less energy to fabricate than their silicon counterparts.

Since the 1990s discovery of polymers that could be made conductive through doping, there has been a lot of work in the field to make organic electronics a reality. The field has spent a lot of its time and energy focused on using and understanding the dopant F_4TCNQ to

create doped organic semiconductors over the past decade, which operates on the principle of integer charge transfer in most circumstances. However, limits to F_4TCNQ doping have driven research into novel dopants and understanding their doping mechanism to open new avenues for creating doped polymers.

This work tackles some of these new dopants and their doping mechanism, specifically Bronsted and Lewis acids. While they have both been used previously for doping polymers, little attention has been paid to them over the past decade while the field has chased dopants with increasingly deeper electron affinities for use in integer charge transfer doping. We bring these dopants back to light and provide an in-depth look into the doping mechanism for Bronsted acid doping. By using a wide slate of techniques including XPS, FTIR, UV-vis-nIR, AFM, TGA-MS, XRR and electrical measurements, we provide an estimation of the doping efficiency along with a complete picture of the Bronsted-acid doping mechanism for the conjugated polyelectrolyte PCPDTBT-SO_3K, and the importance of sulfonate for these self-doping conjugated polyelectrolytes. We also touch on Lewis acid doping, and how Lewis acid strength does not correlate to increased doping efficiency or stability of these dopants by using impedance spectroscopy, EPR, UV-vis-nIR, XPS and electrical measurements. Lastly, we make use of p-doped OSCs and cAFM to show how de-doping on the microscale can be used as a novel way to image the efficacy of bacterial electron transfer to the substrate which can lead to a better understanding of how to improve the efficiency of bacteria driven fuel cells.

TABLE OF CONTENTS

Chapter 1 − Introduction to Doping.....1

A. History of doping.....1

B. Doping mechanisms – ICT, CT, Bronsted-acid.....11

C. Techniques employed to study doping.....16

D. Focus of this thesis.....23

Chapter 2 − Understanding the Doping Mechanism of CPE-K.....25

A. Introduction to Conjugated Polyelectrolytes.....25

B. Proposed structure of doped and de-doped CPE-K.....27

C. X-ray photoelectron spectroscopy (XPS).....28

D. Attenuated Total Reflectance-FTIR Spectroscopy (ATR-FTIR).....34

E. UV-vis-nIR Absorption Spectroscopy.....36

F. Electrical Measurements.....38

G. Estimation of CPE-K doping efficiency.....39

H. Reversible de-doping of CPE-K by annealing.....42

I. Experimental Section.....48

Chapter 3 − Lewis Acid Doping.....52

A. Introduction to work on Lewis acids.....52

B. Choosing of polymer and dopants to study.....56

C. Impedance Spectroscopy (IS).....64

D. Doping Efficiency Trends and Discussion.....70

E. Experimental Section.....74

Chapter 4 − Using CPE-K to Visualize Electron Transfer from Bacteria 77

A. Introduction to Microbial Fuel Cells (MFCs) 77

B. Experimental Requirements 78

C. Sample Preparation and Imaging 81

D. Inefficiencies in Bacterial Electron Transfer 83

E. Quantitative Electron Transfer Calculations 86

F. Experimental Section 89

Chapter 5 − Conclusions 93

A. Understanding the doping mechanism of CPE-K 93

B. Lewis acid doping 94

C. Using CPE-K to visualize electron transfer from bacteria 95

Chapter 6 − References 96

Chapter 7 − Appendix 107

LIST OF FIGURES

Figure 1-1. Polyacetylene 2

Figure 1-2. Example small molecule organic crystalline semiconductors 3

Figure 1-3. Cartoon drawing of band transport versus hopping transport 4

Figure 1-4. Examples of early p-type organic semiconductor oligomers 6

Figure 1-5. Examples of p-type organic semiconductor polymers 7

Figure 1-6. Common small molecule p-type dopants 8

Figure 1-7. Integer charge transfer doping model 13

Figure 1-8. Charge transfer state doping model 14

Figure 2-1. Schematic of conjugated polyelectrolytes 25

Figure 2-2. Chemical Structures of Doped and De-doped CPE-K 27

Figure 2-3. High resolution XPS spectra 29

Figure 2-4. Normalized high-res C 1s XPS spectra of CPE-K under different doping conditions 31

Figure 2-5. Survey XPS spectrum of self-doped CPE-K 34

Figure 2-6. ATR-IR spectrum and corresponding functional group vibrations denoted by color on the chemical structure on the right 35

Figure 2-7. Normalized UV-vis-nIR of CPE-K films at various levels of doping 36

Figure 2-8. Gaussian peak fits to UV-vis-nIR spectra of CPE-K 37

Figure 2-9. Arrhenius plot of CPE-K films at different doping levels 39

Figure 2-10. TGA-MS of self-doped CPE-K showing loss of H_2O upon heating 43

Figure 2-11. UV-vis-nIR absorption spectra of CPE-K after annealing and re-doping in H_2O 43
Figure 2-12. Histogram of cAFM current distribution with annealing 45
Figure 2-13. Film morphology and current distributions of CPE-K films pre- and post-annealing.....45
Figure 2-14. I-V curves of CPE-K obtained under vacuum at different temperatures 46
Figure 2-15. Arrhenius plot of annealed CPE-K films 47
Figure 2-16. TGA-MS of self-doped CPE-K showing formation of SO_2 and SO 48
Figure 3-1. Lewis acid-base reaction schematic.....52
Figure 3-2. Doping mechanism of BCF and PCPDTBT 54
Figure 3-3. π−backbonding to empty p-orbital on boron atom 55
Figure 3-4. Polymer and Lewis acid structures, UV-vis-nIR absorption spectra, and kinetics data.....57
Figure 3-5. High-resolution N 1s XPS spectra of polymers with and w/ out BCF 58
Figure 3-6. Survey and high-resolution C 1s and S 2p XPS spectra of polymers with and w/ out BCF.....59
Figure 3-7. Survey and high-resolution S 2p XPS spectra of CPDT monomer with and w/out BCF.....60
Figure 3-8. EPR spectra (top) and energy levels (bottom) of polymers with BCF. 61
Figure 3-9. EPR spectra of polymers with BCF and F_4TCNQ.....62
Figure 3-10. UPS spectra of polymers with BCF 63
Figure 3-11. MIS device schematic operating in accumulation and depletion regimes.66

Figure 3-12. Representative capacitance-frequency plot from MIS measurements of PCPDT-BT and BCF 67
Figure 3-13. Representative capacitance-voltage plot from MIS measurements of PCPDT-BT and BCF 68
Figure 3-14. Representative Mott-Schottky plot from MIS measurements of PCPDT-BT and BCF 69
Figure 3-15. Chemical structures of BCF and PCPDT-BT and Lewis acid strengths 70
Figure 3-16. Doping efficiency and number of holes of PCPDT--BT for different Lewis acids 71
Figure 3-17. PCPDT-BT doping efficiency of different boron-based Lewis acids over time 73
Figure 4-1. Diagram of microbial fuel cells (MFCs) 77
Figure 4-2. Schematic for de-doping of CPE-K by bacteria 79
Figure 4-3. UV-vis-nIR film absorption spectra of CPE-K before and after thermally reversible de-doping 80
Figure 4-4. Figure of cAFM setup used in this experiment 81
Figure 4-5. AFM (left) and cAFM (right) images of *G. sulfurreducens* on CPE-K 82
Figure 4-6. AFM (left) and cAFM (right) images of imperfect *G. sulfurreducens* on CPE-K 84
Figure 4-7. AFM (left) and cAFM (right) images of *E. coli* on CPE-K 85
Figure 4-8. High resolution AFM image of *G. sulfurreducens* on CPE-K 85
Figure 4-9. cAFM and morphology images of *G. sulfurreducens* on CPE-K 88
Figure 7-1. Schematic for preparation of *G. sulfurreducens* CPE-K sample 107

LIST OF TABLES

Table 2-1. Atomic Ratios of Elements from High-Res C 1s XPS spectrum 29

Table 2-2. Summary of XPS integrations from survey spectra of CPE-K 30

Table 2-3. Atomic percentages of C and K in Figure 12.....31

Table 2-4. Peak area percentages from Gaussian fits in Figure 16 37

Table 2-5. Electrical Measurements of CPE-K Doped at Various Levels 38

Table 2-6. Charge transport activation energy at various annealing temperatures.....47

Table 4-1. Mobility data from nano and bulk SCLC measurements 87

Chapter 1 − Introduction to Doping

To the normal lay person, the word doping invokes memories of Barry Bonds or Lance Armstrong who used substances not authorized by their respective athletic governing committees in order to enhance their performance. This image of doping can actually be applied in the context of scientific research as well, where here we define doping as the addition of a small amount of a chemical compound in order to enhance (or suppress) the electrical properties, namely conductivity, of an organic semiconductor. Lance Armstrong would be the organic semiconductor, the improvement in electrical conductivity of the semiconductor is like an improvement in Armstrong's speed on his bike, and the dopant is, well, the dopant.

A. History of doping

At the time of this writing, the doping of inorganic semiconductors such as silicon has been known for many decades and forms the foundational basis for our electronic devices today.[1,2] By adding a specific number of dopant atoms with either less or more valence electrons than silicon such as boron and nitrogen respectively, electrons can be either taken out of or added into silicon, providing the free charge carriers necessary for electrical transport to occur. In doing so, the formation of p- and n-doped silicon can be readily achieved, allowing for the creation of p-n junctions that are ubiquitous in consumer electronics. However, the creation of crystalline silicon that is needed for high charge-carrier mobilities, with mobility being defined as the speed at which a free charge carrier such as a hole or electron can travel throughout the material, is immensely energy intensive. Due to the large amount of energy needed for the creation of silicon-based devices such as silicon photovoltaics (PVs), the

amount of energy we can readily obtain from silicon PVs before the end of their life cycle is reduced.[3,4]

The energy-intensive nature of silicon processing and issues with mechanical flexibility of silicon-based devices opened the door for organic semiconductors. Organic semiconductors (OSCs), which can be simplistically defined as conductive plastics, are mechanically flexible opening the door for niche applications where such flexibility is necessary.[5–7] In addition, OSCs are less energy intensive to process because many of them are soluble in common organic and inorganic solvents, allowing for solution-based processing such as spin-coating, roll-to-roll printing, and inkjet printing, which take significantly less energy than the growth process and doping of crystalline silicon which involves high pressures and temperatures.[8–11] The doping of organic semiconductors was first discovered by Heeger, MacDiarmid, and Shirakawa in 1977.[12–18] Their initial studies that broke open the field of organic semiconductors was on the doping of polyacetylene by halogen vapor, specifically Cl_2, Br_2, and I_2 (Figure 1-1).

The conductivity of polyacetylene increased 7 orders of magnitude from 10^{-5} S/cm to 10^{2} S/cm and was accompanied by a corresponding decrease in activation energy for charge

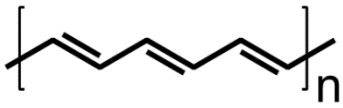

Figure 1-1. Polyacetylene

transport from 300−500 meV to 18 meV. In the case of I_2, their studies revealed that the process of doping was similar, in that the generation of I_3^- in situ provided the electron donor moiety that gives electrons to polyacetylene. This combination of polyacetylene and iodine was able to generate data showing that polyacetylene is now acting, electrically, as if it is a metal. Their work earned them the Nobel Prize in Chemistry in 2000.[15]

The chemical structure of polyacetylene, though excellent for electrical conductivity, makes it difficult to process, which is a drawback for organic semiconductors since the appeal of organic electronics is their potential physical flexibility and ease of processing. Despite this, early research still focused on achieving charge transport properties of metals—that is, band transport which is achieved by highly crystalline materials—by studying organic small molecules such as naphthalene, perylene, and pentacene (Figure 1-2) which are conjugated planar systems that can form nicely ordered crystalline lattices under ideal conditions. Some of these organic crystalline small molecules have been shown to achieve very high charge carrier mobilities (400 $cm^2/V{\cdot}s$) at low temperatures and after extensive purification—an impressive mobility value that rivals that of polycrystalline silicon.[19,20]

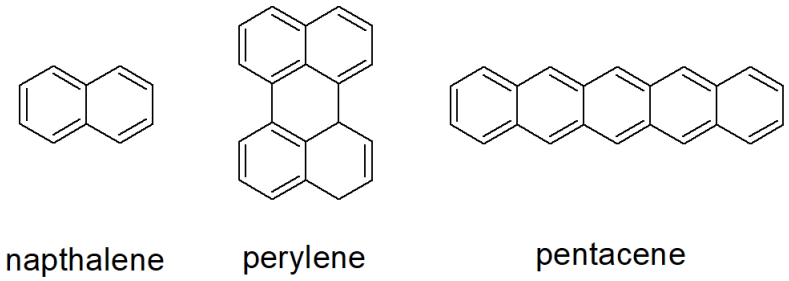

Figure 1-2. Example small molecule organic crystalline semiconductors

In addition, temperature dependent measurements revealed these small molecules were most likely operating in the band transport regime, which is normally associated only with metals. In band transport, due to the delocalized wavefunction over the entire volume, charge carriers travel freely throughout the material without needing to overcome energetic barriers within the system. In hopping transport, the wavefunctions are localized, requiring charge carriers to hop from one site to another which requires energy. Experimentally, band transport and hopping transport can be distinguished *via* changes to the mobility with temperature—with increasing temperature, band transport mobilities decrease due to the presence of defects

caused by thermal vibrations in the crystalline lattice. In hopping transport on the other hand, with increasing temperature mobilities typically increase as additional energy is available to the free charge carriers to hop from one site to another in the material as discussed later in this thesis (Figure 1-3). Band transport is typically associated with metals, while hopping transport is typically associated with semiconductors.

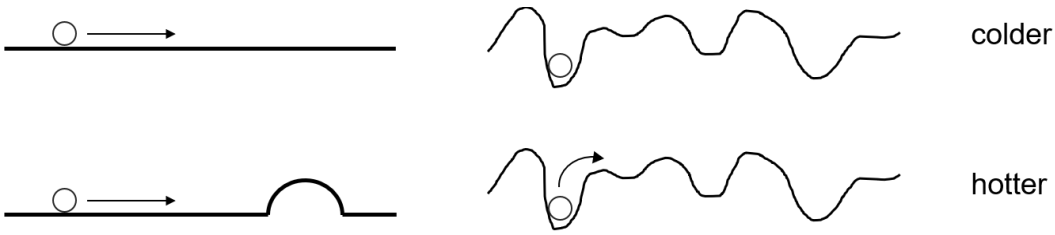

Figure 1-3. Cartoon drawing of band transport (metals) versus hopping transport (semiconductors)

Despite these organic crystalline small molecules' impressive electronic transport properties, processing of these small molecules to achieve such mobilities is not trivial, and its crystalline nature precludes the possibility of its use for flexible organic electronics. As such, device manufacturers stayed with silicon, and scientists pursued other organic semiconductors that could also be doped to achieve high mobilities and conductivity.

From these early studies came additional research that focused in one of two directions. The first was to look for organic semiconductors that are more easily processable than polyacetylene, naphthalene, and perylene, but that could still be doped to achieve good electrical transport properties. A second prong of research that emerged was an investigation into other dopants that could be used aside from halogen vapor, since halogens were shown to be unstable as the vapor could diffuse through and out of the film, reversing the doping process. Halogen vapor doping is also hard to control, in that a wide range of different conductivity values would be obtained upon doping with halogen vapor outside of the researcher's control.

1. Structural properties of early organic semiconductors

A sampling of the new organic semiconductors that were synthesized and whose electrical parameters were measured are in Figure 1-4. A couple of structural similarities and patterns are distinguishable when looking at the set of structures below—first, there was continued work in synthesizing and measuring electrical characteristics of fused ring organic semiconductors as researchers continued to pursue the possibility of having a well-packed ordered crystalline lattice of organic semiconductors that would be able to transport charges at very high mobilities.[21–26] However, issues with solubility of structures such as anthracene, pentacene continued to exist, thus leading to new structures such as anthradithiophene (ADT), where the attached thiophene groups would help provide some solubility and serve as attachment points for solubilizing alkyl chains.[27] The second structural motif that emerged was the use of thiophene based oligomers such as sexithiophene (6T).[28] These rigid rod-like oligomers are particularly electron-rich due to the sulfur component in each heterocycle, and also contain many more entry points for chemical modifications that would enhance solubility as seen in dihexyl-sexithiophene (DH-6T) and methyl ethylene-sexithiophene (Et-6T).[29,30] Mixtures of fused ring systems with thiophenes were also introduced such as bis-TDT and DH-FITTFI.[31,32] While electron-rich thiophene based oligomers were seen as promising candidates, researchers also found that they are prone to oxidation in air due to high HOMO energy levels of such systems.

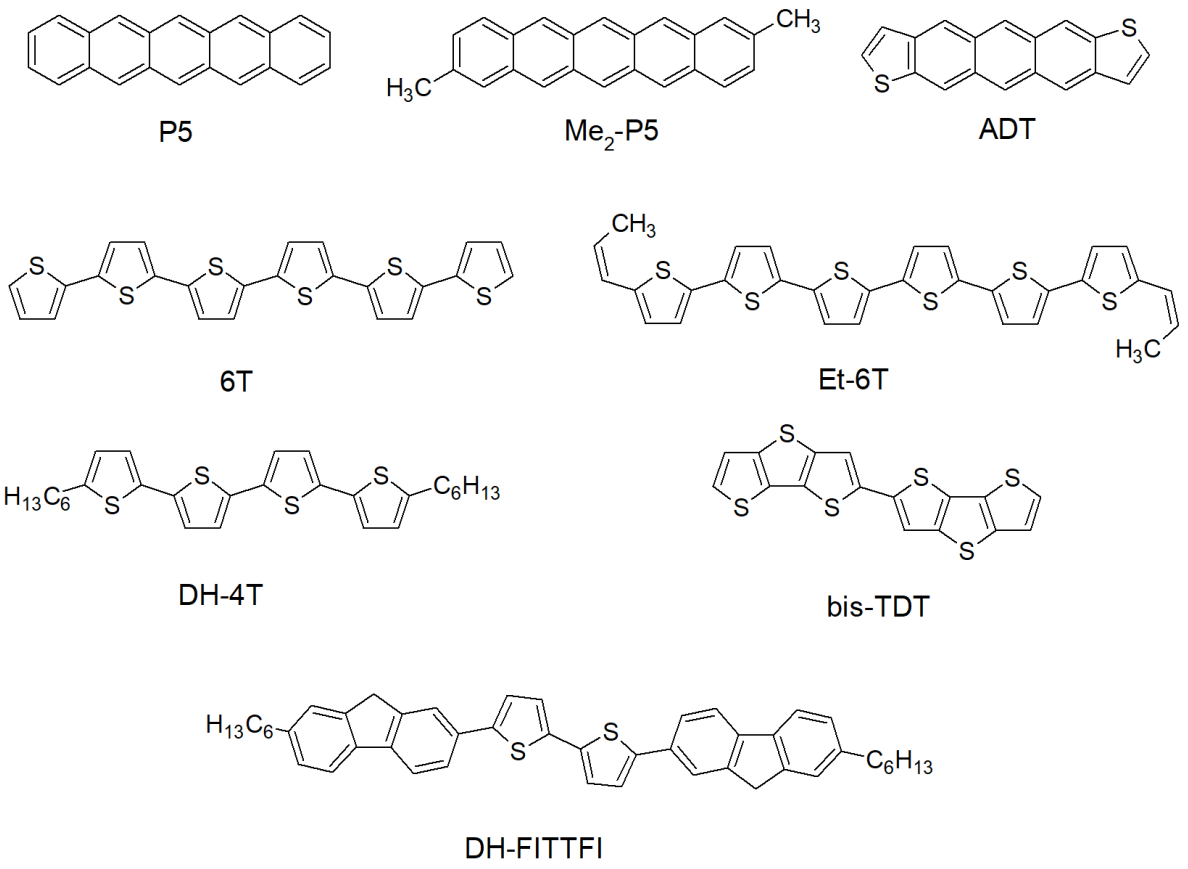

Figure 1-4. Examples of early p-type organic semiconductor oligomers

Polymeric structures were developed based off the aromatic based oligomer systems studied and solubilized by adding alkyl chains to various attachment points on the monomers, examples of which are shown in Figure 1-5. These efforts led to the synthesis of one of the most well-known organic semiconductors poly-3-hexylthiophene (P3HT).[33–36] P3HT's energy levels allow for doping and also make P3HT relatively more stable than its other organic semiconductor counterparts. In addition, P3HT's solubility in common organic solvents opened the door for creating flexible electronics, allowing the polymer to be spun cast or even printed onto various flexible substrates. Ease of processability and solubility of such polymers also helped to drive new research in the field, which continued expanding to include donor-acceptor based systems that help narrow the band gap of the polymer which are

beyond the scope of this thesis. Efforts to reduce the HOMO level to make the polymers more stable in air were also undertaken by substituting the bridging carbon atom with silicon as in TS6T2 and BS6T2.[37] There are two important takeaways from this discussion on chemical structures. The first is organic systems are highly modifiable to fit exacting needs thanks to the efforts and expertise of synthetic chemists. The second is electron-rich thiophene based polymer structures allow for protonation of the polymer backbone, which is exploited and discussed in this thesis.

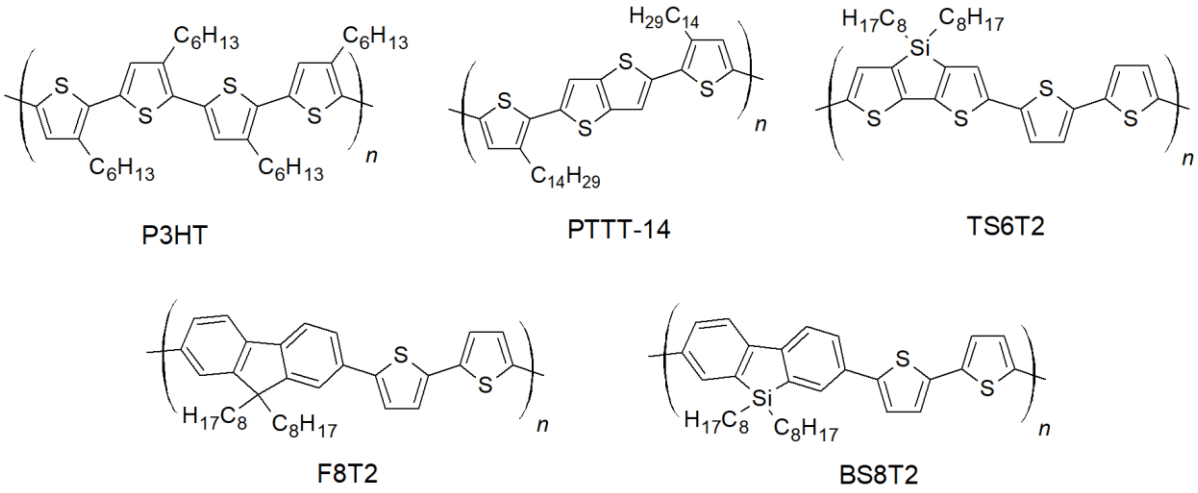

Figure 1-5. Examples of some p-type organic semiconductor polymers

2. Introduction and summary of p-type dopants

A large variety of dopants have been synthesized and tested since the first reports of halogen vapor doping. The dopants fall into different classes including elemental species, covalent solids, Bronsted acids, Lewis acids, and small molecule dopants. The elemental species that have been employed in doping include Cl_2, Br_2, I_2, and O_2. Covalent solids that have been employed in doping involve metal oxides with deep electron affinities such as MoO_3, V_2O_5, and WO_3.[38–44] Almost all strong Bronsted acids such as HCl have also been used

for doping.[45–47] The most common Lewis acids that have been used in doping are $FeCl_3$ and $SbCl_5$, though recently boron-based Lewis acids have been used for doping as well as described in this thesis and elsewhere. Small molecule dopants with deep electron affinities have been developed for doping as well, with the most common ones derived from tetracyanoquinodimethane (TCNQ) as shown in Figure 1-6. Each of the dopant classes will be expounded on below along with their uses and drawbacks.

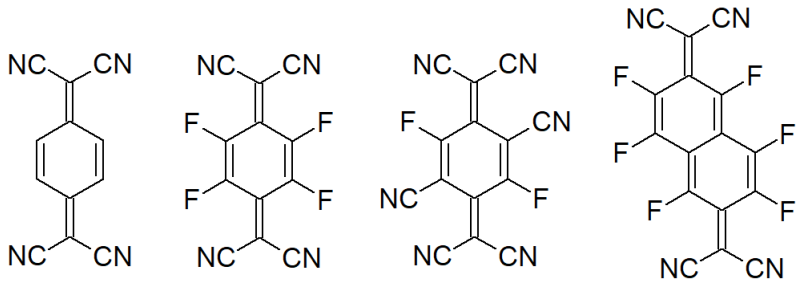

Figure 1-6. Common cyanobased small molecule p-type dopants

Recall that issues with halogen vapor doping included instability due to the ability of the halogen atoms to diffuse through the organic semiconductor matrix. In addition, while oxygen can dope some electron-rich organic semiconductors, the prevalence of oxygen in our environment makes controllable doping difficult to achieve.[48–52] These issues led to the pursuit of other dopants as described above.

Metal oxides tend to require very high temperatures in order to thermally evaporate them for deposition onto the organic semiconductor except for MoO_3. Sol-gel processing methods are possible for these metal oxides, which would then allow for deposition onto the substrate *via* spin-coating. In addition, metal oxides are sensitive to processing conditions, which can influence the frontier energy levels more than 1 eV.[53] Thermal evaporation and sol-gel processing of metal oxides do not allow the metal oxide to penetrate into the bulk of the organic semiconductor matrix, thus preventing doping of the entire bulk. In addition, metal

oxides tend to form clusters with themselves as opposed to evenly dispersing across the organic semiconductor leading to inconsistent doping profiles.[54]

Strong inorganic Bronsted acids tend to be soluble in water and other polar protic solvents, which can be useful if the organic semiconductor is also soluble in the same solvents. Miscibility would allow doping of organic semiconductors in solution, which can be easily controlled. This interaction was taken advantage of as described in Chapter 2 of this thesis to controllably dope an organic semiconductor with pendant ionic groups. On the other hand, many organic semiconductors tend to be soluble in non-polar organic solvents, in which many strong inorganic Bronsted acids are insoluble and significantly less acidic as well.

Lewis acids have many uses aside from the doping of organic semiconductors such as their role as catalysts for organic synthesis applications. Early Lewis acids that were used for doping included $FeCl_3$, $SnCl_4$, and $SbCl_5$.[55–59] As a catalyst, the Lewis acids activate sites for nucleophilic attack by withdrawing electron density, thus aiding in addition reactions to carbonyls, Diels-Alder reactions, carbonyl-ene reactions, and Friedel-Crafts alkylation and acylation.[60–66] As a dopant, Lewis acids work on the same principle and p-dope the organic semiconductor. An additional benefit to Lewis acid doping is their relatively high solubility in a wider array of solvents than Bronsted acids, thus allowing them to dope a wider variety of polymers in solution. Later research made use of tris(pentafluorophenyl)borane (BCF), which has even better solubility in non-polar organic solvents than transition-metal based Lewis acids.[67–72] Some boron-halogen based Lewis acids such as BF_3, BCl_3, and BBr_3 have stability issues however, being very reactive to air thus limiting its use outside of the glovebox.

Small molecule dopants were a large breakthrough in the field of organic semiconductor doping. The development of tetrafluoro-tetracyanoquinodimethane (F_4TCNQ) as a dopant

allowed for controllable doping of organic semiconductors since F_4TCNQ is a solid and can be weighed out according to the precise molar amounts needed.[73–75] In addition, though F_4TCNQ is not very soluble, enough of it can dissolve in solvents commonly used to process organic semiconductors to allow for solution-based processing and doping which is less energy intensive and procedurally much more simple than other processes such as thermal evaporation.[76,77] While F_4TCNQ's structure allows for intercalation within the organic semiconductor, it also makes F_4TCNQ prone to aggregation which can disrupt the packing structure of the organic semiconductor which hinders charge mobility.[78–81] Though cosolvents and sequential processing can be employed, F_4TCNQ's limited solubility also places an arbitrary upper limit on the amount of dopant that can be added to the organic semiconductor, potentially limiting the number of free charge carriers that can be generated and by extension the conductivity that can be achieved.

One last note: All the material covered in Chapter 1-A. History of doping, pertains to p-type doping. P-type doping entails the creation of holes in semiconductors, whereas its counterpart, n-type doping, entails the creation of electrons in the semiconductor as mentioned in the beginning of Chapter 1-A. While p- and n-type doping can be readily achieved in silicon, n-type doping is more difficult to achieve in organic semiconductors. The reason for this is the LUMO of organic semiconductors is often too shallow for facile n-type doping to occur. Few electron donors are strong enough to donate an electron to organic semiconductors, and the donors themselves are prone to reacting in unstable fashion with air, which precludes its use in industrial applications. Attempts to synthesize organic semiconductors with a LUMO deep enough to allow for n-type doping are ongoing but are hindered by the difficulty in incorporating strong electron withdrawing groups within the chemical structure. Some

proposed structures as determined by computational theory can be found on the webpage of the Materials Project. N-type doping of organic semiconductors is an open research field with a lot of promise, should appropriate chemical structures for n-type doping be produced. For the aforementioned reason this thesis focuses on p-type doping, and on fundamentally understanding a lightly used but important doping mechanism for organic semiconductors.

B. Doping mechanisms – ICT, CT, Bronsted-acid

In the organic electronics community, recent discussions have revolved primarily around integer charge transfer (ICT) and charge transfer states (CT) as the two models for how doping occurs in organic semiconductors. Both models run under the premise of some amount of electron transfer from one species to the other, where ICT involves full electron transfer, and CT involves partial electron transfer. A detailed study into the doping mechanism of F_4TCNQ revealed a similarity with halogen vapor doping where both processes involve integer charge transfer when the energy levels are favorable for integer charge transfer to occur. In the case of F_4TCNQ, the dopant molecule accepts an electron from the polymer, thus creating a mobile hole in the backbone whereas in halogen vapor doping, electrons were being donated from the dopant molecule to the polymer. When energy levels of the host and F_4TCNQ are closer in energy, F_4TCNQ has been hypothesized to form charge transfer states with the orbitals of the host instead. While integer charge transfer and charge transfer states have dominated the field of organic electronics, there is a third doping mechanism that involves proton transfer from a Bronsted-acid. Discovered in the late 1980s, this method of doping polymers has received much less attention than its integer charge transfer counterpart until recently, due to an increasing push towards using green solvents for processing organic electronics. Many dopants as described above currently used by the OSC community are insoluble in green

solvents such as EtOH and H_2O, which opens the door to increased study and use of Bronsted-acids for doping. In addition, the community's previous work on Bronsted-acid dopants has shown increased control over the amount of doping, thereby preventing over-doping of the OSC which was seen when doping with halogen vapor, a process that caused the OSC to lose its beneficial mechanical properties. While Bronsted-acid doping can be seen as a form of ICT since when proton transfer occurs the Bronsted base loses electrons while the Bronsted acid gains electrons, involving a proton as well brings this beyond the realm of just ICT. An extended summary of the three types of doping mechanisms are presented below.

1. Integer charge transfer (ICT)

Integer charge transfer operates under the premise that electrons prefer to occupy the lowest energy state possible. Therefore when the HOMO (or ionization potential in the case of polymers) of the organic semiconductor (OSC) species is more shallow in energy than the LUMO (or electron affinity) of the dopant species (in the case of p-doping), an electron is transferred from the OSC to the dopant, leaving behind a hole in the HOMO (Figure 1-7). The hole is then free to move throughout the OSC matrix, contributing to the concentration of charge carriers that constitutes doping.

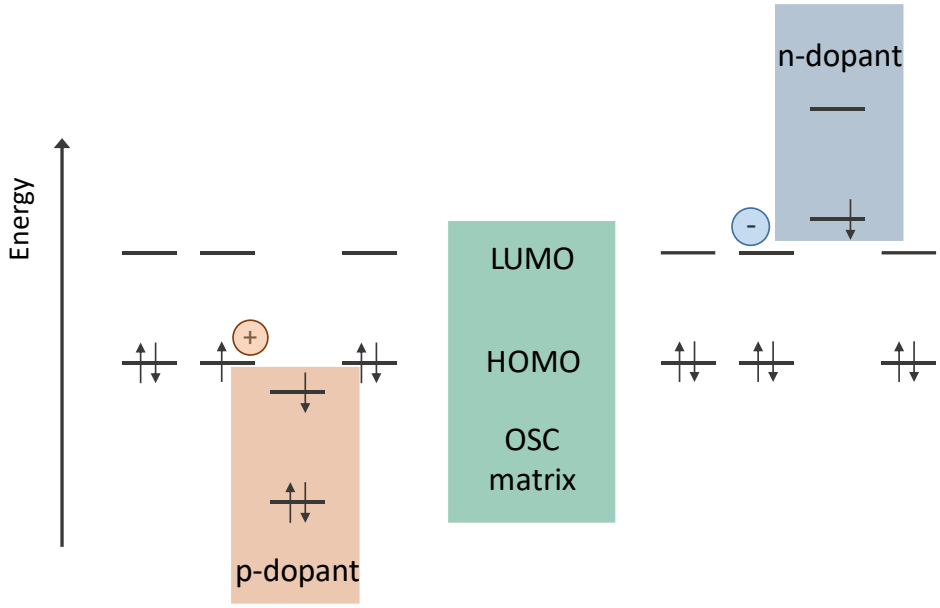

Figure 1-7. Integer charge transfer doping model

The most famous dopant, F_4TCNQ, operates under the ICT model for most organic semiconductors because of its deep electron affinity. Conversely, n-doping can also occur when a dopant has a HOMO (ionization potential) that is greater than the LUMO (electron affinity) of the OSC. The electron from the dopant will then move to the LUMO of the OSC, increasing the concentration of charge carriers in the OSC matrix.

This simplified model does leave out an important aspect of doping, which is the coulombic affinity between the hole (or electron) in the OSC and the electron (or hole) in the dopant. The electrostatic attraction between the two species often hinders charge carrier movement, thereby preventing the charge carrier from contributing to the conductivity of the OSC. The activation energy needed to overcome the electrostatic attraction can be larger than the available thermal energy in the system, thereby preventing the formation of free charges. To increase the number of free charge carriers in the system, there have been suggestions that

by increasing the amount of disorder in the system, more sites are available for the charge carrier to hop to, thereby making it easier to overcome the coulombic attraction.

One additional comment is that for free charge carriers to move through the OSC matrix, the charge carrier needs to hop from site to site as previously mentioned. This hopping process requires a certain amount of energy depending on the energy level of neighboring sites to which the charge carrier can travel to, which is often referred to as the charge transport activation energy. The energy required to break the coulombic attraction between the charged species in the OSC and dopant is also included in this measure of activation energy, which is averaged across the entire system of interest.

2. Charge transfer state (CT)

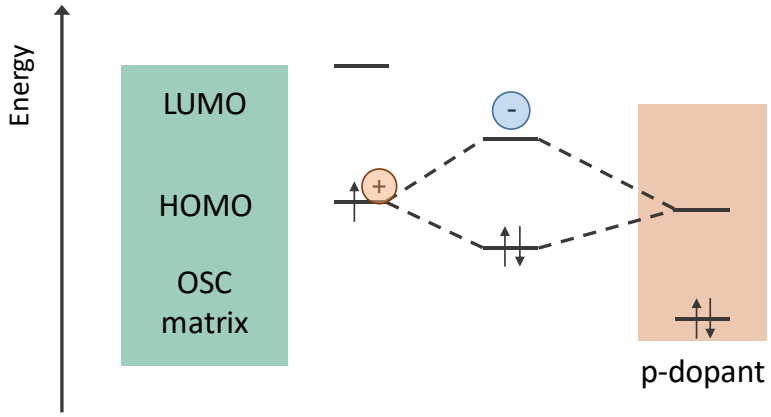

Figure 1-8. Charge transfer state doping model

Another doping model discussed in the literature revolves around charge transfer states that take on a hybrid sort of nature where the HOMO orbital of the OSC and the LUMO orbital of the dopant interact and mix to form new MOs. This is most likely to occur between an OSC and dopant where the HOMO and LUMO, respectively, are close in energy. After mixing, the new MOs will have one occupied and one unoccupied state. Electrons in the HOMO of the

OSC from a neighboring site on the OSC can then interact with the new MOs, as seen in Figure 1-8. Promoting one of the electrons *via* thermal excitation from the HOMO of the OSC to the antibonding state of the MO creates a hole in the OSC, which is presumably then free to move throughout the OSC matrix, after taking into account the discussion regarding coulombic attraction as discussed in the ICT section. In the case of CT states, the activation energy for charge transport depends on the difference in energy between the antibonding state in the MO and the HOMO of the OSC matrix, as well as the charge transfer integral between the HOMO of the OSC and the LUMO of the dopant molecule.

3. Bronsted-acid

The third doping mechanism to be touched on in this introduction is Bronsted-acid doping. Though Bronsted-acid doping was first reported in the 1980s, the relative lack of publications and studies on Bronsted-acid doping is somewhat surprising. One article suggested the lack of publications on this topic is due to underappreciation of the relationship between acid strength and ionization potential of the polymer under study, leading researchers to try arbitrary combinations of polymers and acids.[82] Another possibility is the work that was conducted on studying doping by Bronsted acid ended up being almost solely on polymers containing a pendant sulfonate moiety due to its self-doping ability—that is, during processing the solvent itself would dope the polymer, precluding the need for external dopants.[83–89]

Initial hypotheses revolving around Bronsted-acid doping involved protonation of the polymer backbone or a redox reaction that accompanied the generation of H_2 gas. The first indication that neither hypotheses were completely correct came in 1989, where it was shown that upon doping of the polymer PDMPV, an EPR signal could be seen, indicating the presence of an unpaired electron which would not be present in the case of only protonation.

In addition, no H_2 gas formation was observed during the doping process, suggesting the doping mechanism is not by way of a redox reaction that generates H_2 gas. Since then, there has been limited work on studying the underlying Bronsted-acid doping mechanism, though it has been employed and shown to work for a slate of different polymers.[83–85,90]

C. Techniques employed to study doping

In the course of this work, many different techniques were employed to help elucidate different aspects of the doping mechanism to help provide a complete picture. A brief overview of each of the techniques employed will be provided below to help provide a picture for the information they provide and their use towards this project. Some of them may be familiar to chemists, while others are not, which is the beauty of doing work in a highly interdisciplinary field.

1. Ultraviolet-visible-near-infrared absorption spectroscopy (UV-vis-nIR)

This common general chemistry technique proves to be very useful when studying doping. A range of monochromated light is sent through the sample and a reference, and the amount of photons that are transmitted through the sample at each wavelength is recorded by the instrument. The organic semiconductor materials studied in this thesis happen to have color visible to the naked eye, which manifested itself in the UV-vis-nIR absorption spectrum. When organic semiconductors are doped and a polaron is formed, the polaron absorbs light at a larger wavelength than the native organic semiconductor due to the formation of intragap states that are created upon doping. In the organic semiconductor community, a polaron is defined as a positive charge, or hole, and an unpaired electron in close proximity to each other.

UV-vis-nIR allows for a very quick, robust method of checking if a material has been doped or not.

The above paragraph describes UV-vis-nIR operating in spectrum mode. UV-vis-nIR absorption spectroscopy can also be operated in kinetic mode, where the absorption at a particular wavelength is monitored over time. Running UV-vis-nIR in kinetics mode helped hint to us that the formation of Lewis acid-base adducts and doping were not the same process. Additional details are in Chapter 3.

2. Fourier transform infrared spectroscopy (FTIR)

FTIR is also a common technique employed most often by organic chemists and learned by most sophomore chemistry students. The operational principle is similar to UV-vis-nIR absorption spectroscopy, in that infrared light is passed through the sample by way of beam splitters, a monochromator, and a mirror, and the amount of photons that make it through the sample are measured by the instrument. Photons not incident on the detector are absorbed by the sample, giving the FTIR spectrum. Since Bronsted acid doping involves the transfer of protons, the location of protonation can be elucidated *via* FTIR spectroscopy by looking for changes in the FTIR spectrum and correlating them with changes to the chemical structure.

3. X-ray photoelectron spectroscopy (XPS)

XPS is a relatively niche technique compared to UV-vis-nIR and FTIR and is used primarily for surface chemical analysis. While not commonly used, its operational principle is based on the photoelectric effect, which is often taught in lower division chemistry courses. X-ray photons are generated by the instrument *via* high voltage aluminum sources and sent through a monochromator. The sample is placed into the analytical chamber which is under

ultra-high vacuum (UHV, 10^{-10} Torr), and the X-ray photons are directed to impinge on the sample. Unlike UV-vis-nIR and FTIR, only photons of a singular energy are emitted from the instrument and sent to the sample—there is no scanning of the energy range. The high energy of the monochromated X-ray photons excite core level electrons in the elements present in the sample, ejecting them from the sample. Because core level electrons are attracted to the nucleus, and each element has a different number of protons in the nucleus in addition to a different amount of electron shielding, the core electrons that are emitted from the sample each have a specific amount of excess energy from the X-ray photon that is turned into kinetic energy. The characteristic kinetic energies are indicative of each particular element and are often converted into binding energy for display *via* the equation BE = hν − KE. The kinetic energy of the emitted electrons is detected by the XPS instrument, which scans across the energy range specified by the user, providing an XPS spectrum with the number of electrons detected on the y-axis, and the binding energy of the ejected electron on the x-axis. Detection of the kinetic energy of the ejected core electrons is the reason why samples must be analyzed under UHV. Gas particles present in the chamber could interfere with the ejected electrons' trajectory and energy, resulting in erroneous data. UHV conditions also mean low MW samples cannot be analyzed as the sample would sublime away into the vacuum.

XPS is useful for the doping studies conducted in this thesis for several reasons. Bronsted acid doping of polymers should result in p-doping, which can be checked by seeing a reduction in the amount of any positively charged counter ions as described in Chapter 2. XPS also proved useful in the Lewis acid doping study, to show that initial hints from UV-vis-nIR that Lewis acid binding to the polymer and doping of the polymer proceed by different mechanistic pathways is indeed true. Lewis acid binding to the polymer can be detected by seeing a shift

in the binding energy of the Lewis basic elements, since any bound Lewis acid would withdraw electron density from the Lewis basic element, making the electron harder to eject from the Lewis base and thus show up at a higher binding energy.

4. Ultraviolet photoelectron spectroscopy (UPS)

Ultraviolet photoelectron spectroscopy is based on the same operational principle as XPS and is often housed together with the XPS. Ultraviolet photons, generated *via* electrical excitation of helium gas, are sent through a monochromator, and then directed to the sample. Ultraviolet photons are lower in energy than X-ray photons, and so only outer valence shell electrons are excited and ejected from the sample.

In the context of doping, by ejecting outer shell electrons the HOMO level as well as the fermi level can be measured. While a detailed explanation of the fermi level is beyond the scope of this work, essentially the fermi level describes the probability of charge carrier occupation of either holes in the HOMO, or electrons in the LUMO. When the fermi level is in the middle of the band gap, it indicates an equal probability of charge carrier occupancy in the HOMO or the LUMO. When the fermi level is close to the HOMO, it indicates p-doping, whereas if the fermi level is close to the LUMO, it indicates n-doping. Measurement of the HOMO has helped with determining the likelihood that the organic semiconductor could undergo integer charge transfer in the presence of a particular dopant, though it is by no means a definitive way of determining a particular doping mechanism.

5. Electron paramagnetic resonance spectroscopy (EPR)

EPR is another useful method for determining whether or not a material has been doped and gives hints about the doping mechanism. EPR operates under a principle that is analogous

to NMR, but instead of probing nuclei spins, EPR probes electron spins. By sending microwave radiation to a sample that is under the influence of a magnetic field, unpaired electrons will absorb the radiation and if it matches a higher energy state that is antiparallel to the magnetic field, the electron will jump to it thus absorbing the microwave radiation and providing the EPR signal seen on the computer. Under ordinary circumstances, most materials would show no EPR signal because there are no unpaired electrons. However, if doping occurs in such a way as to create a free racial, then that can be measured using EPR.

This is one of the ways previous researchers elucidated that Bronsted acid doping of certain organic semiconductors does not stop at protonation of the OSC. If protonation of the OSC was all that it takes to dope, then there would be no EPR signal present as there is no free radical species.

6. Conductive atomic force microscopy (cAFM)

cAFM and AFM generally is also a relatively niche technique not often taught or employed by chemists. The operational principle of AFM relies on a tip that raster scans across the surface of a material. Deflections of the tip are detected by a laser that reflects off the backside of the tip, and the signal is sent to the computer that controls a set of piezoelectric materials that modulate the x, y, and z movements of the tip. In contact mode, as the tip raster scans across the surface, the z-piezo responds in such a way as to maintain the contact force between the tip and the sample by moving the tip up when it comes across a tall feature on the surface, and lowering the tip when it comes across a depression in the surface of the sample. In tapping mode, the tip is vibrated at its resonance frequency, and when the tip is either closer or farther away from the surface, there is a shift in the modulation frequency as van der Waals forces and electrostatic repulsion forces respectively act on the tip. The computer then adjusts

the z-piezo to maintain tip tapping amplitude and frequency in response to the surface morphology. This technique provides an image of the surface, and can help determine if the dopant is affecting the morphology of the OSC, which can sometimes be detrimental to the charge carrier mobility, or in other words, the speed at which a free charge carrier can move throughout the material.

By coating the AFM tip with a conductive metal such as doped diamond, platinum, or gold, the instrument can then also be used for electrical measurements. When the OSC sample is cast onto a conductive substrate, electrical contact can be made with the conductive substrate, and the AFM tip acts as the top electrode. A voltage is applied between the two electrodes as the tip raster scans across the surface, providing a map of both the current and the morphology simultaneously. This proved to be very useful in my work in Chapter 4, which details how the electrogenic bacteria *Geobacter sulfurreducens* can be used to de-dope CPE-K, a process that can be imaged and visualized using cAFM. cAFM was also employed in Chapter 2 to complete the picture for how thermal annealing can also be used to dedope certain polymers.

7. Current-voltage measurements

Current-voltage measurements have broad applicability and use to the study of how doped organic semiconductors' electrical properties are affected upon doping. By measuring the current at different applied voltages before and after doping, clear indications about the improvement of electrical properties can be obtained. To do so, the material under test needs to be placed, through spincasting or other method, between two metal electrodes. An instrument (source measurement unit or SMU) that can apply a voltage and measure the current flowing through the device is then connected to the two electrodes. In addition,

measuring the current-voltage relationship at different temperatures gives additional information such as the amount of energy needed for hopping transport in a particular amorphous organic semiconductor material. As a material is increasingly doped, the activation energy needed for hopping transport typically decreases, in line with an increase in the availability of sites for the hole to hop to.

Creating a device where the organic semiconductor is sandwiched between two electrodes on the top and bottom with a well-defined area also allows for the measurement of a material's mobility *via* space charge limited current (SCLC). A cautionary note should be added here, in that SCLC is only valid for materials in their undoped state, that the mobility is constant throughout the sample, and that the current is not limited by traps or energetic disorder. These assumptions along with others outlined in books and papers on the topic need to be taken into account when attempting to use Mott-Gurney's law and SCLC to measure a material's mobility. The reason for these assumptions is because the current in SCLC measurements is dominated by injected charge carriers, and thus mobility is independent of the charge carrier density. If there are traps or mobile free charge carriers due to doping, they will contribute to the measured current, and mobility will no longer be independent of the charge carrier density. When done correctly however, the mobility can be obtained, which is useful when computing the density of free charge carriers and by extension the doping efficiency.

8. X-ray reflectivity (XRR)

XRR is a technique that operates by sending X-rays to the sample at different angles and measuring the X-ray radiation that is reflected off of the sample back to the detector. At a certain angle called the critical angle, the intensity of the reflected X-ray radiation drops

rapidly, at a rate approximately equal to the $(angle)^{-4}$. The critical angle can then be used along with mathematical fitting to provide the density of the material.

XRR is important not so much for understanding the doping mechanism, but in obtaining information about the doping efficiency of a particular dopant. Because XRR measures the density of a material, the concentration of monomers in a particular volume can then be determined and used in calculations of the doping efficiency as described in Chapter 2 and Chapter 3 of this thesis.

9. Thermogravimentric analysis – mass spectroscopy (TGA-MS)

TGA-MS is a thermal analysis technique coupled with mass spectroscopy. The operational principle involves placing a sample of the organic semiconductor in a crucible, which is then heated to extremely high (up to 1000 ^{o}C) temperatures under an inert gas such as nitrogen. Anything that is volatized from the sample as it is heated is sent through to the mass spectrometer, which then analyzes the volatile species emitted from the sample after heating.

Use of TGA-MS has helped to support thermal annealing as a viable route for the dedoping of one of the OSCs studied in the course of this work. In addition, understanding the underlying thermal stability of various materials can help better understand the viable applications for that particular material.

D. Focus of this thesis

This thesis will cover Bronsted-acid doping, and the different ways it can be achieved from the perspective of both polymer structure and dopant properties. The role that sulfonate plays in making conjugated polyelectrolytes self-doping is elucidated. The change in electrical properties to the studied conjugated polyelectrolyte in various doping and dedoping conditions

are also examined. A unique method for de-doping of the conjugated polyelectrolyte will also be touched upon, and its chemical structure examined along with its electrical properties.

A shift in focus thanks to available funding leads to a study in the doping mechanism of a boron-based Lewis acid in Chapter 3, and how it affects the optical and electrical properties of different polymers that contain Lewis basic sites. Additional study on the doping efficiency and stability of different boron-based Lewis acids is also undertaken, with some surprising results.

Lastly, my first Ph.D. project on the visualization of electron transfer processes from bacteria will be covered in Chapter 4, which uses the same conjugated polyelectrolyte from Chapter 2. Combining the fact that the p-doped conjugated polyelectrolyte can be de-doped by electron transfer from bacteria along with the imagining capabilities of cAFM allows for a unique combination of the two to examine inefficiencies in bacterial transfer of electrons to the substrate both qualitatively and quantitatively. The overall experiment setup also provides a foundation for how future studies of electron-transfer species such as bacteria can be examined and studied.

Chapter 2 − Understanding the Doping Mechanism of CPE-K

A. Introduction to Conjugated Polyelectrolytes

Conjugated polyelectrolytes (CPEs) are structurally unique polymers in that they contain a π-conjugated backbone and pendant ionic groups which make the polymer soluble in water and polar solvents (Figure 2-1).[87,91]

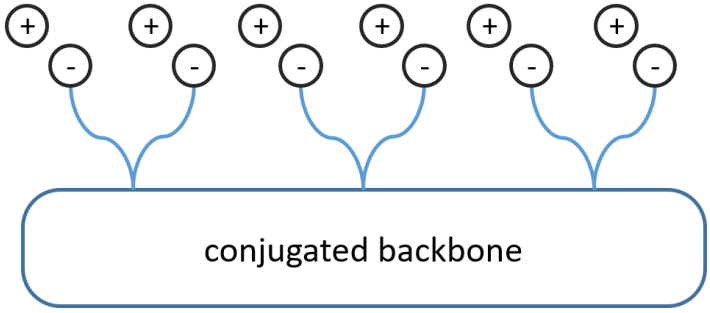

Figure 2-1. Schematic of conjugated polyelectrolytes

Pendant anionic side chains have also been shown to give CPEs the ability to be self-doped during purification in water due to the presence of protons, eliminating an extra processing step and the use of additional chemicals typically used in doping neutral conjugated polymers.[92] This self-doping property eliminates the need for adding external dopants such as F_4TCNQ, which has low solubility in organic solvents, often aggregates and prevents the doping of organic semiconductor materials to conductivity levels necessary for use in various device applications. The specific CPE poly[2,6-(4,4-bis-potassium butanylsulfonate-4H-cyclopenta-[2,1-b;3,4-b']-dithiophene)-alt-4,7-(2,1,3-benzothiadiazole)] (PCPDTBTSO3K or CPE-K) in particular has been shown to be doped in the mildly acidic conditions of ultrapure H_2O (Ω=18.3 MΩ*cm), allowing de-doping of the polymer *via* the addition of a base, while also allowing user tunability of the doping level by

adding the desired amount of acid – an important feature as controlling the doping level is at the heart of modern electronics.

CPEs have been used in a wide variety of applications such as biosensors, as an interlayer or a conductive buffer layer in organic and perovskite photovoltaics, as an interconnective layer between top and bottom cells in tandem organic solar cells, as the active layer in light-emitting electrochemical cells, to modify the injection barrier in OFETs, and in organic thermoelectrics.[93,94,103–110,95–102] CPEs have also been recently shown to act as p- or n-type dopants for carbon nanotubes, a property that is modulated by changing the charge of the ionic groups of the CPEs.[93] CPE/graphene hetero-bilayer 2D nanocomposites also exhibit a unique, temperature switchable type of electrical conductivity.[111] In summary, the ability to control the conductivity of CPEs, to dope the material during purification, and its pH neutral character can open the door to its use in a wide range of electronic and optoelectronic device applications from organic field effect transistors (OFETs) to organic photovoltaics (OPVs) and everything else in-between.

Yet, a more comprehensive understanding of the importance of sulfonate for the self-doping mechanism of CPE-K and its effect on charge transport and mobility is required to improve the use and design of this class of polymers. Many self-doped polymers dating back to the 1980s have made use of pendant sulfonate groups to achieve the self-doping property, without taking time to fully understand why sulfonate is needed.[83,84,113–117,85,87–91,99,112] To shed light on the role that pendant sulfonate groups play in the self-doping of this class of polymers, we probe doped and un-doped states of CPE-K with X-ray photoelectron spectroscopy (XPS), Fourier-transform infrared spectroscopy (FTIR), and ultraviolet-visible-near infrared spectroscopy (UV-vis-NIR) spectroscopy. In addition, we study the material's electrical

properties in the doped and un-doped states *via* a series of electrical measurements, provide an estimate of the doping efficiency with the help of X-ray reflectivity (XRR), and show another, unique method for the reversible doping and de-doping of this material.

B. Proposed structure of doped and de-doped CPE-K

Figure 2-2 shows the proposed doped and un-doped chemical structures of CPE-K, which was previously synthesized by Bazan *et al.*[92] Based on the below structures, several structural and chemical changes such as the reduction in potassium concentration and change in vibrational structure in the conjugated backbone of CPE-K should be noticeable upon doping.

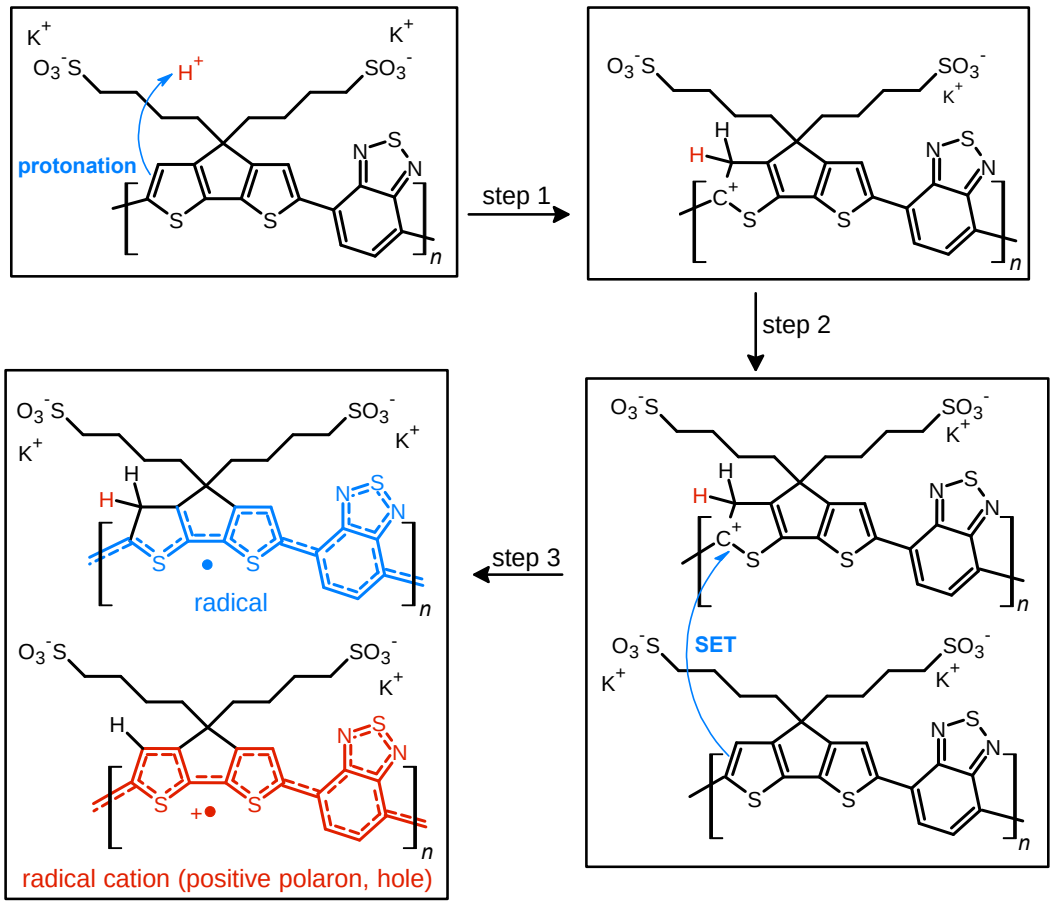

Figure 2-2. Chemical Structures of Doped and De-doped CPE-K

More specifically, upon protonation of the cyclopentaditiophene (CPDT) unit of the polymer,

a cation is formed in the conjugated backbone of the polymer. A neutral polymer chain can then undergo single electron transfer with the protonated polymer giving one polymer chain with a positive polaron and another polymer chain with an unpaired electron. This structural change will result in additional vibrational peaks for both polymer chains due to a loss in rigidity in the polymer backbone, which was previously enforced by the unbroken chain of sp^2 hybridized carbons in the backbone. The additional vibrational freedom experienced by the polymer results in new vibrational modes that are revealed through infrared spectroscopy. In addition, when doping occurs, the SO_3^- groups stabilize the radical cations (positive polarons or holes) on the backbone, thus eliminating the need for the K^+ counterions, a change that is detectable by XPS. While the K^+ ions are necessary to stabilize the SO_3^- groups in the undoped state of CPE-K, the K^+ ions are no longer necessary after the formation of holes on the polymer backbone and are likely solvated away by water molecules in solution. In the following sections, please note that "self-doped CPE-K" solution was prepared by dissolving the polymer in water and all "doped with H_2SO_4" and "de-doped CPE-K" solutions were prepared by the addition of 1 mole equivalent per sulfonate group of either H_2SO_4 or KOH to a solution of self-doped CPE-K.

C. X-ray photoelectron spectroscopy (XPS)

In the XPS analysis of CPE-K, we first start with CPE-K that has been de-doped by the addition of KOH to the self-doped CPE-K solution. When looking at the C 1s and K 2p high resolution spectrum, in theory de-doped CPE-K should have a 2:25 potassium to carbon atom ratio. However, XPS analysis of CPE-K in Figure 2-3 reveals a K 2p signal corresponding to a potassium to carbon atom ratio of approximately 4:25 in undoped CPE-K, which can be attributed to the addition of KOH beyond what was needed to de-dope the CPE-K solution.

One equivalent of KOH was added per sulfonate group; however, it is possible that the amount of KOH needed to de-dope the polymer was less than 1.0 equivalent of KOH per sulfonate group resulting in the higher than expected K 2p percentage seen in XPS due to not all of the monomer units being doped. In addition, very small crystallites of salt were seen on the surface of the film under magnification, suggesting the formation of KOH crystals that would explain the higher than expected K 2p signal. Washing the film with water in order to remove the salt crystals from the film would then also dissolve the film, thus XPS analysis was performed on the sample as is after spin casting.

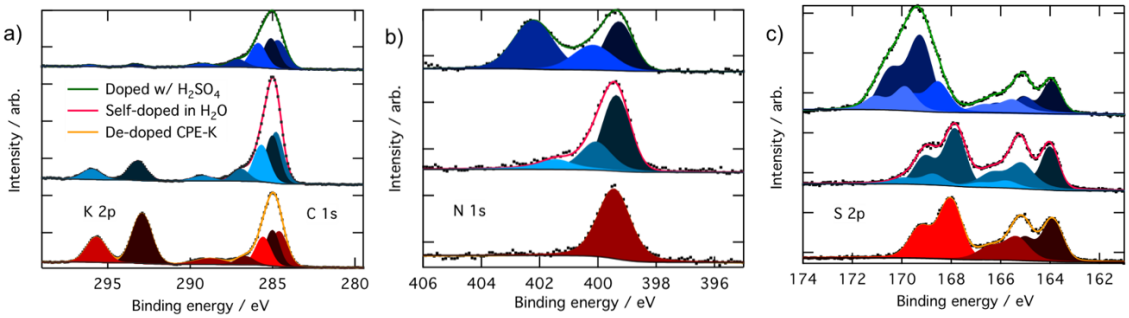

Figure 2-3. High resolution XPS spectra

CPE-K	K : C	C–N	C–S	C–C	C=C
Doped w/ H_2SO_4	0.4 : 25	2.1	5.9	6.8	8.1
Self-doped in H_2O	1 : 25	1.9	5.9	7.0	8.2
De-doped w/KOH	4 : 25	1.9	5.9	7.0	8.2

Table 2-1. Atomic Ratios of Elements from High-Res C 1s XPS spectrum

Upon doping of CPE-K, there is a clear reduction in the ratio of potassium to carbon as expected from 4:25 in dedoped CPE-K to 1:25 in CPE-K self-doped in H_2O, and to 0.4:25 in CPE-K doped with H_2SO_4 (Table 2-1). An additional table with a summary of all the atomic

percentages of the elements measured in the CPE-K film is shown in Table 2-2, which also shows the reduction in potassium percentage upon increased doping level. With an increase of holes in the backbone, the potassium ion is no longer needed to compensate for the pendant sulfonate groups as the sulfonate balances out the hole on the backbone.

	C 1s	N 1s	O 1s	S 2p	K 2p
w/ H_2SO_4	45.1 %	4.8 %	36.6 %	13.1 %	0.3 %
Self-doped	65.0 %	3.2 %	19.8 %	9.4 %	2.6 %
Un-doped	50.5 %	3.2 %	27.7 %	9.7 %	8.8 %

Table 2-2. Summary of XPS integrations from survey spectra of CPE-K

Protons from H_2SO_4 can also undergo an ion exchange reaction with potassium – the pKa of H_2SO_4 is approximately -3.0 while the pKa of the sulfonate moiety is > -2.6 allowing for such an ion exchange process to occur. To ensure the reduction in potassium percentage correlates with the addition of holes into CPE-K, we obtained additional high resolution XPS data of the XPS peaks in the C 1s and K 2p region of CPE-K before the final purification step in water, which means CPE-K has not yet been doped by water. Indeed, in the XPS spectrum in Figure 2-4, we see that un-doped CPE-K, whether before purification in water or after the addition of base to de-doped CPE-K, results in the same ratio of K to C atoms as measured by XPS. Table 2-3. Atomic percentages of C and K in Figure 2-4 provides a quantification summary of the data fromFigure 2-4. Lastly, the doublet K $2p_{3/2}$ peak at 293.2 eV and the K

$2p_{1/2}$ peak 296.0 eV agree with reported binding energies for K^+ from the National Institute of Science and Technology (NIST) database.[118]

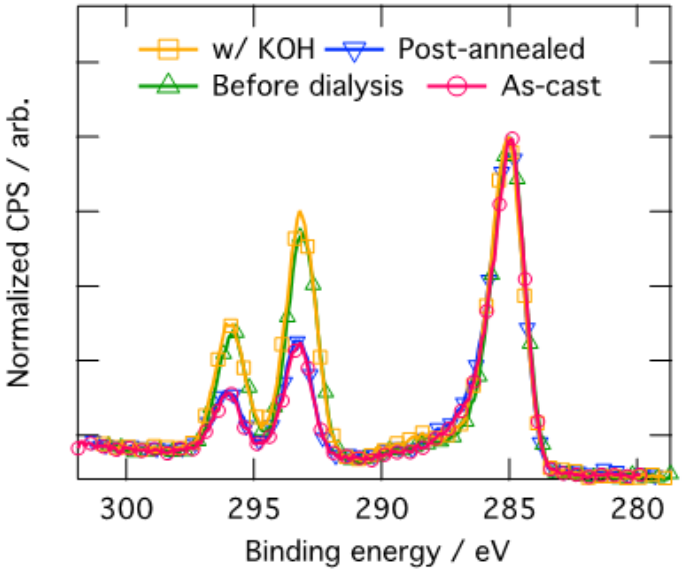

Figure 2-4. Normalized high-res C 1s XPS spectra of CPE-K under different doping conditions

CPE-K condition	Atomic % C	Atomic % K
As-cast	91.30	8.70
Post-annealed	90.67	9.33
Before dialysis	80.88	19.12
w/ KOH	81.56	18.44

Table 2-3. Atomic percentages of C and K in Figure 2-4

For the carbon signals, all of the C 1s high resolution peaks in Figure 2-3 were fit with four Voigt profiles consistent with four inequivalent carbons on CPE-K. The peak at 284.8 eV corresponds to carbons within the conjugated backbone that are bonded to other carbons (C=C), the peak at 285.0 eV corresponds to carbons on the alkyl chain that are bonded to other carbons (C–C), the peak at 285.7 eV corresponds to carbons bonded to sulfur atoms (C–S), and the peak at 286.9 eV corresponds to carbons bonded to nitrogen atoms (C–N), as expected from the chemical structure and previously described in literature.[119] From the chemical

structure, given the amount of each of these types of carbons in CPE-K, we expect a peak intensity ratio for CPE-K of 2:6:7:8 (C–N, C–S, C–C, C=C), which was indeed the ratio obtained from peak fitting (Table 2-1). The carbon peak at 289.2 eV is due to a shake-up satellite, which appears due to the energy loss of a photoelectron that has induced a $\pi \rightarrow \pi^*$ excitation during final state formation.[120,121]

The nitrogen high-resolution XPS spectra in Figure 2-3 shows one peak at 399.5 eV corresponding to the two chemically equivalent nitrogen atoms bound to a sulfur in undoped CPE-K, whereas the addition of holes into the backbone upon self-doping in H_2O results in the formation of higher binding energy peaks at 400.2 eV and 401.6 eV. The higher binding energy nitrogen peak at 400.2 eV corresponds to a radical cation nitrogen, as expected due to the presence of holes that appear after doping CPE-K. The peak at 401.6 eV is tentatively assigned to shake-up satellites, which typically appear a few eV higher in binding energy than the main element peak with an intensity of approximately 10% that of the main peak.[121,122] Upon further doping by the addition of H_2SO_4, an even higher binding energy peak appears at 402.2 eV, which corresponds to the protonation of the imine nitrogen in CPE-K by excess H_2SO_4.[113,117] As was the case with the addition of KOH, it is likely that excess H_2SO_4 was added beyond 1.0 equivalent per CPE-K sulfonate unit due to CPE-K having already been doped due to its self-doping properties.

In the undoped CPE-K S 2p spectrum, we can identify three chemically inequivalent sulfur atoms, as expected, with the 3/2 spin-orbit component peaking at 164.0 eV, 165.4 eV, and 168.1 eV binding energy (all doublets split by 1.18 eV with a 2:1 area ratio). The highest binding energy sulfur peak at 168.1 eV belongs to the sulfur on the sulfonate group as it is the most electron poor sulfur atom, while the sulfur at 165.4 eV belongs to the benzothiadiazole

unit. The lowest binding energy sulfur peak at 164.0 eV belongs to the thiophene, which is the most electron rich of the three sulfur atoms.[119,123,124]

Upon doping of CPE-K, additional peaks appear in the S 2p spectra. The peak centered at 166.5 eV can be attributed to more positively charged sulfur atoms in thiophene, while the peak centered at 170 eV is likely due to less electrostatically screened sulfur in the sulfonate ions. After the addition of 1.0 equivalent of H_2SO_4 per sulfonate group, an additional peak at a higher binding energy, i.e., 169.3 eV, appears as expected from a sulfur bound to four oxygen atoms, while also increasing the area percentages of the peaks belonging to electron deficient sulfur atoms on the polymer located at 165.9 eV and 169.0 eV, respectively, due to the increased doping. We attribute the overall higher binding energy of these sulfur species, compared to de-doped and self-doped samples, to different electrostatic interactions, as K cations seemingly better screen the sulfonate and polaron charges compared to the positive polarons, in accord with the different Madelung potentials of the differently doped polymers.[125] An even higher binding energy peak located at 169.9 eV is attributed to negatively charged sulfonate ions, whose electrostatic interaction with the protonated CPE-K polymer chains is particularly weak. As mentioned above, additional acid could have caused protonation beyond what could be stabilized by the sulfonate groups on CPE-K, resulting in CPE-K polymer chains with an overall positive charge that allow for an electrostatic interaction with SO_4^{2-} to occur.[126] This electrostatic interaction of the polymer chains causes increased polymer density and increased viscosity of the CPE-K polymer chains, which is supported by visually seeing the CPE-K solution thicken upon addition of sulfuric acid to the CPE-K solution. Additional doping of CPE-K *via* addition of 1 monomeric equivalent of H_2SO_4 to the solution reduces the solubility by about half. Lastly, a survey scan of CPE-K

after purification shows signals from only the elements expected from the chemical structure of CPE-K (**Figure S2**).

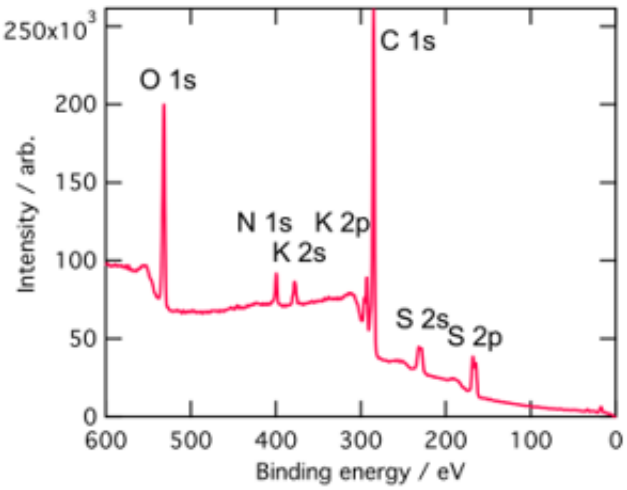

Figure 2-5. Survey XPS spectrum of self-doped CPE-K

D. Attenuated Total Reflectance-FTIR Spectroscopy (ATR-FTIR)

ATR-FTIR spectroscopy was used to investigate vibrational level changes in the polymer upon exposure of CPE-K to various sources of protons. Focusing on the fingerprint region of the IR spectra, which were obtained by drop casting solutions of CPE-K at various doping levels directly onto the ATR crystal, it is immediately clear that the spectrum of doped CPE-K contains an additional peak at 1300 cm^{-1} that the undoped CPE-K does not possess (Figure

2-6). In addition, CPE-K that has been annealed also does not have the peak at 1300 cm^{-1}, a finding which is discussed further in section 2.6.

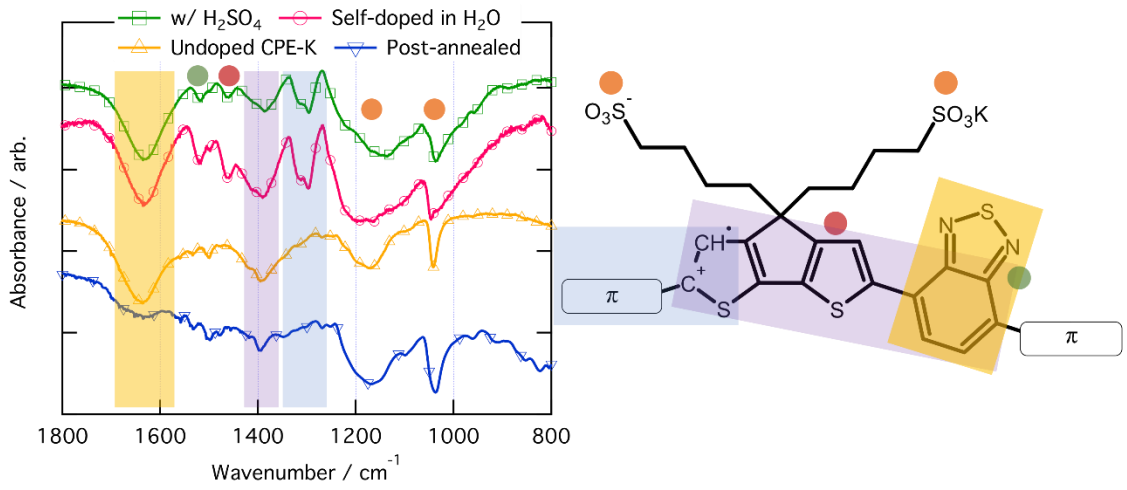

Figure 2-6. ATR-IR spectrum and corresponding functional group vibrations denoted by color on the chemical structure on the right

The peak at 1300 cm^{-1} is a crucial indicator of the doped CPE-K species, and it was assigned to an asymmetrical C-C stretch between the CPDT and benzothiadiazole (BT) portions of the CPE-K polymer. This peak at 1300 cm^{-1} only appears upon protonation of the CPDT unit.[127] Protonation of the CPDT unit at the location indicated by the red hydrogen in Figure 2-2 breaks the conjugation between the BT and CPDT units leading to an increase in vibrational freedom and the appearance of the new peak. Han and Elsenbaumer also suggested such a reaction occurs based on ^{13}C NMR data.[82]

In addition, the broad peak at 1200 cm^{-1} belongs to the asymmetrical SO_3^- stretch, which shifts to lower wavenumber upon increased levels of CPE-K doping. This is consistent with our hypothesis that SO_3^- is no longer interacting with the potassium counterion, but instead with a hole on the conjugated backbone of CPE-K, which was previously only hypothesized, but not proven. An interaction between the negatively charged oxygens of the sulfonate group

with the hole on the backbone would be more favorable from an atomic radii standpoint, and the hole on the backbone would draw out the oxygen away from the sulfur, leading to a longer S–O bond length and hence lower wavenumber.

E. UV-vis-nIR Absorption Spectroscopy

To ensure the material being analyzed is doped, which we take here to mean there is an increase in charge carriers which may participate in charge transport, we performed UV-vis-NIR measurements as seen in Figure 2-7, and coupled them with electrical measurements as outlined in Section F. The peak at 410 nm corresponds to π-π* absorption from localized π orbitals, while the higher intensity peak at 690 nm corresponds to the absorption from the intra-charge transfer (ICT) band.[128] The two lower energy peaks at 1100 nm and 2000 nm, respectively, are due to the formation of positive polarons on the polymer backbone.[129,130]

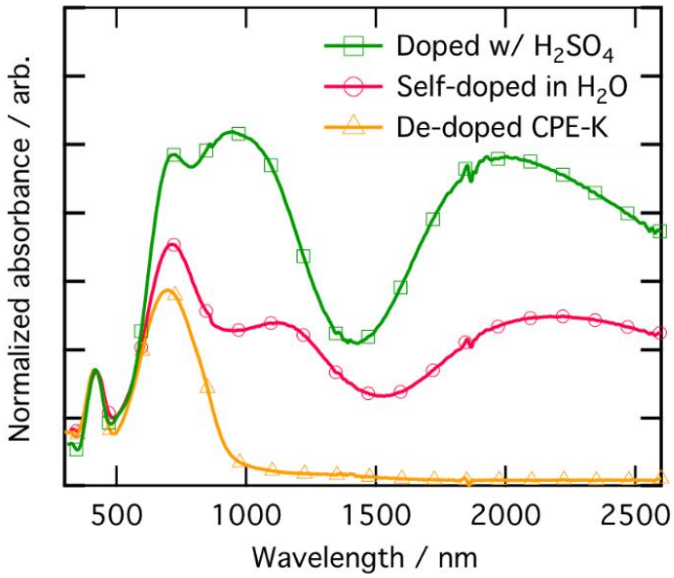

Figure 2-7. Normalized UV-vis-nIR of CPE-K films at various levels of doping

The UV-vis-nIR spectrum was fit for both the main electronic transitions as well as the polaron peaks and are shown in Figure 2-8. Sub-figure a) shows the UV-vis-nIR spectrum of CPE-K doped with H_2SO_4, b) shows self-doped CPE-K, and c) shows de-doped CPE-K. Quantification of the peak areas are shown as percentages in Table 2-4, confirming the increase in polaron peak intensity with doping of CPE-K. We also obtained solution UV-vis-nIR spectra of the polymer where we substituted out both of the pendant ionic side chains with two simple linear C_{16}-alkyl side chains (**Figure S4**). When the polymer consists of simple linear C_{16}-alkyl side chains as opposed to the sulfonate group, there is no doping upon addition of even 1000 monomeric equivalents of MilliQ water to the polymer, highlighting again the important role the sulfonate moiety plays in self-doping of CPE-K during purification of the material. In addition, previous work on studying doping in CPE-K has also shown that doping occurs in the presence of acid vigorously sparged to remove all the oxygen, which agrees with Han and Elsenbaumer's work.[128]

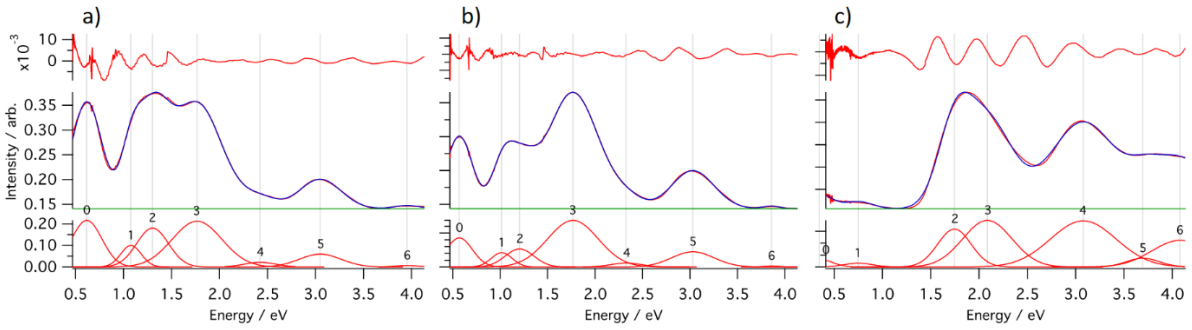

Figure 2-8. Gaussian peak fits to UV-vis-nIR spectra of CPE-K

Peak %	w/ H_2SO_4	As-cast	Un-doped
Electronic structure	49.3 %	76.4 %	92.3 %
Polaron bands	50.7 %	23.6 %	7.7 %

Table 2-4. Peak area percentages from Gaussian fits in Figure 2-8

F. Electrical Measurements

Temperature dependent conductivity measurements of CPE-K were performed using a parallel plane diode structure, with a channel length of 160 µm, and gold electrodes, which are close to the ionization potential of CPE-K thereby allowing for efficient charge injection into the material from the electrodes. By plotting the natural log of conductivity against inverse temperature to give the slope, the activation energy E_a was obtained by using equation (1).

$$ln\sigma = ln\sigma_0 - \frac{E_a}{k}\frac{1}{T} \quad (1)$$

where σ is conductivity, σ_0 is the conductivity at infinite temperature, plotted as the intercept on the graph, k is Boltzmann's constant, and T is absolute temperature in Kelvin. The decrease in activation energy from 272 meV to 117 meV (Table 2-5) upon increased doping is expected as with an increased concentration of charge carriers in the system, the Fermi level shifts towards the HOMO transport level allowing access to a greater density of states for holes to hop to.

CPE-K	Activation energy [eV][a)]	Conductivity [S/cm][b)]	Mobility, µ [$cm^2/V*s$]
w/ H_2SO_4	0.117 ± 0.007	0.140 ± 0.019	0.30[c)]
Self-doped in H_2O	0.159 ± 0.001	0.030 ± 0.003	0.24[c)]
De-doped w/KOH	0.272 ± 0.007	Below detection limit	2 x 10^{-8} [d)]

Table 2-5. Electrical Measurements of CPE-K Doped at Various Levels

The Arrhenius plot used to extract the activation energies is shown in Figure 2-9. The shift in the Fermi level towards the HOMO are supported by prior ultraviolet photoelectron spectroscopy (UPS) measurements which show an increase in the work function of the

material from 4.77 to 5.05 eV.[92] In addition, the conductivity of the material increases from below detection limit to 0.140 S/cm, and the mobility increases from 2 x 10^{-8} to 0.30 $cm^2/V*s$ upon doping. Particularly noteworthy is the dramatic seven orders of magnitude increase in the mobility of holes in the material, simply after self-acid doping during dialysis. Recent work on understanding excited state dynamics of CPE-K has shown that the polaron of CPE-K is delocalized into the frontier transport levels, which could contribute to its high conductivity.[131] The mobility of de-doped CPE-K was obtained from the SCLC region of the I-V curve with a vertical hole-only diode device. The mobility of both self-doped and doped CPE-K samples was obtained with Hall effect measurement as the mobility was too high for traditional measurements of organic semiconductor mobility *via* single-carrier diodes.

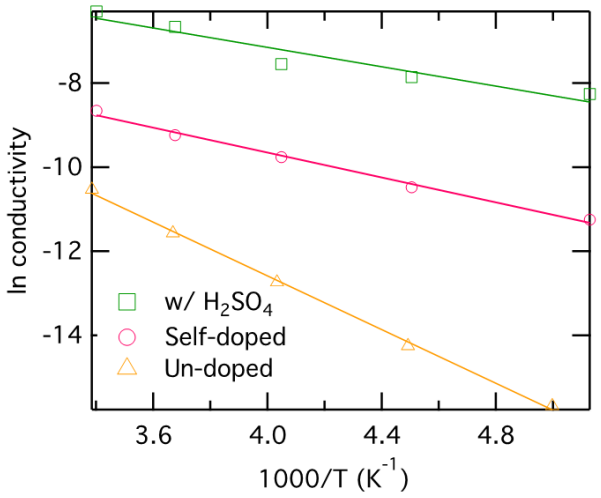

Figure 2-9. Arrhenius plot of CPE-K films at different doping levels

G. Estimation of CPE-K doping efficiency

From both the aforementioned electrical and optical measurements, the material's doping efficiency – that is, the number of free charge carriers generated per dopant molecule – can be estimated. In traditional doped organic semiconductors that use dopants such as F_4TCNQ,

which are known to undergo 1:1 integer charge transfer with the organic semiconductor, it is straightforward to know the number of dopant molecules added to the system. However, as outlined above, the dopant for CPE-K is protons, and as a result, doping efficiency is a lot trickier to calculate and depends on additional factors such as molar concentration of CPE-K, proton concentration, and volume of solution.

In this manuscript, doping efficiency was estimated by obtaining an estimate of the monomer density in a film of CPE-K along with an estimate of the free charge carrier density, then taking a ratio of the two values. The density of CPE-K, obtained by X-ray reflectivity, was measured to be 1.30 g/cm^3. Given the molar mass of a single monomer unit of CPE-K of 722.10 g/mol, the estimated monomer density in the film was obtained to be 1.08 x 10^{21} monomers/cm^3. By then using the conductivity and mobility values measured, the free charge carrier density can be obtained using equation (2)

$$\sigma = nq\mu \tag{2}$$

where σ is the measured conductivity in S/cm, q is the elementary charge of an electron, μ is the mobility in cm^2/V·s, and n is the free charge carrier density in cm^{-3}. Using the conductivity and Hall effect mobility values from CPE-K self-doped in H_2O in Table 3, n was calculated to be 2.88 x 10^{18} holes/cm^3. Taking the ratio of the two values gives a doping efficiency of 0.266 %, assuming that a single proton results in the creation of a single hole, which is a relatively safe assumption given the structural changes that occur in CPE-K upon doping as previously outlined. Addition of H_2SO_4 does not increase the measured free charge carrier density, but instead increases the mobility by an order of magnitude, thus increasing the conductivity by an order of magnitude as well. While the doping efficiency value is very low for organic semiconductors, it is important to note that this is an estimate, and that this

estimate is based on electrical measurements which provide the free charge carrier density. The free charge carrier density is arguably a more useful estimate of doping efficiency than simply the number of uncompensated acceptor centers, because the number of free charge carriers is directly related to the conductivity of the material whereas uncompensated acceptor centers do not necessarily lead to free charge carriers. In addition, because the dopant is a proton, and water is a ubiquitous solvent, CPE-K can be more readily doped even with limited scientific resources when compared to organic semiconductors that require the use of an external dopant molecule. We would also like to point out that despite the same free charge carrier density as estimated *via* electrical measurements, the disparity in UV-vis-nIR spectra between self-doped CPE-K and CPE-K doped with H_2SO_4 can be attributed to the formation of additional holes as discussed previously in the XPS section. These additional holes are immobile due to the presence of SO_4^{2-} from H_2SO_4, which coulombically interact with the additional holes to electrostatically bind the CPE-K chains together, causing a sharp increase in viscosity, which was visibly apparent. However, despite being bound holes that cannot contribute to electronic transport, they can still absorb light, thus increasing the polaron absorption peak in the UV-vis-nIR spectrum. These trapped holes are also responsible for the blue-shift in the polaron peaks as close proximity of the SO_4^{2-} anion localizes the polaron, causing the blue-shift.[132,133] Despite the low doping efficiency, the abundance of protons present in water along with the electrical transport characteristics of CPE-K are such that the material is still used for a wide variety of organic electronics such as biosensors, interlayers in organic photovoltaics, as the active layer in light-emitting electrochemical cells, and in organic thermoelectrics, acting as a replacement for PEDOT:PSS in some of these cases.[93–102]

H. Reversible de-doping of CPE-K by annealing

Over the course of this study, all of the undoped CPE-K measurements were performed with CPE-K that has been de-doped through the addition of base, specifically KOH. However, there is another way to de-dope the polymer: *via* thermal annealing. Thermally assisted de-doping of a conductive polymer has also been seen in sulfonic acid ring-substituted polyaniline, in which the proposed mechanism was elimination of some sulfonic acid groups.[117] In that particular case, the authors Chen and Hwang claimed the thermally assisted de-doping was partly irreversible due to a change in the chemical structure of the conjugated backbone. In another example using a sulfonated derivative of polythiophene, the authors also see thermal de-doping – however in this case the de-doping is completely irreversible due to decomposition of the polymer.[90] In the case of CPE-K, thermal de-doping is a reversible process as explained below. One of the reasons for this is heating the CPE-K film up to 300 ^{o}C does not cause the loss of sulfonate groups as seen in thermal gravimetric analysis-mass spectrometry (TGA-MS) data, suggesting the mechanism for de-doping of the CPE-K film does not involve the loss of sulfonate side groups as that ion is not seen in the mass spectrum. Residual water in the film is driven off during annealing as seen from the TGA-MS data up until temperatures above 450 ^{o}C, at which point the CPE-K film degrades leading to the

oxidation of the polymer into carbon dioxide (Figure 2-10). No other products are evolved during the entire TGA-MS run aside from water up until 300 ºC.

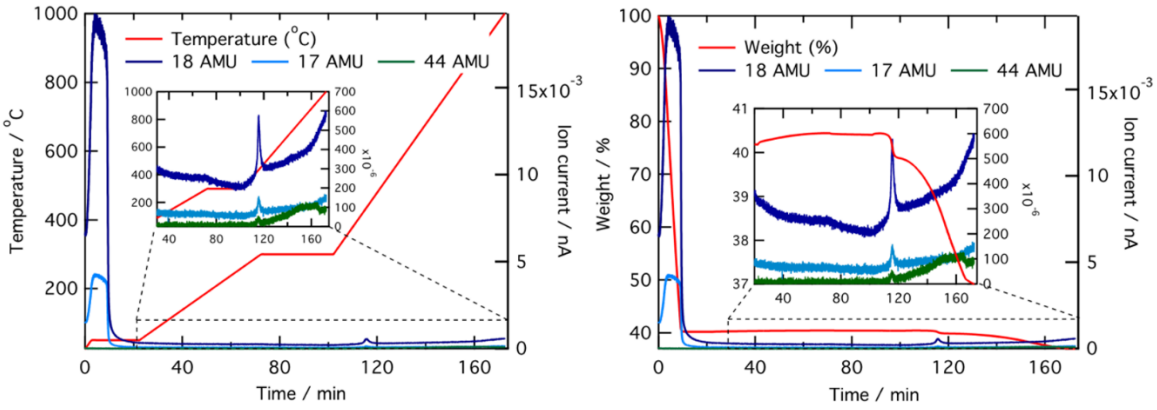

Mass (AMUs)	18	17	44
Compound	H_2O	^{-}OH	CO_2

Figure 2-10. TGA-MS of self-doped CPE-K showing loss of H_2O upon heating

As seen in Figure 2-11, annealing CPE-K for 30 minutes under a nitrogen atmosphere results in a reduction of the polaron absorption band of the polymer with increasing temperatures monitored by UV-vis-NIR.

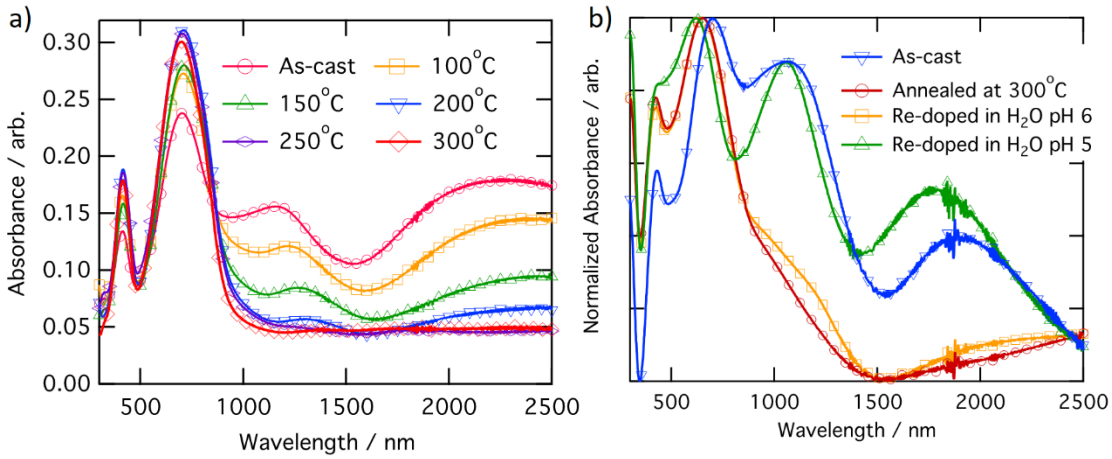

Figure 2-11. UV-vis-nIR absorption spectra of CPE-K after annealing and re-doping in H_2O

IR spectroscopy of an annealed CPE-K film also shows the same vibrational structure as seen in CPE-K de-doped by KOH (Figure 2-6), which means CPE-K before doping and CPE-K that has been de-doped *via* thermal annealing result in the same chemical structure. In addition, the lack of a strong absorption at 1635 cm^{-1} in the post-annealed spectrum of CPE-K corresponds to the loss of H_2O. De-doping of CPE-K through loss of water can also be seen in various I-V measurements both in nanoscale and in bulk measurements. Nanoscale I-V measurements are obtained *via* conductive atomic force microscopy (cAFM), which operates by applying a bias to the conductive substrate, in this case indium tin oxide, while raster scanning a gold or platinum/chromium coated silicon AFM tip in contact mode across the surface of the sample. In doing so, a morphology and current image of the thin film can be obtained simultaneously, allowing for precise mapping of the morphology and current of semiconductor films. cAFM measurements of CPE-K annealed for 30 minutes, at the same temperatures used for UV-vis-NIR, show a decrease in the average current across the film with no difference in surface morphology (Figure 2-12, Figure 2-13). Seeing a decrease in average current across the film without a change in the surface morphology is important as it means the reduced current in the film is due to the aforementioned changes in chemical structure and composition, and not on film surface morphology. In Figure 2-13, images on the left show the morphology (top) and current (bottom) pre-annealing, while the images on the right show morphology and current post-annealing.

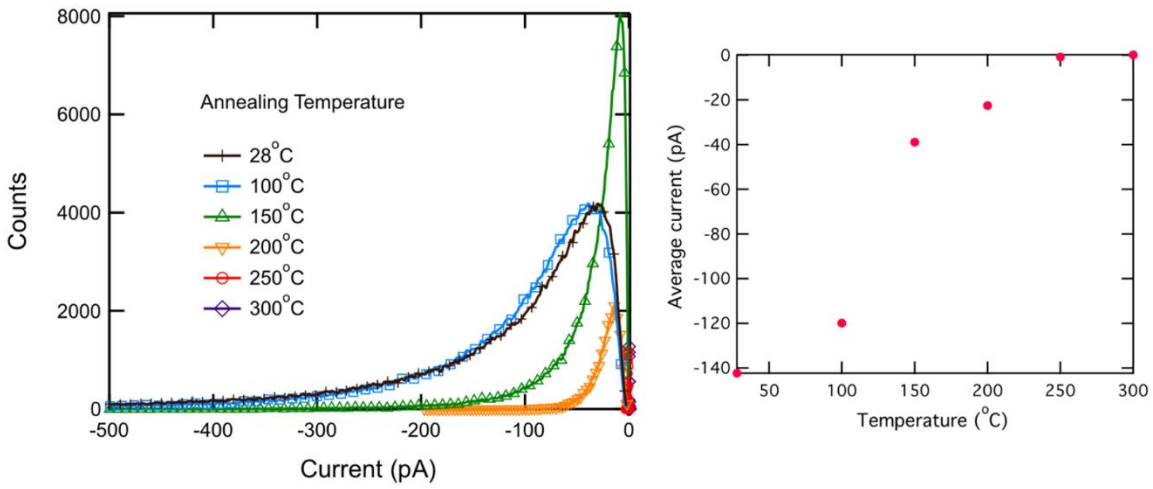

Figure 2-12. Histogram of cAFM current distribution with annealing

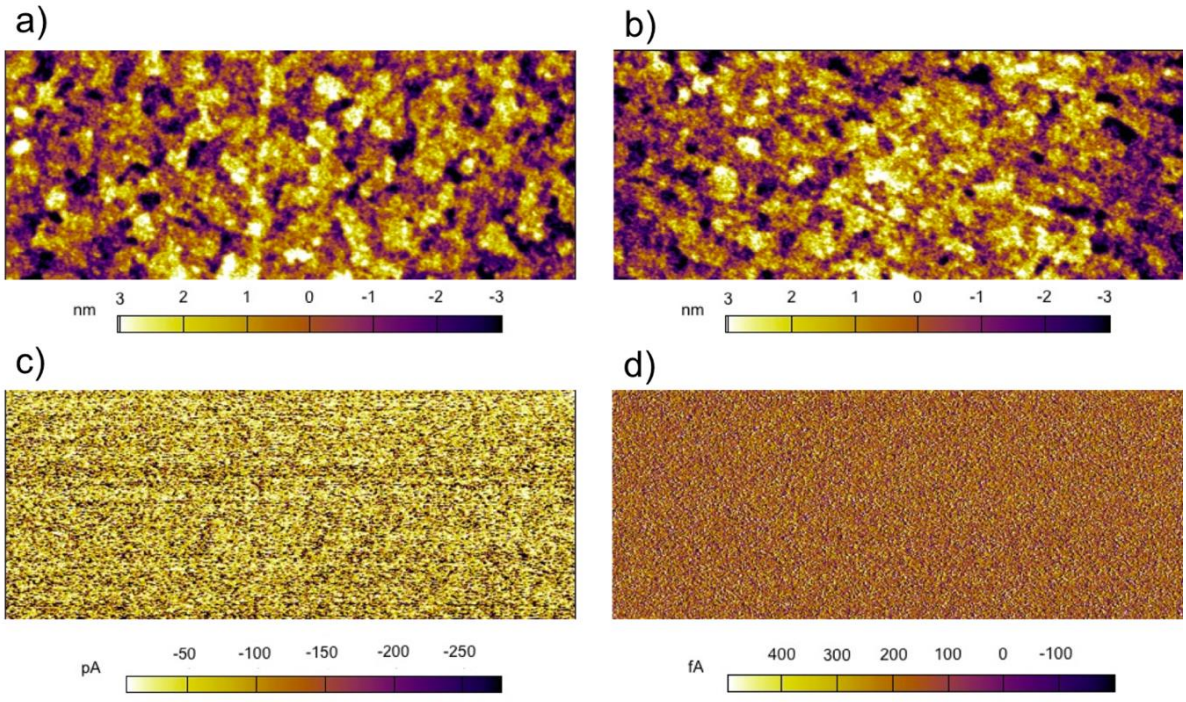

Figure 2-13. Film morphology and current distributions of CPE-K films pre- and post-annealing

Increasing the temperature of an as-cast film under vacuum while measuring bulk I-V curves across two parallel plane electrodes, set in the same configuration as were used for temperature dependent conductivity measurements in Section 2.4, shows a slight increase in

the current until 147 ^{o}C, at which point the current decreases. Allowing the film to sit at 147 ^{o}C under a vacuum of 1 x 10^{-9} torr overnight dramatically reduces the current seen in the film when analyzed the following day (Figure 2-14). The ohmic nature of the I-V curves at all temperatures in the figure reflect the intrinsically high conductivity of self-doped CPE-K.

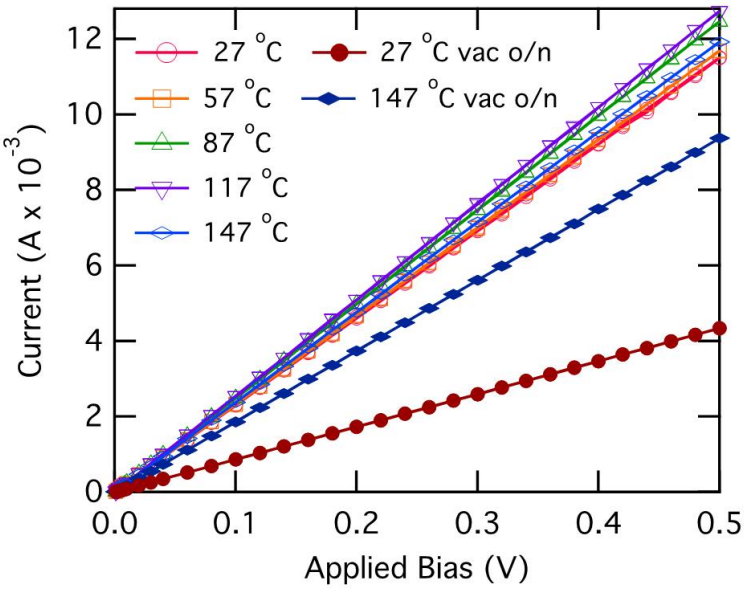

Figure 2-14. I-V curves of CPE-K obtained under vacuum at different temperatures

Temperature dependent conductivity measurements confirm the experimental evidence described previously. After obtaining conductivity measurements at different temperatures, an Arrhenius plot (Figure 2-15) was created. Different CPE-K films were annealed for 30 minutes at varying temperatures, and revealed that with an increase in annealing temperature, the activation energy for charge transport also increased, which is consistent with de-doping of CPE-K.

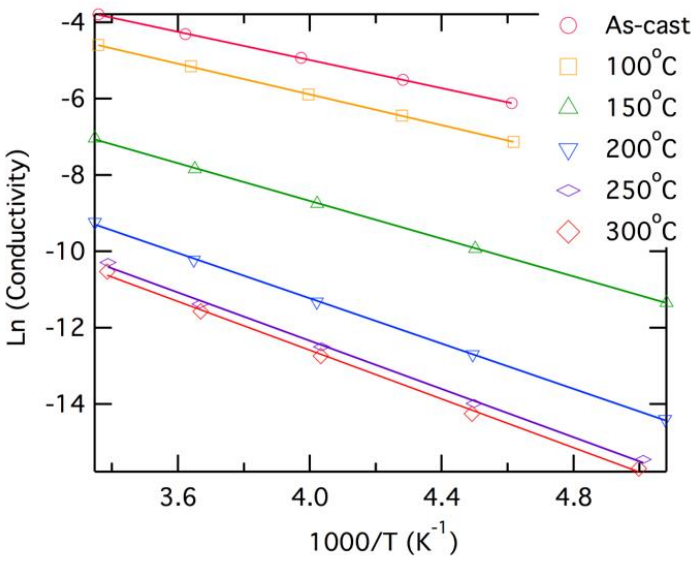

Figure 2-15. Arrhenius plot of annealed CPE-K films

CPE-K film	Activation energy (eV)
AC	0.159 ± 0.001
100°C	0.174 ± 0.001
150°C	0.213 ± 0.002
200°C	0.256 ± 0.003
250°C	0.272 ± 0.007
300°C	0.272 ± 0.007

Table 2-6. Charge transport activation energy at various annealing temperatures

By briefly submerging a CPE-K film that has been annealed at 300 °C in vigorously degassed water of pH = 5 or lower under oxygen-free conditions in an anaerobic chamber, the polaron signature returns in the UV-vis-NIR spectrum in Figure 2-11 without dissolving the polymer. Signals corresponding to the mass of SO_2 and SO are evolved from the polymer at temperatures starting around 300 °C (Figure 2-16). This suggests the crosslinking of some, but not all of the CPE-K polymer chains *via* the sulfonate moiety in a Friedel-Crafts type addition reaction, reducing the overall water uptake efficiency throughout the bulk of the film

thereby making it resistant to dissolution in water.[134] This experiment also shows that the presence of oxygen is not required for doping of CPE-K. However, leaving the polymer in water for a longer amount of time (> 5 minutes) will result in its dissolution. This thermally activated, reversible de-doping process is in itself an interesting finding, opening CPE-K to additional versatility in devices which require biological applications.

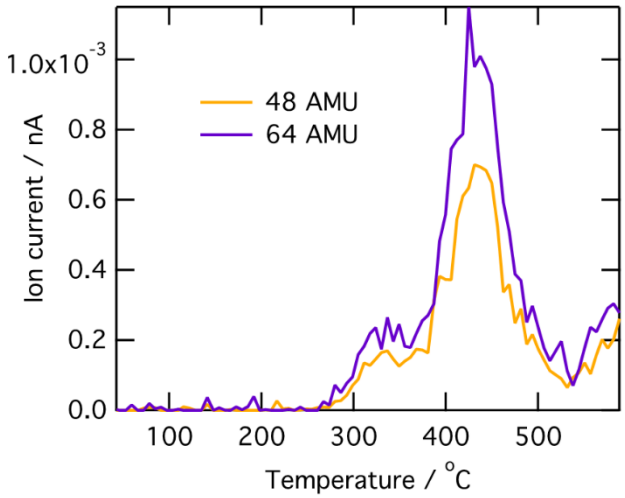

Figure 2-16. TGA-MS of self-doped CPE-K showing formation of SO_2 and SO

I. Experimental Section

1. Solution preparation

CPE-K solutions were prepared by dissolving previously doped CPE-K into Millipore H_2O, and sonicating the solution until the solids were dissolved. An equal volume of methanol was added, the solution was further sonicated, then filtered through a 0.45 μm PTFE filter before use. To obtain undoped CPE-K, 1.0 equivalent of KOH relative to the concentration of the monomer unit was added to the solution before use. To obtain "w/ H_2SO_4" solutions, 1.0

equivalent of H_2SO_4 relative to the concentration of monomer unit was added to the solution before use. Both the KOH and H_2SO_4 solutions were at a concentration of 2.19 M.

2. XPS

All x-ray photoelectron spectroscopy measurements were obtained on using a Kratos Axis Ultra DLD XPS under vacuum (10^{-8} Torr) using monochromated x-rays produced using an aluminum source running at a potential of 14 kV. A pass energy of 20 was used for all high-res element sweeps. The CPE-K samples were spuncast onto cleaned conductive indium tin oxide/glass substrates. The films were mounted onto a sample bar using double-sided tape, and electrically grounded to the sample bar using nickel impregnated tape. Peak fitting was performed using WINSPEC, and atomic sensitivity factors for each element were taken into account during peak integrations.

3. ATR-FTIR

Infrared spectroscopy measurements were obtained on a Thermo Nicolet iS10 FTIR Spectrometer by drop-casting the CPE-K solution and allowing it to dry before measurement. A baseline correction was performed on the data.

4. UV-vis-nIR

All UV-vis-NIR spectra were obtained using a Perkin-Elmer Lambda 750 UV-vis-NIR spectrometer using a tungsten lamp for the visible to near-IR region and a deuterium lamp for the UV region. A 100% transmission blank was obtained using a clean indium tin oxide/glass substrate for all spectra.

5. Electrical measurements

All electrical measurements with the exception of the Hall effect measurement were performed under vacuum (10^{-7} Torr) using a Keithley 4200 semiconductor analyzer. Conductivity values were obtained by linear four-point probe measurement. The geometrical parameter S of the electrodes, which takes into account electrode length and thickness, is 1.3 x 10^{-4}, allowing for calculation of σ by equation 1

$$\frac{dI}{dV} = \sigma S \qquad (1)$$

where I is current in amperes and V is voltage. Activation energy values were obtained using devices in a simple lateral diode configuration with a geometrical parameter of 6.5 x 10^{-4} cm, also measured under vacuum using a Keithley 4200 semiconductor analyzer. The van der Pauw method was used in order to measure the Hall effect. It is a widely used method for measuring the Hall effect in thin films and two-dimensional materials.[135,136] The measurements of the Hall effect were carried out in a vacuum of 10^{-5} mbar. The magnetic field strength B and the electric current I were set to 0.63 T and 50 μA, respectively. Each experimental value of the Hall voltage V_H was averaged by 15 successive measurements. The measurements of V_H were carried out at different directions of electric current and orientations of the magnetic field in order to cancel out parasitic effects.

6. XRR

Solution of CPE-K self-doped in H_2O was spuncast on a clean glass substrate to obtain a thin film of approximately 25 nm. The density of the CPE-K thin film was then determined by X-ray reflectivity measurements using a Rigaku Smartlab High-Resolution Diffractometer and accompanying reflectivity fitting software (GXRR3).

7. Conductive-Atomic Force Microscopy (cAFM)

All topographic and current measurements were obtained using an Asylum MFP-3D operating in closed loop mode mounted atop an Olympus inverted optical microscope under an inert atmosphere. Pt/Cr coated silicon AFM tips with a resonant frequency of ~13 kHz and a force constant of ~0.2 N m^{-1} were used (Budget Sensors). All images were obtained at a force of 2nN to ensure a constant electric field across all measurements. First order image flattening was performed on the morphology images on Asylum Research AFM software version 10, programmed using IGOR Pro.

8. Thermogravimetric-mass spectrometry (TGA-MS)

Themogravimetric-mass spectrometry analyses were performed on a Discovery TGA housed at University of California, Santa Barbara's TEMPO facility, located within the materials research laboratory (MRL). Samples were placed in an AlO_2 crucible, which was placed onto a high-temperature platinum pan and analyzed under a nitrogen atmosphere. Temperature ramps were performed at a speed of 10^{o}C/min. Mass spectrometry data was collected using Process Eye software. TGA data was collected using TRIOS, and analyzed along with MS data using TRIOS, developed by TA Instruments.

Chapter 3 − Lewis Acid Doping

A. Introduction to work on Lewis acids

Lewis acids are defined as being species which accept a lone pair of electrons, often through an empty p-orbital. Lewis bases are the opposite, in that they donate an available pair of electrons. The most well-known example of these species is found through the combination of the Lewis acid BF_3 and the Lewis base NH_3, forming the Lewis acid-base adduct BF_3—NH_3 as seen in Figure 3-1.

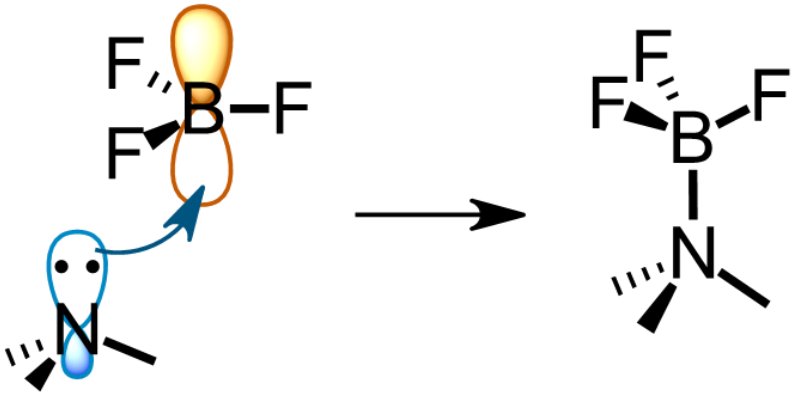

Figure 3-1. Lewis acid-base reaction schematic

Lewis acids stand in contrast to Bronsted acids, which function through the donation of a proton to a Bronsted base. Lewis acids have found wide-spread use in synthesis, having been used for decades as a catalyst for a wide range of reactions such as Friedel-Crafts, aldol, Diels-Alder, and other carbon-carbon bond forming reactions.[66,69,137–140] However, we will focus on the use of Lewis acids for doping, with one of the earliest reports coming in 1999. The Lewis acid tin (IV) chloride was added to polyaniline, resulting in an increase in conductivity of polyaniline to values of 10^{-3} S/cm.[141] However, the reported conductivity is 5-orders of

magnitude lower than when polyaniline was doped with Bronsted acids, which could have contributed to the lack of research in using Lewis acids for doping following that work.

Renewed interest in using Lewis acids for applications involving organic semiconductors began in the early 2010s when the Bazan group found that Lewis acids can shift the bandgap of organic semiconductors, thus changing their absorption and emission spectra. A secondary benefit to using Lewis acids is the post-synthesis modification of the bandgap, which is experimentally much more straightforward than synthesizing new small molecules and polymers from starting materials. Lastly, the work by Bazan's group also showed that the strength of Lewis acids affected the degree to which the bandgap was shifted.

Following these initial findings, more research was published showing how Lewis acids, specifically tris(pentafluorophenylborane) (BCF), could be used to dope organic semiconductors, thus improving electrical parameters such as the mobility and conductivity. While applications for the use of organic semiconductors doped with Lewis acids increased in number, a fundamental understanding for how Lewis acids were able to change bandgaps, mobilities, and conductivity remained unknown. Intensive collaborative efforts began to understand the doping mechanism of Lewis acids, which led to findings that showed a shift in bandgap of the organic semiconductor is due to the formation of Lewis acid-polymer complexes *via* direct binding of the Lewis acid with a Lewis basic site on the polymer.[71] Doping of the studied organic semiconductors on the other hand is due to Bronsted-acid doping, where protonation of the polymer backbone is then followed by single electron transfer between a protonated polymer chain and a neutral polymer chain to create a polymer chain with a mobile polaron that can contribute to increasing the conductivity of the polymer, as shown in Figure 3-2.[72]

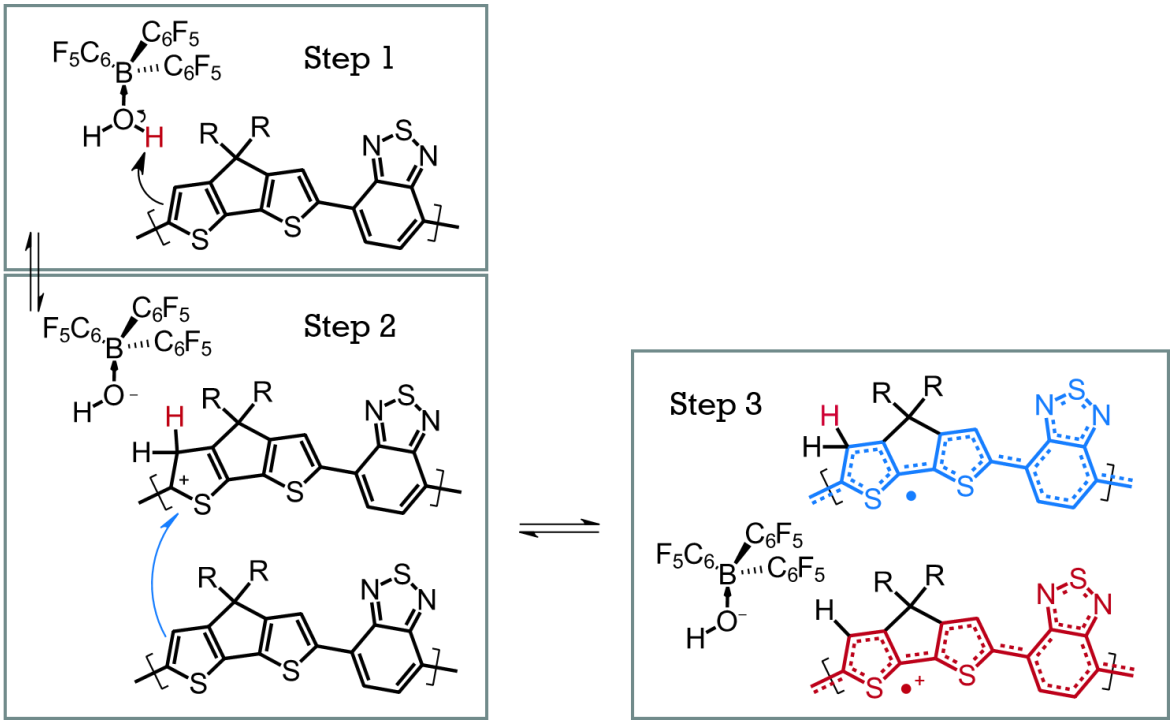

Figure 3-2. Doping mechanism of BCF and PCPDTBT

Understanding the doping mechanism of Lewis acids was intended by my advisor to be a separate chapter in my thesis, however a former student chose to co-opt the project for himself without letting anyone else know. Therefore, my attention shifted to following up on this work by looking into how Lewis acid strength affects the doping efficiency.

Traditional, textbook definitions of Lewis acid strength rely on an understanding that there are two competing processes at play. The first is the electronegativity of the elements attached to the electron-deficient atom. The second is the amount of π−backbonding that can occur between the attached elements and the electron-deficient atom. Let us take for example the Lewis acids BF_3, BCl_3, and BBr_3. Based on electronegativity values alone, one could speculate that due to the electronegativity of fluorine, that the boron atom of BF_3 would be the most electron deficient, and therefore BF_3 would be the strongest Lewis acid of the three, and BBr_3 would be the weakest. However, the size of the valence orbitals on boron and fluorine on BF_3

are much closer to each other than the size of the p-orbitals on boron and bromine on BBr_3, which allows for greater π−backbonding from the fluorine to the boron atom in BF_3 than from the bromine to the boron atom in BBr_3, thus resulting in BF_3 being in reality the weaker Lewis acid (Figure 3-3).

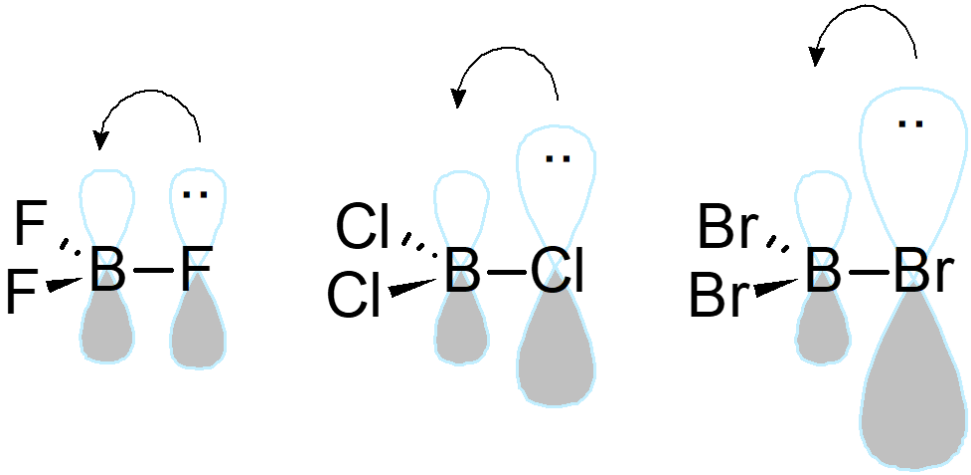

Figure 3-3. π−backbonding to empty p-orbital on boron atom

Experimental measurements of Lewis acidity show some similar trends with what is predicted in organic chemistry textbooks. A study looking into the ^{1}H NMR downfield shifts of the aldehyde and methyl protons of DMF upon binding with various Lewis acids showed that of the Lewis acids BF_3, BCl_3, and BBr_3, the expected trend in Lewis acid strength where BF_3 is the weakest and BBr_3 is the strongest holds true.[65] A second paper that also measures Lewis acid strengths but by fluoride ion affinity also shows the expected trend for BF_3, BCl_3, and BBr_3, and furthermore, says that BCF is the strongest of the four boron based Lewis acids mentioned in this introduction.[142] However, another paper that examined the strength of Lewis acids by examining the downfield shift of the ^{31}P NMR signal showed BCF being the weakest of the four boron based Lewis acids.[143]

Given these Lewis acids and their different strengths, the question then arises if stronger Lewis acids also result in greater doping efficiency. Because the Lewis acid doping mechanism first involves the formation of a complex where the water molecule is bound to the Lewis acid followed by protonation of the polymer by the Lewis-acid-water complex, in theory stronger Lewis acids will also create stronger (more acidic) Bronsted-acids. An increase in the number and strength of doping complexes should in theory increase the doping efficiency to a maximum of 50 %, though in reality reaching such doping efficiencies is hindered by the presence of traps, the relative acidity and basicity of the Lewis acid and polymer, and sterics.

B. Choosing of polymer and dopants to study

1. UV-vis-nIR Absorption Spectroscopy

During the course of our collaborative study into Lewis acid dopants, one of the findings as briefly touched upon above is that the processes of binding of the Lewis acid molecule to the polymer, which shifts the bandgap, and doping, which increases the number of available free charge carriers for transport, are two separate processes. In addition, the processes occur on different timescales, as shown in Figure 3-4. Solution UV-vis-nIR absorption spectroscopy of PCPDT-PT, which contains a Lewis basic pyridyl nitrogen, shows formation of an adduct with BCF, thus shifting the bandgap of the polymer on a very rapid timescale. On the other hand, PCPDT-BT, which does not contain the pyridyl nitrogen, only gets doped by BCF, with the process occurring on a much slower timescale than adduct formation. These processes are also reversible—with the addition of pyridine *in situ*, there is a rapid change back to the original spectrum for PCPDT-PT, indicative of the pyridine outcompeting the pyridyl nitrogen

for binding to the BCF. When pyridine is added to a solution of PCPDT-BT, there is only a slow change in absorption that does not completely resolve itself and return the spectrum of PCPDT-BT back to its original native state due to PCPDT-BT now being doped, which pyridine alone cannot reverse. Film UV-vis-nIR absorption spectroscopy data also shows a shift in the bandgap of PCPDT-PT, and only doping but no shift in bandgap for PCPDT-BT.

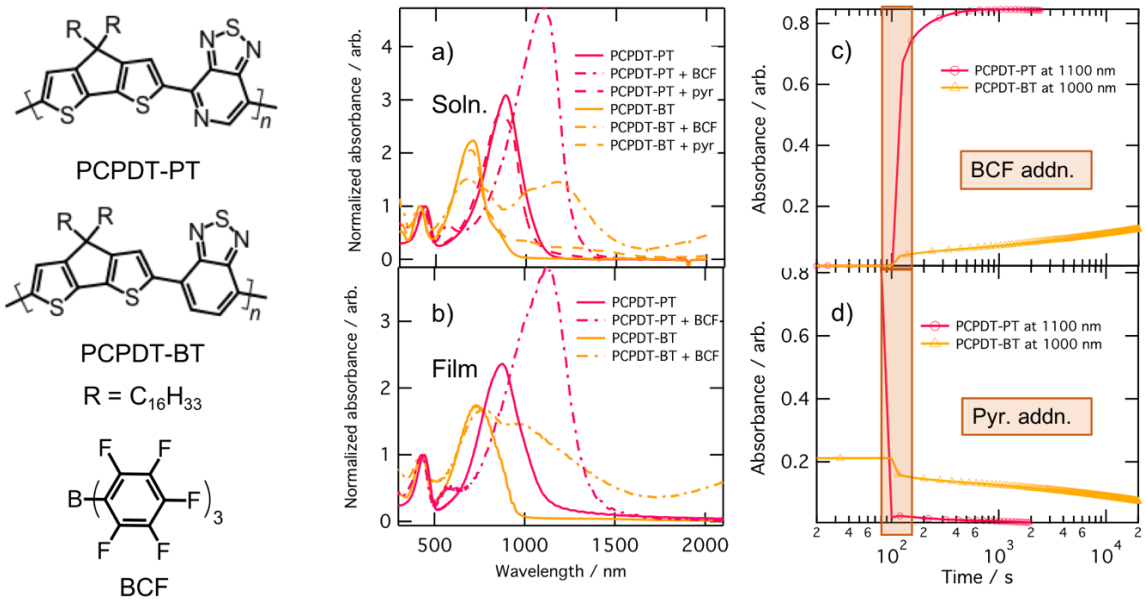

Figure 3-4. Polymer and Lewis acid structures, UV-vis-nIR absorption spectra, and kinetics data

2. XPS

XPS data also supports the conclusion that BCF binds to only the pyridyl nitrogen.

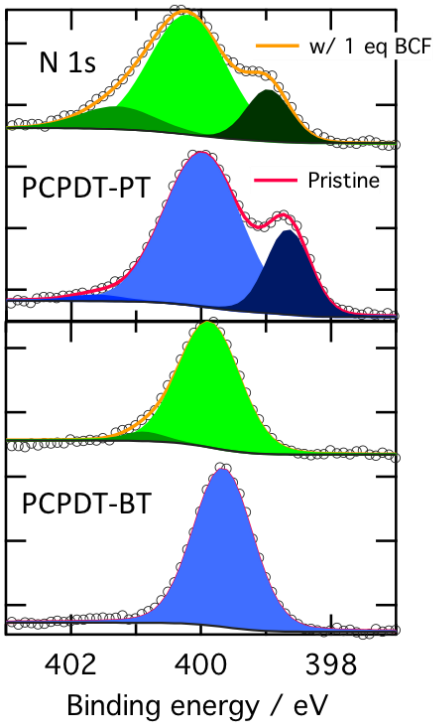

Figure 3-5. High-resolution N 1s XPS spectra of polymers with and w/ out BCF

In Figure 3-5, which is a high-resolution scan of the N 1s peak, a peak-fitting routine was employed to deconvolute the main envelope to provide us with two Voigt profiles in PCPDT-PT, and only one Voigt profile in PCPDT-BT, which is consistent with the chemical structure of the polymers. There are two chemically inequivalent nitrogens in PCPDT-PT, whereas there is only one nitrogen atom in PCPDT-BT leading to the peaks seen in the pristine N 1s scan. After the addition of 1 equivalent of BCF, a clear reduction in peak area of the lower binding energy peak in PCPDT-PT is seen, along with the presence of a higher binding energy peak at approximately 401.5 eV. These changes are indicative of BCF binding to the pyridyl nitrogen that leads to a more electron deficient nitrogen atom that shows up as a higher binding energy peak. In PCPDT-BT, a small shoulder shows up at 401 eV upon addition of BCF that is attributed to the formation of holes along the polymer backbone after addition of BCF. As

detailed below, BCF addition to CPDT containing polymers increases the concentration of holes *via* doping. Because holes can be delocalized along the backbone, they also lead to lower electron density for the nitrogen atoms, which causes the small shoulder at high higher binding energy. XPS survey scans confirm the presence of BCF in the film *via* the fluorine peak located at 688 eV, and rules out the presence of unexpected elements. High-resolution C 1s XPS scans also confirm the presence of BCF (Figure 3-6). In addition, high-resolution S 2p XPS spectra of the polymers show no difference between the pristine polymers and the polymers w/ BCF added.

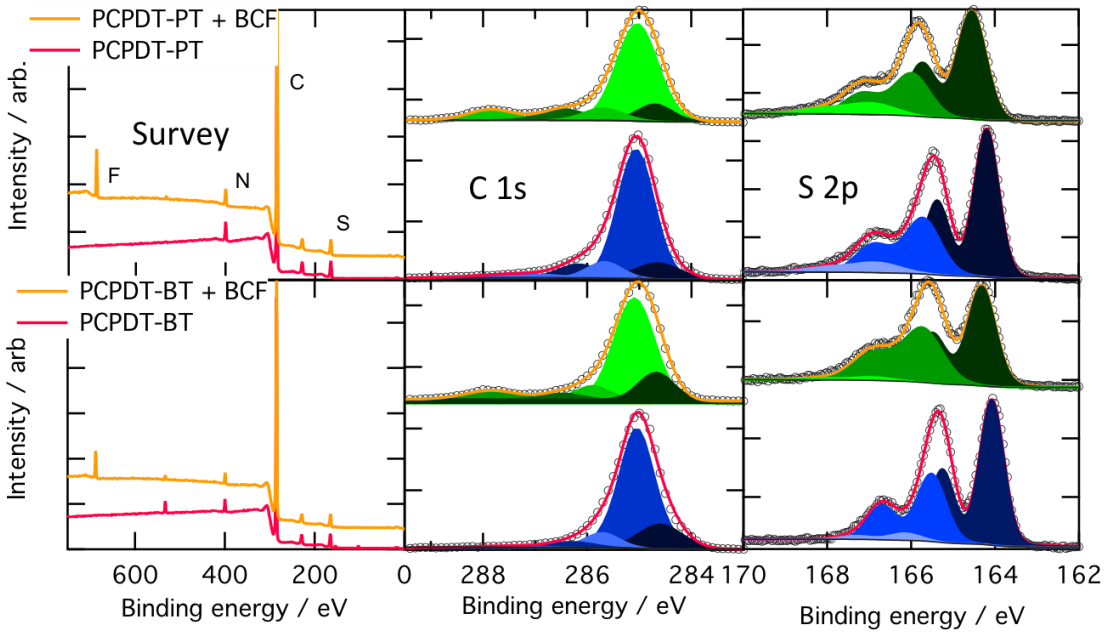

Figure 3-6. Survey and high-resolution C 1s and S 2p XPS spectra of polymers with and w/ out BCF

Futhermore, an additional high-resolution S 2p XPS spectrum of just the CPDT monomer with BCF further confirms no binding of BCF to the sulfur atoms in the polymers (Figure 3-7).

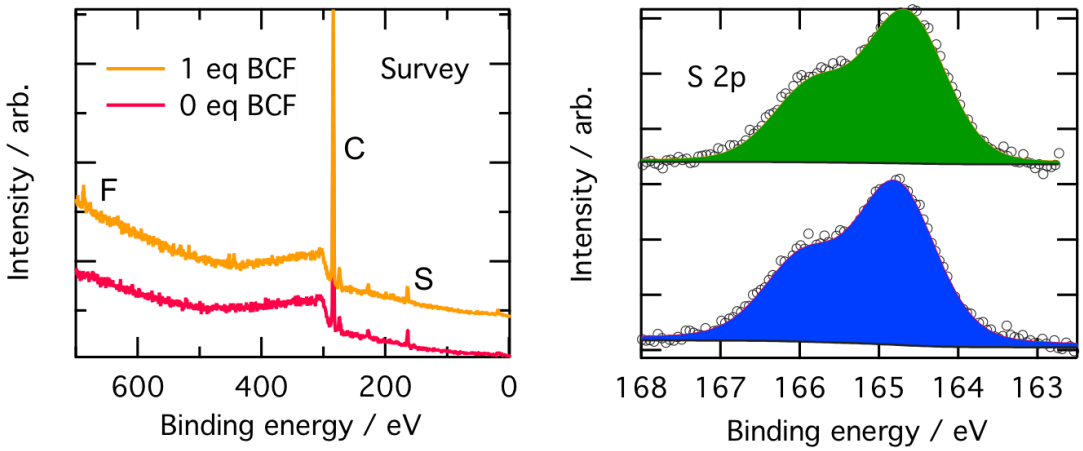

Figure 3-7. Survey and high-resolution S 2p XPS spectra of CPDT monomer with and w/out BCF

In summary, there is evidence for BCF binding to the pyridyl nitrogen on the PT group of PCPDT-PT that leads to the reduction in the bandgap as previously reported in literature.[144–146]

3. EPR and UPS

Despite experimental evidence for BCF binding to PCPDT-PT, formation of the BCF-polymer complex does not correlate to electrical doping of the polymers with BCF, where electrical doping herein is defined to be the formation of free charge carriers in the polymer upon addition of the dopant BCF. Indeed, both PCPDT-BT and PCPDT-PT are electrically doped by BCF as seen from EPR and UPS measurements detailed below, even though BCF does not bind to PCPDT-BT. Film EPR measurements of the polymers with BCF show a clear signal corresponding to an unpaired electron on the polymer backbone for both PCPDT-BT and PCPDT-PT (Figure 3-8). Solution EPR of the polymers with BCF give the same result as seen in film EPR. Separate samples of the polymers with F_4TCNQ added were also examined by EPR and the same results were seen – that is, PCPDT-BT and PCPDT-PT are also doped

by F_4TCNQ (Figure 3-9). In theory, an EPR signal from the BCF radical anion should also be seen given the formation of a cationic radical species on the polymer backbone. However, previous EPR spectra of BCF radial anions have shown they are unstable at room temperature, and only at -50 ^oC can the EPR signal from a radial anion of BCF be seen.[147]

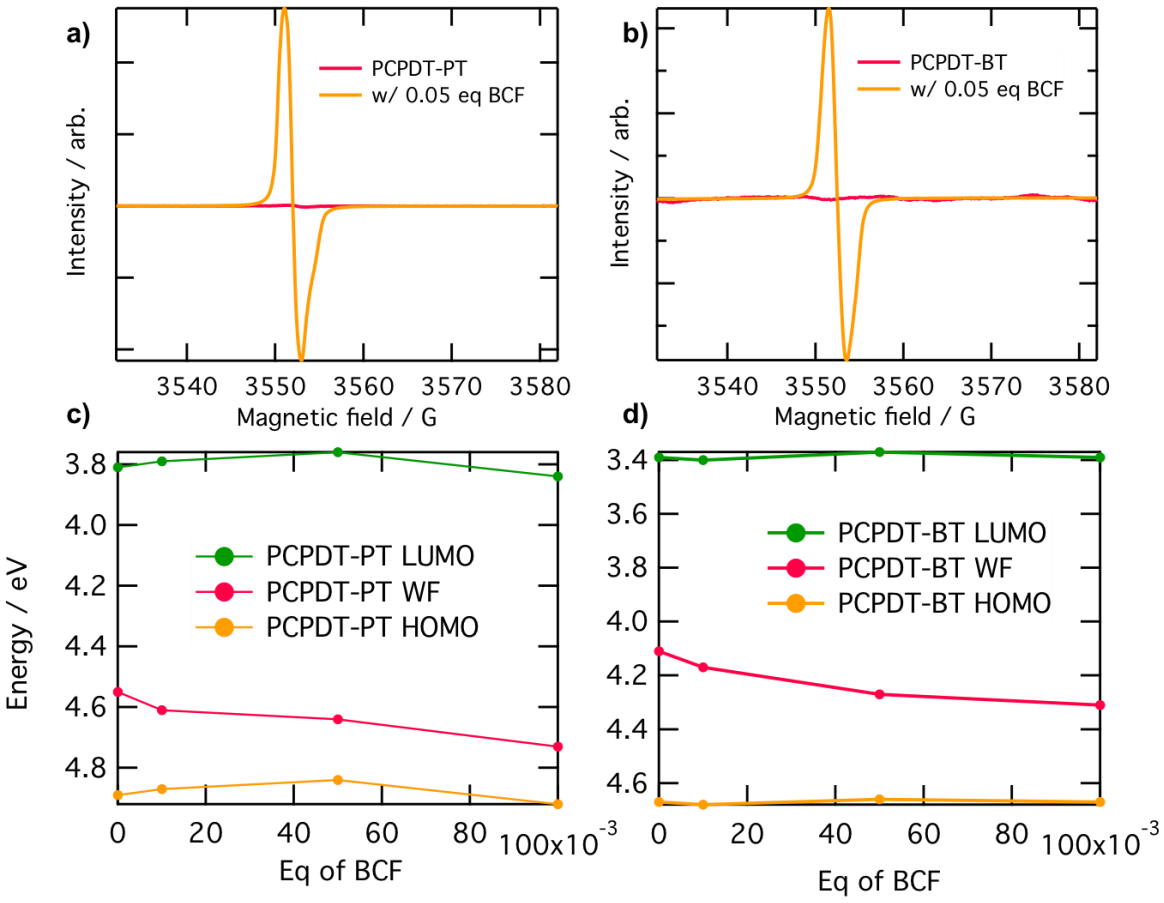

Figure 3-8. EPR spectra (top) and energy levels (bottom) of polymers with BCF.

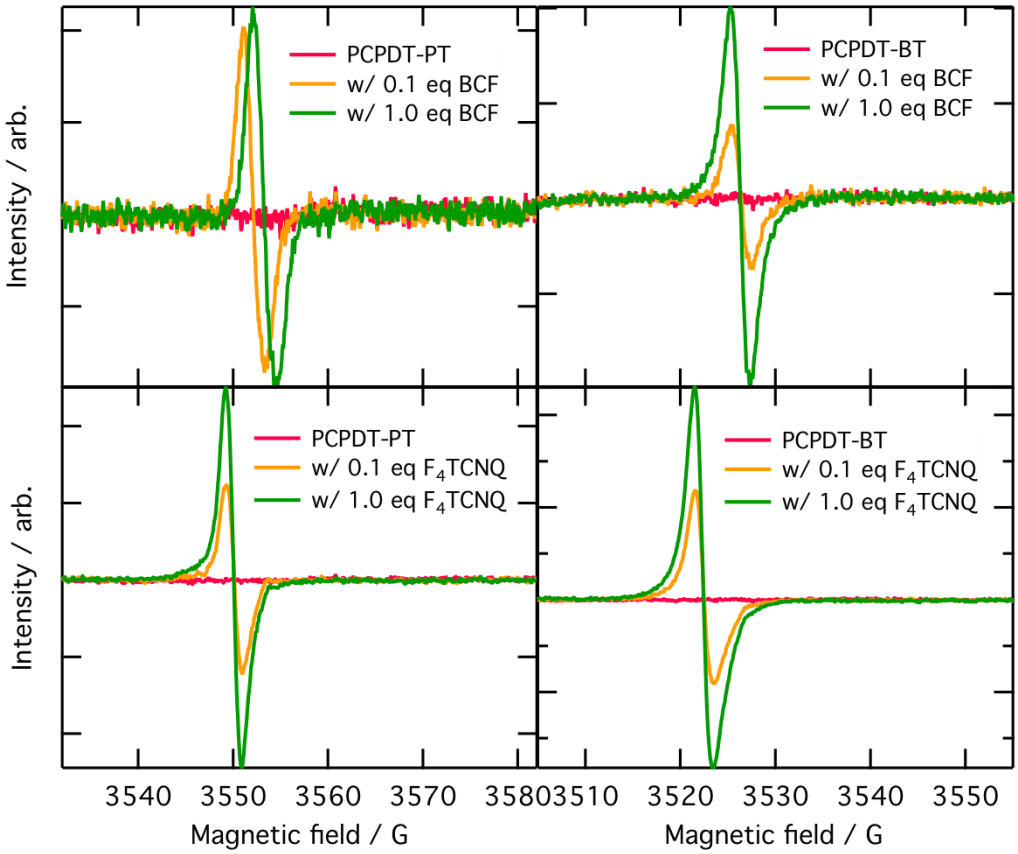

Figure 3-9. EPR spectra of polymers with BCF and F_4TCNQ

Ultraviolet photoelectron spectroscopy measurements of the two polymers with different amounts of BCF shows the expected shift of the Fermi level towards the HOMO that comes from the creation of more holes, which populate the HOMO states of the polymers (Figure 3-8).[148] In other words, the addition of BCF p-dopes the polymer, causing a deepening of the work function of the polymer. The LUMO levels were estimated from measurements of the polymer's optical bandgap in the pristine state. The full UPS spectra are shown in Figure 3-10, from which the energy levels in Figure 3-8 were derived. From both the EPR and UPS measurements, we can conclude that with the addition of BCF, holes are being formed in PCPDT-PT and PCPDT-BT. Here we should also make a note that while the terminology

HOMO and LUMO are often used among the organic semiconductor community to refer to states seen by UPS and inverse photoelectron spectroscopy (IPES), they are not technically the most correct terms to be using as we are working with polymers, not discrete molecules, and as such their frontier energy levels begin to blend in a continuum of energy states as opposed to discrete energy levels. However, due to the ubiquitousness of the terms HOMO and LUMO within the community, they will be used in this thesis.

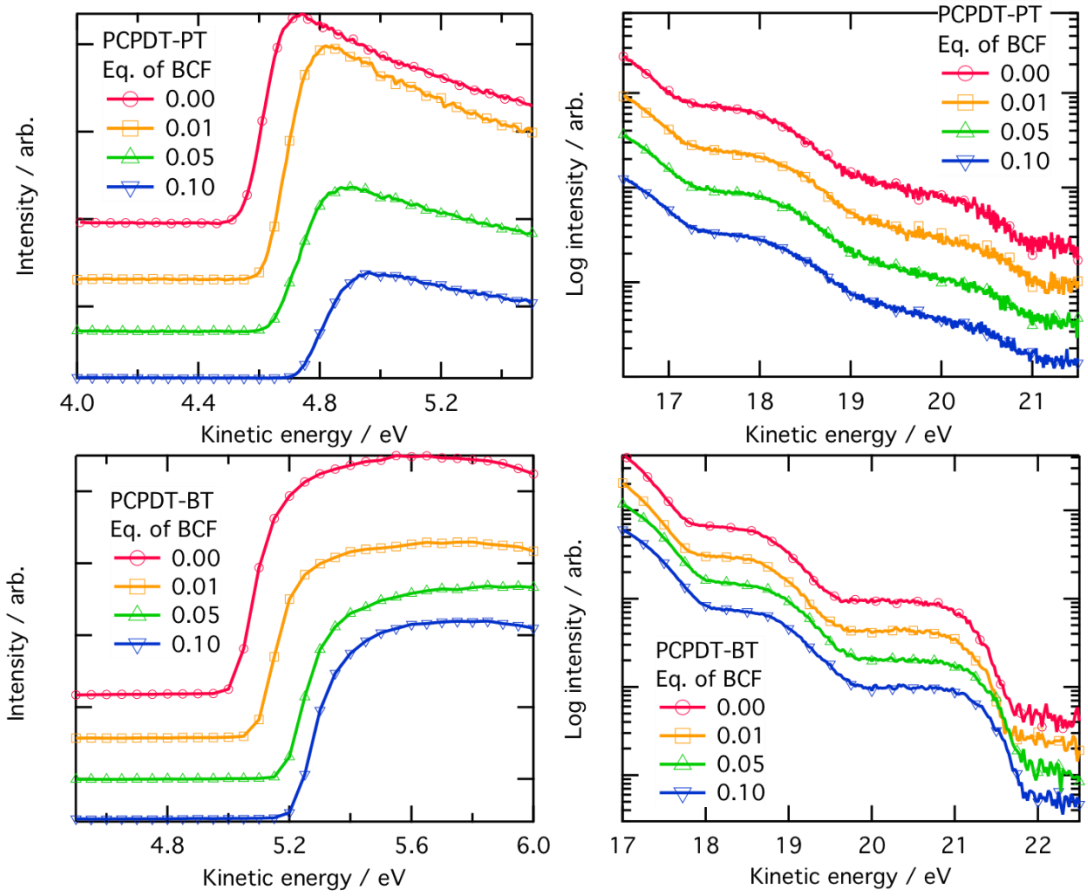

Figure 3-10. UPS spectra of polymers with BCF

Because of PCPDT-PT's unique characteristics in that the addition of the Lewis acid BCF not only changes its bandgap but also dopes the polymer, the choice was made to study only the doping efficiency of PCPDT-BT with respect to the different Lewis acid dopants. The

competing nature of binding and doping in the case of PCPDT-PT will make it challenging to deconvolute the processes enroute to answering the question does the strength of the Lewis acid strength have any bearing on doping efficiency.

C. Impedance Spectroscopy (IS)

Before delving into the doping efficiency of PCPDT-BT upon the addition of different Lewis acids, a short chemists' introduction into the device structure used as well as the instrumental technique is warranted as it falls more on the side of semiconductor physics than chemistry. Impedance spectroscopy involves the analogy that just like how normal direct current (DC) electrical measurements are subject to resistance, which is the impediment of electron motion, so are alternating current (AC) electrical measurements. However, when talking about AC measurements, the term impedance is used instead of resistance, in recognition that the two processes are not the same. Ohm's law, which governs DC measurements, assumes a single, ideal resistor with a resistance value that is independent of frequency. In addition, Ohm's law also assumes that for AC measurements, the current and voltage signals are in phase with each other. Impedance on the other hand takes into account these different simplifications that Ohm's law does not, allowing for more complex electrical analysis.

When measuring impedance, a small, 10 mV AC voltage signal is applied, and the current response is measured. In a linear system, where linear systems are defined somewhat simplistically in this thesis as a system where a two-fold increase in voltage corresponds to a two-fold increase in current, the resulting current signal should have the same frequency and amplitude as the voltage signal, except shifted in phase. Most electrochemical systems however are not linear, resulting in some complex impedance behavior that is beyond the

scope of this thesis. However, for the electrochemical measurements that were performed to obtain the doping efficiency of the polymer, a small (< 20 mV AC amplitude) signal was applied to the system of interest, allowing us to obtain a pseudo-linear system where within the small voltage range that was probed, the current response is linear. In addition to using an impedance analyzer which allows us to apply DC and AC voltages while measuring the impedance response, the correct device architecture also needs to be employed.

To obtain the doping efficiency of our systems, a device with the structure Si/SiO_2/BCB/polymer/Au was fabricated, often referred to as a metal-insulator-semiconductor device structure (MIS). For polymers with an intermediate charge carrier concentration between (10^{15} cm^{-3} to 10^{18} cm^{-3}), the charge carrier density, conductivity, mobility, and doping efficiency can be probed using a MIS device structure. Materials with very high charge carrier concentrations cannot be probed using a MIS structure, which will be expanded on in detail below. The SiO_2 capacitor layer was passivated with BCB because the presence of water on the SiO_2 layer has been shown to interfere with electrical measurements due to the presence of traps.[149]

During the experiment to obtain the doping efficiency, a large DC bias is applied to the MIS structure, coupled with a small AC bias. Simplistically speaking, the role of the DC bias is to pull charges to the insulator-semiconductor interface which then modulates the measured capacitance of the device, whereas the AC bias is used to probe the impedance of the device. In order to accurately measure the impedance of the device, all the charges need to be swept towards the interface to form the depletion layer, which is the layer at which the number of majority free charge carriers, in this case holes, eventually decreases to zero. When the free charge carrier concentration is very large, there is no physical point in the device at which the

number of free charge carriers goes to zero, thereby preventing accurate measurement of the capacitance of the overall device. The reason for this is the depletion layer is larger than the thickness of the device, meaning there is no point at which all of the charges can be accounted for by measuring the change in capacitance of the device. Figure 3-11 below gives a schematic representation of an MIS device operating in the accumulation and depletion regimes.

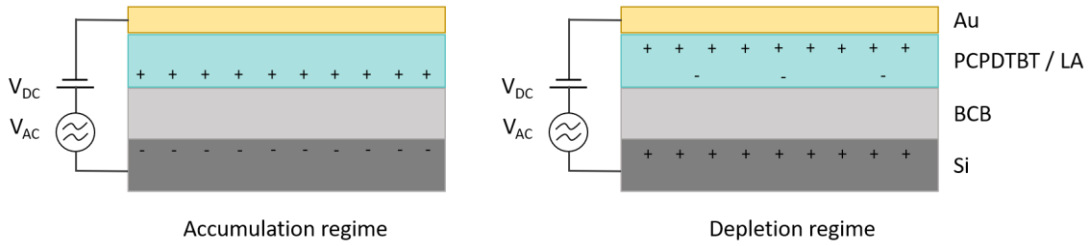

Figure 3-11. MIS device schematic operating in accumulation and depletion regimes.

In the accumulation regime, a negative bias is applied to the silicon electrode, thus attracting the majority charge carrier (holes) to the interface of the semiconductor and the insulator. In the depletion regime, the opposite occurs, leaving behind a regime where there are very few mobile charges. The negative charges that are present come from ionized dopant molecules, which are not only significantly less mobile compared to the holes, but also much lower in concentration. The depletion regime acts as a capacitor, thus decreasing the overall capacitance of the device.

The resulting data is plotted, with capacitance on the y-axis, the frequency at which the measurement was obtained on the x-axis, and each DC voltage as a separate line on the plot, to give Figure 3-12, which is an example of what the data looks like from a measurement of

the polymer PCPDT-BT with the Lewis acid BCF. The lines go from negative DC bias at the top of the plot, to positive DC bias towards the bottom of the plot.

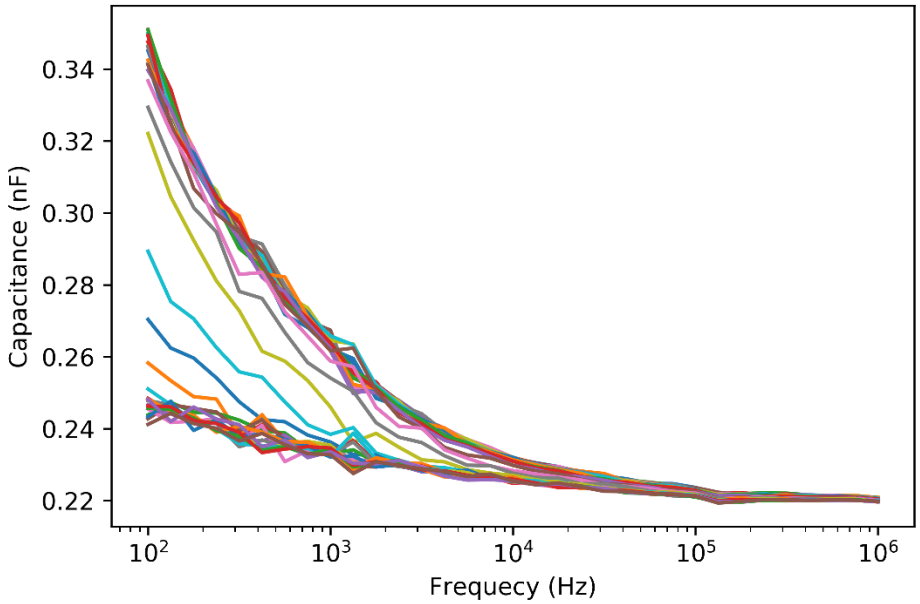

Figure 3-12. Representative capacitance-frequency plot from MIS measurements of PCPDT-BT and BCF

Here I should specify that the MIS measurement is really measuring uncompensated acceptor centers, however the chemistry side of the organic semiconductor community often refers to them as free charge carriers, which is the language that will be used throughout the thesis. Doping of PCPDT-BT results in an increase in free charge carriers, specifically holes, thereby leading to changes in the capacitance upon application of a DC voltage which can be measured and plotted in the aforementioned plot. In Figure 3-12, we can see that as the frequency is increased, the capacitance across all DC voltages is the same, due to the free charge carriers no longer being able to respond quickly enough to the applied AC voltage to form the accumulation and depletion regimes.

The frequency at which the capacitance of the MIS device is equal to the capacitance of the insulator layer by itself is when the capacitance values at each of the measured DC voltages is obtained and plotted into what is known as a capacitance-voltage plot, or C-V plot. A representative plot is shown in Figure 3-13. From this figure, we can also distinguish the accumulation and depletion regimes, where at negative gate voltages, the device is operating in the accumulation regime thus giving a higher measured capacitance. At positive gate voltages, the device is operating in the depletion regime and the capacitance drops.

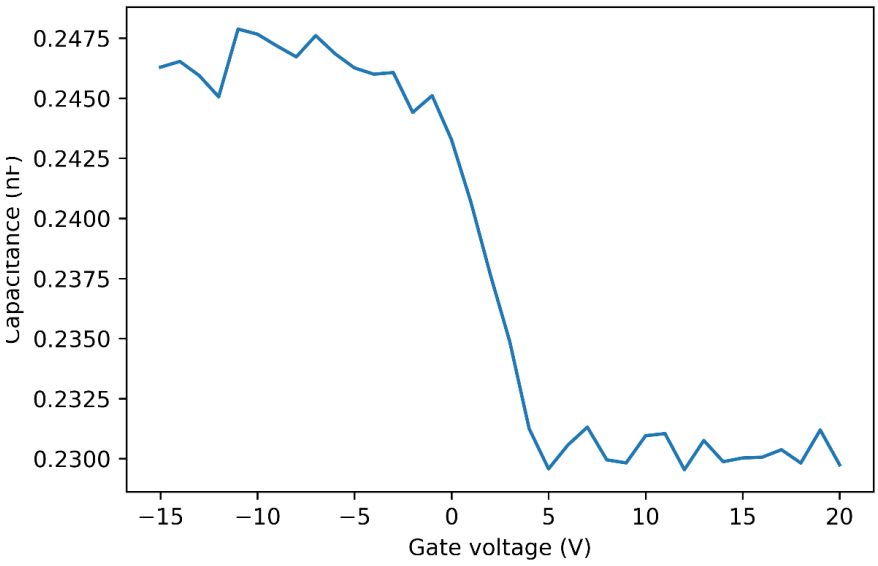

Figure 3-13. Representative capacitance-voltage plot from MIS measurements of PCPDT-BT and BCF

A Mott-Schottky plot can then be generated by using Equation (3), where C is the capacitance, ε is the dielectric constant of the polymer, estimated to be 2.5, ε_0 is the permittivity of free space, A is the area of the device under test, e is the elementary charge, N_a is the density of dopants, V is the applied potential, V_{fb} is the flatband potential which is also known as the built-in potential, k_B is Boltzmann's constant, and T is the absolute temperature.

$$\frac{1}{C^2} = \frac{2}{\varepsilon\varepsilon_0 A^2 e N_a}\left(V - V_{fb} - \frac{k_B T}{e}\right) \quad (3)$$

Rearranging (3) allows us to then plot the square of the area over the square of the capacitance $(A/C)^2$ versus the voltage. The slope of that plot, an example of which is shown in Figure 3-14, allowed calculation of N_a, the concentration of uncompensated acceptor centers.

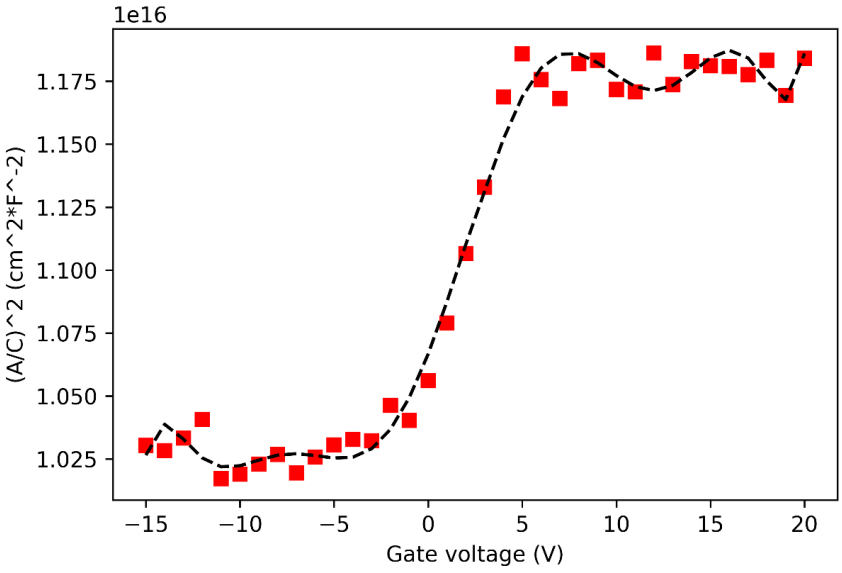

Figure 3-14. Representative Mott-Schottky plot from MIS measurements of PCPDT-BT and BCF

Taking the derivative of the Mott-Schottky plot to find the maximum slope gives us N_a. The doping efficiency can then be calculated by taking the concentration of uncompensated acceptor centers (N_a), and dividing that by the molecular equivalents of dopant added multiplied by the concentration of monomer units (Equation **(4)**). The number of unintended free charge carriers from unintentional doping due to impurities also needs to be subtracted out from the calculated number of uncompensated acceptor centers (N_a) to give the actual doping efficiency.

$$DE = \frac{N_a - N_d}{ME * N_m} \quad (4)$$

The concentration of monomer units in the film was determined by collaborators using X-ray reflectivity, the parameters of which are detailed in the experimental section of this chapter.

D. Doping Efficiency Trends and Discussion

Recall that traditional theories of Lewis acid strength place BBr_3 on the upper end of Lewis acid strengths, and BF_3 on the lower end. The Gutmann-Beckett method for determining Lewis acidities confirms the traditional theories of Lewis acid strengths, and in addition places BCF below BF_3 in terms of Lewis acidity. The Guttmann-Beckett method is based on the change in ^{31}P NMR chemical shift after complexation of the Lewis acid with Et_3PO.[143,150,151] The greater the shift, the stronger the Lewis acid.

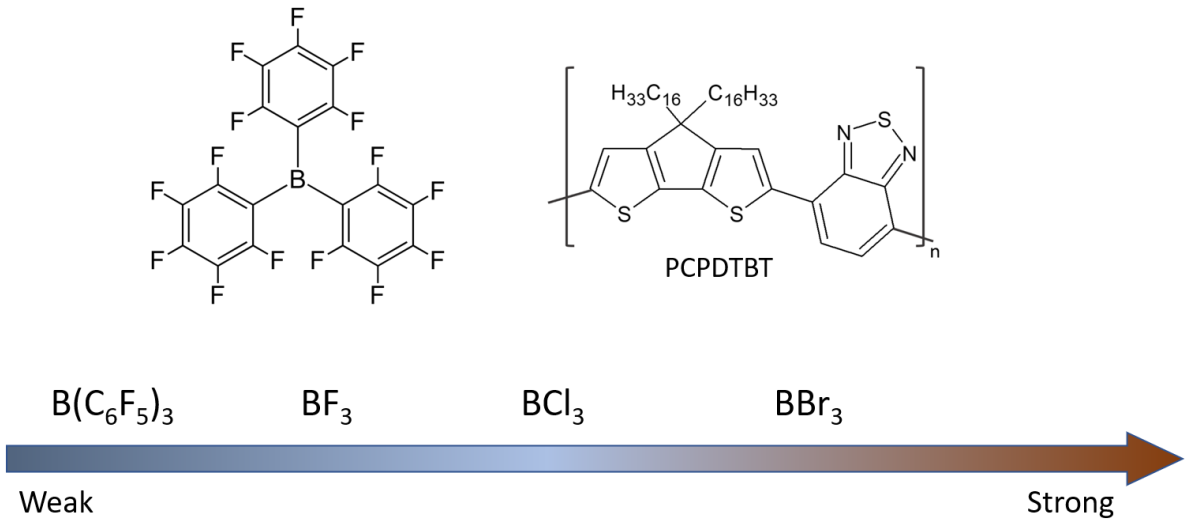

Figure 3-15. Chemical structures of BCF and PCPDT-BT and Lewis acid strengths

However, Lewis acid strengths as seen in Figure 3-15 do not correlate to an increase in doping efficiency. In fact, there is no discernable correlation between the doping efficiency

and the strength of the Lewis acid. The resulting doping efficiencies obtained from the MIS measurement described above are plotted in Figure 3-16.

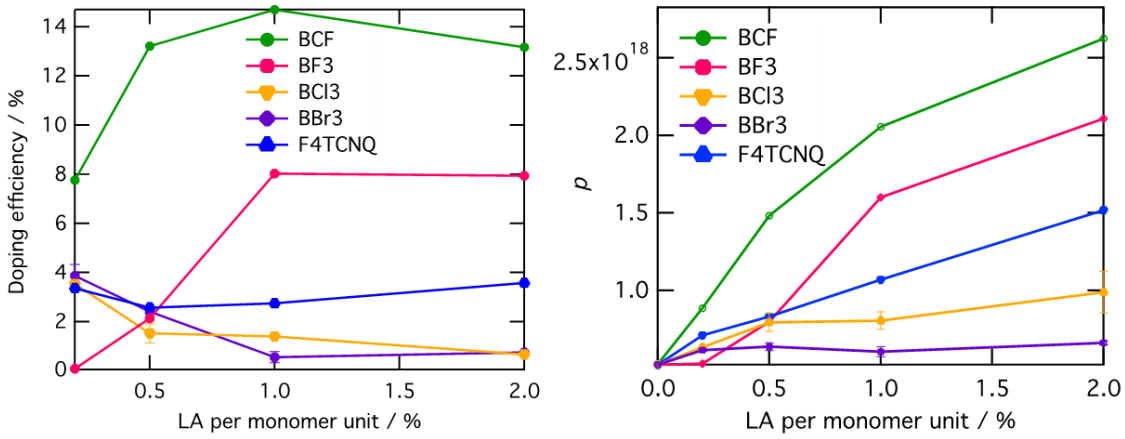

Figure 3-16. Doping efficiency and number of holes of PCPDT--BT for different Lewis acids

Possible explanations for this situation entail the doping mechanism of the Lewis acid, as outlined in our group's paper.[72] Because the doping mechanism entails the formation of a Lewis acid adduct with water, Lewis acids that can form stable adducts with water in adduct concentrations high enough for doping of the polymer are preferred. Numerous reports detail how BBr_3 and BCl_3 react with H_2O to form $B(OH)_3$ and their corresponding acids, as outlined in equations (5) and (6) below.

$$BBr_3 + 3\ H_2O \rightarrow B(OH)_3 + 3\ HBr \quad (5)$$

$$BCl_3 + 3\ H_2O \rightarrow B(OH)_3 + 3\ HCl \quad (6)$$

These reactions suggest that some Lewis acid water adducts are not stable, and therefore are not useful for doping of PCPDT-BT. This has led to questions regarding why HCl and HBr cannot act as acids and protonate the PCPDT-BT backbone to begin the doping process. While beyond the scope of this thesis, I would like to propose that in addition to the instability

of BBr_3 and BCl_3 to H_2O, the resulting acid products, hydrobromic and hydrochloric acid respectively, are only sparingly soluble in chloroform and chlorobenzene, the solvents used in this study. In addition, HBr and HCl are repelled by the non-polar side chains of PCPDT-BT, thus preventing HBr and HCl from interacting with and protonating the polymer species. This stands in contrast to BCF, whose water adduct is chemically stable. In contrast, the pentafluorophenyl moieties on BCF help BCF retain its solubility in organic solvents, thus helping it interact with PCPDT-BT and dope the polymer. Ironically, it is the strength of the Lewis acids BCl_3 and BBr_3 that promote their rapid reaction with water, thus making them poor dopants for PCPDT-BT.

Another possible reason for the lower doping efficiency of putatively stronger Lewis acids BCl_3 and BBr_3 is their Lewis acidity and small size could make binding to Lewis basic sites on PCPDT-BT more favorable than the formation of water adducts. Our work has shown that Lewis acid binding to Lewis basic sites on the polymer is in direct competition with Lewis acid doping of the polymer due to the doping mechanism. Therefore, if more Lewis acids have directly formed dative bonds with Lewis basic sites on the polymer, they are no longer available for doping.

The doping efficiency over time was also examined in this study. Fresh MIS devices with different percentages of various boron-based Lewis acids were fabricated and measured. Between measurements, the devices were kept in a nitrogen filled glovebox. The results in Figure 3-17 show that PCPDT-BT MIS devices doped with BCl_3 or BBr_3 are less stable—their measured doping efficiency drops by 50 % over the course of 12 days, whereas 2.0 % monomer equivalents of BCF remains stable and 0.2 % monomer equivalents of BCF increases over time. Possible reasons for these findings that should be probed are as follows.

Since all steps in the doping mechanism as shown in Figure 3-2 are in equilibrium with each other, it is likely that BCl_3 and BBr_3 vacillated between their water and non-water adducts, with the former being the dopant for PCPDT-BT. As just the native Lewis acid, BCl_3 and BBr_3 degrade to $B(OH)_3$ over time in the presence of water, rendering them incapable of doping PCPDT-BT. Even in the controlled environment of a glovebox, there are trace amounts of water that are available for reaction with the Lewis acids, turning BCl_3 and BBr_3 into $B(OH)_3$. On the other hand, BCF is stable and does not readily degrade to $B(OH)_3$ in the presence of water.

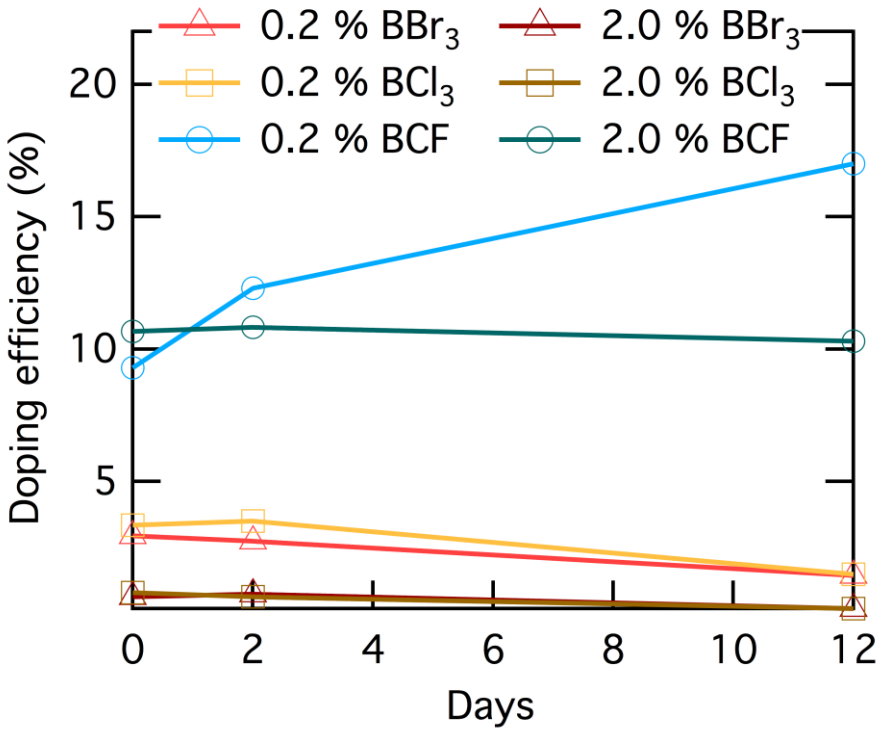

Figure 3-17. PCPDT-BT doping efficiency of different boron-based Lewis acids over time

E. Experimental Section

1. Materials

BCF was purchased from Tokyo Chemical Industry Co., Ltd., and used as received. BF_3 (diethylether), BCl_3 (1 M in dichloromethane), BBr_3 (1 M in dichloromethane), and the solvents used were purchased from Sigma-Aldrich and used as received. PCPDT-BT was purchased from 1-material and used as received. PCPDT-PT was synthesized in-house according to published literature.[152] All materials were stored in a dry, inert atmosphere (N_2) glovebox.

2. UV-vis-nIR absorption spectroscopy

All UV-vis-NIR spectra were obtained using a Perkin-Elmer Lambda 750 UV-vis-NIR spectrometer using a tungsten lamp for the visible to near-IR region and a deuterium lamp for the UV region. Solution UV-vis-nIR spectra were obtained using a polymer concentration of 0.025 mg/mL for PCPDT-PT and 0.05 mg/mL for PCPDT-BT. Film UV-vis-nIR spectra were obtained by casting a thin film of the polymer with dopant solution on a clean indium tin oxide/glass substrate. A 100% transmission blank was obtained using a clean indium tin oxide/glass substrate for all film spectra.

3. XPS

Measurements were obtained using a Kratos Axis Ultra DLD XPS under vacuum (10^{-9} Torr) using monochromated X-rays produced using an aluminium source running at a potential of 14 kV and a current of 14 mA. A pass energy of 20 was used for all high-resolution element sweeps, and 160 for survey sweeps. Sample preparation was identical to that

described for UPS measurements. Peak fitting was performed using WINSPEC, and atomic sensitivity factors for each element were taken into account during peak integrations.

4. UPS

Measurements were obtained using a Kratos Axis Ultra DLD XPS system under vacuum (10^{-8} Torr) using He I line with 21.21-eV photons (Supplementary Figs. 12 and 13). Samples were prepared on freshly cleaned conductive indium tin oxide/glass substrates at a thickness of approximately 10 nm. The films were mounted onto a sample bar using double-sided adhesive tape, electrically ground to the sample bar using nickel impregnated tape and biased at −9 V.

5. EPR

EPR measurements were obtained on a Brucker continuous wave (CW) X-band EPR, running at a frequency of 9.79 GHz. Solution EPR samples were prepared by dipping 0.7 MM inner diameter capillaries into doped solution, then sealing both ends with critoseal. Film EPR samples were prepared by dipping 0.7 MM inner diameter capillaries into doped solution, then allowing the solution to evaporate leaving behind a film coating the inner walls of the capillary tube. An empty capillary tube was also run to ensure measured EPR signal was from the sample.

6. Impedance Spectroscopy (IS)

Measurements were obtained from a device structure of n^{++}-Si/SiO_2 (200 nm)/benzocyclobutene (BCB, 30 nm)/active layer/Au to create the MIS architecture. Benzocyclobutene was spun-cast on top of the SiO_2 dielectric layer from a 1 mg/ml solution at 4,000 r.p.m. and then annealed at 250 °C for 1 hr. The active layer was spin-coated at 1,200

r.p.m. on top of BCB after cooling, followed by thermal evaporation of the gold contact. The n^{++}-Si was used as the working electrode. The stack of 200-nm SiO_2 and 20–30-nm BCB served as the insulator layer. Film thickness measurements were carried out using an Innova AFM. MIS devices were analyzed using a Solartron 1260 impedance analyzer. The impedance spectra were measured over a wide frequency range (10 Hz – 3 MHz) with a small alternating current amplitude signal of 20 mV and various direct current biases ranging from −15 to 20 V.

7. X-ray reflectivity (XRR)

Solution of PCPDT-BT was spuncast on a clean glass substrate to obtain a thin film of approximately 25 nm. The density of the thin film was then determined by X-ray reflectivity measurements using a Rigaku Smartlab High-Resolution Diffractometer and accompanying reflectivity fitting software (GXRR3) in order to determine the concentration of monomer units in the thin film for calculation of the doping efficiency.

Chapter 4 − Using CPE-K to Visualize Electron Transfer from Bacteria

A. Introduction to Microbial Fuel Cells (MFCs)

Microbial fuel cells (MFCs), currently a niche renewable energy source, suffer from high overpotential losses, of which approximately half is due to losses that occur during electron transfer from the bacteria to the electrode.[153] By understanding the efficiency losses during electron transfer from bacteria to electrode, we can better understand how to direct efforts to reduce the overpotential loss.

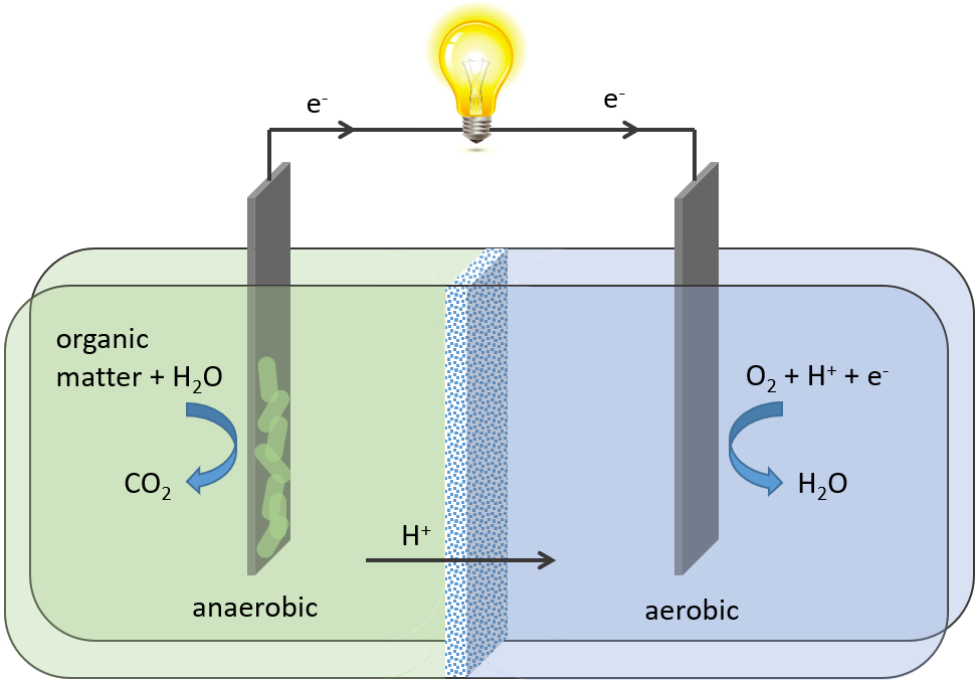

Figure 4-1. Diagram of microbial fuel cells (MFCs)

So far, there has not yet been consensus on the electron transfer mechanism. Some claim electron transport occurs through electrically conductive pili[154,155] while others argue electron transport occurs through redox mediated electron transfer in which electrons are required to hop from one electron site to another.[156–160] Previous, albeit limited work using scanning probe microscopy (SPM) to look at *G. sulfurreducens* has focused solely on examining the

conductivity of their pili.[154,155,161–163] While this work will comment upon possible electron transfer mechanisms based on the images obtained, the focus is on using this technique to better understand losses to electron transfer efficiency from the bacterium *G. sulfurreducens* to the electrode. In this work, we use a hole-transporting conjugated polyelectrolyte (CPE) and conductive atomic force microscopy (cAFM) to probe the transfer of electrons from single cells of the bacteria *G. sulfurreducens* to the CPE surface. A recent publication describes the use of a new experimental platform for monitoring single cell respiration rates at electrode interfaces for the bacteria *Shewanella oneidensis* MR-1.[164] In this work however, we use commercially available instrumentation to demonstrate the ability to *quantitatively* examine electron transfer from *G. sulfurreducens* to the CPE surface on the nanoscale and use the information to better understand the reason for large overpotential losses in MFCs.

B. Experimental Requirements

In order to image bacteria donating their electrons, a few things are required: first, a material to which bacteria can donate electrons to; second, a material that is insoluble in water and the medium in which the bacteria are in upon being deposited onto the surface; and third, instrumentation capable of obtaining current and morphology images simultaneously with nanoscale resolution. Using a hole-transporting organic semiconductor allows for visualization of the bacteria transferring its electrons to the organic semiconductor *via* the scheme shown in Figure 4-2. For this experiment, we used PCPDTBT-SO_3K (CPE-K), previously synthesized and reported by Gui Bazan.[128] Because holes are present in doped CPE-K, electrons from the bacteria can recombine with those holes, quenching them and subsequently reducing the conductivity of CPE-K *via* a reduction in free charge carrier density.

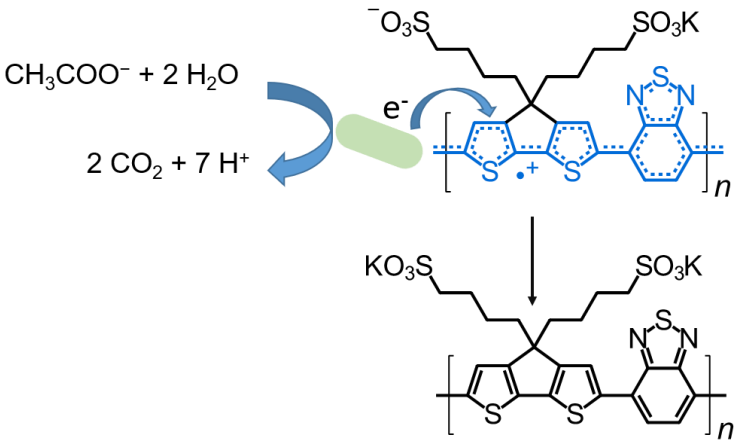

Figure 4-2. Schematic for de-doping of CPE-K by bacteria

Previous work has shown *Shewanella oneidensis* MR-1 can also anaerobically respire on CPE-K where the CPE acts as the electron acceptor in place of fumarate.[165] In addition, CPE-K, which contains anionic pendant groups, is not toxic to *G. sulfurreducens*, a gram-negative bacteria. While there are studies that have shown CPE toxicity to the gram-negative bacteria *Escherichia coli* (*E. coli*), those have been in cases for CPEs with a pendant cation, whereby the CPE coats the surface of the bacteria and causes cell death.[166]

In order to prepare CPE-K for an aqueous solution of *G. sulfurreducens*, CPE-K, which is soluble in water, had to be rendered insoluble when exposed to water. For this, inspiration was drawn from literature, which showed that upon annealing of a MEH-PPV film for 1 hour at 220^{o}C, the solubility of the MEH-PPV film was greatly reduced.[167,168] After spin-coating a solution of CPE-K onto a clean indium tin oxide (ITO)/glass substrate, the CPE-K film was annealed at 300^{o}C for 30 minutes under an N_2 atmosphere, at which point it was insoluble in water as well as *G. sulfurreducens'* growth media. However, the annealing process also de-dopes CPE-K.[169] As mentioned previously, CPE-K needs to be doped for this experiment – therefore the CPE-K film was then submerged in ultrapure water that was measured to have a pH of 5 and resistivity of 18.2 MΩ*cm, at which point the film becomes doped again as seen

and monitored by UV-vis-nIR. The peaks at 1100 nm and 1800 nm are indicative of a polaron in CPE-K, which in of itself is good indication that CPE-K is doped (Figure 4-3).[92]

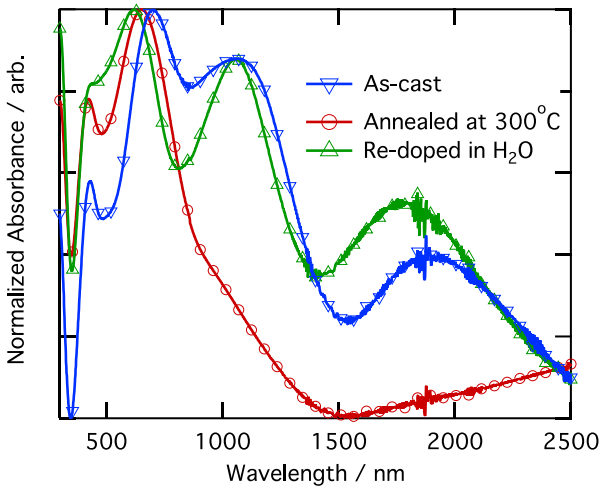

Figure 4-3. UV-vis-nIR film absorption spectra of CPE-K before and after thermally reversible de-doping

In order to image the bacteria on top of CPE-K, cAFM is employed due to its ability to simultaneously obtain both a current and morphology image of the organic semiconductor surface and the bacterium drop cast on top of it at nanoscale resolution (Figure 4-4). The cAFM tips employed had a work-function that matched the HOMO of CPE-K in order to provide for efficient hole transfer between the cAFM tips, CPE-K, and ITO. Before drop casting the bacteria on top of CPE-K, cAFM images of the annealed and unannealed CPE-K films were obtained, which indicate no change in the morphology of the CPE-K surface even though current levels in the annealed CPE-K film dropped to noise level.[169] After submerging the CPE-K film in water to re-dope the film, the current obtained *via* cAFM returns to levels seen in the CPE-K film before annealing, and the CPE-K film remains insoluble in water and other aqueous solutions.

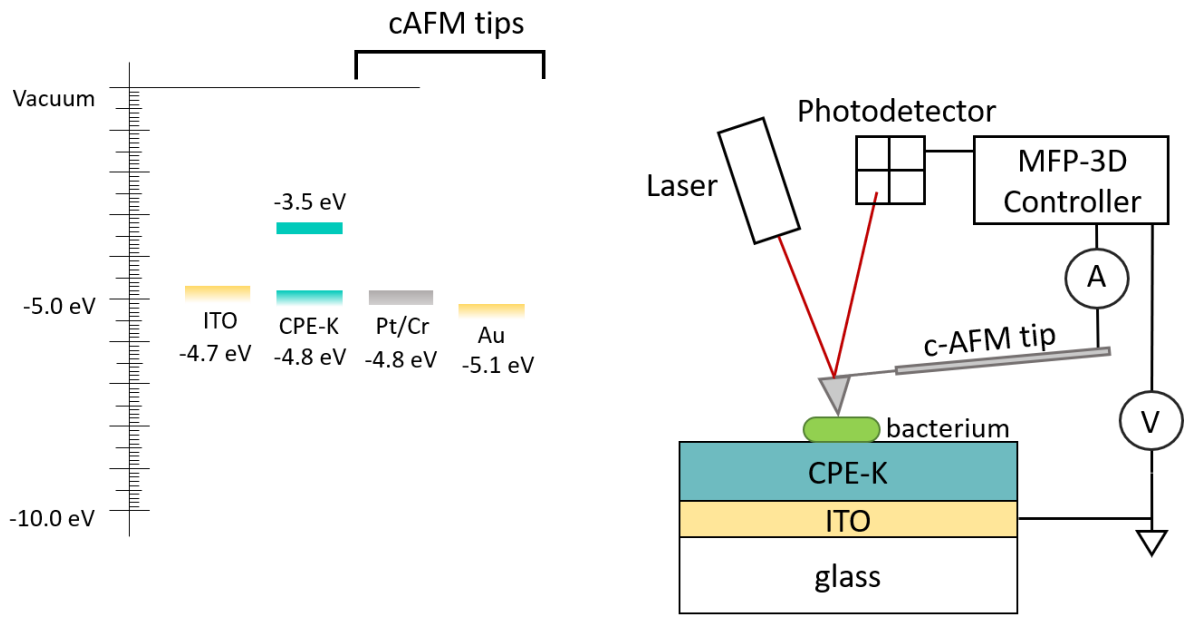

Figure 4-4. Figure of cAFM setup used in this experiment

C. Sample Preparation and Imaging

A solution of *G. sulfurreducens* grown in an electron-acceptor deficient environment was then drop-cast on top of the film (sample preparation along with culture and solution details in experimental section). *G. sulfurreducens* grown in an electron-acceptor deficient environment are known to store their electrons in the haem groups of their exocytoplasmic cytochromes.[170–172] While the *G. sulfurreducens* bacteria are still alive in the droplet cast on top of the CPE film, they can donate their stored electrons to the CPE, using the CPE as an electron acceptor as shown in Figure 4-2. After washing the film with anaerobic water of pH ~ 7 to remove residual salts, the film was allowed to dry, and then imaged with cAFM (Figure 4-5). A schematic of the sample preparation process is provided in the appendix as Figure 7-1. Anaerobic water was used because *G. sulfurreducens* is an obligately anaerobic bacterium, and water of pH ~ 7 was used to prevent the re-doping of CPE-K following bacterium electron transfer to the CPE. The voltages applied were chosen to maximize the signal to noise ratio.

The reduction in current around the bacteria is due to electrons being donated to the CPE-K, thereby quenching the holes in CPE-K, which decreases the number of free charge carriers in that portion of the film and lowers the conductivity of the material and the measured current. As far as we are aware, this is the first report of such images being obtained with direct visual proof of electron transfer from an electrogenic bacterium to another material.

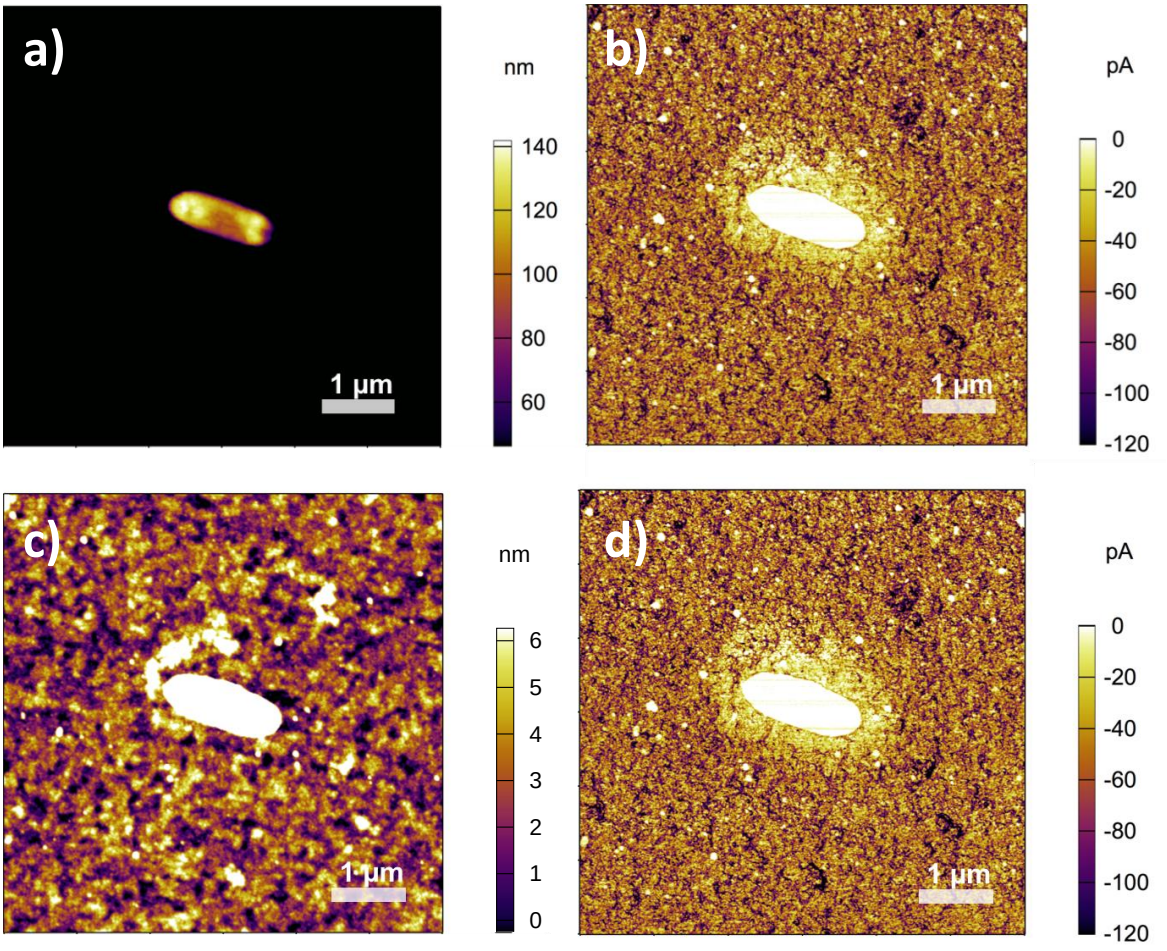

Figure 4-5. AFM (left) and cAFM (right) images of *G. sulfurreducens* on CPE-K

The redox gradient between the electrons stored in the cell membrane's cytochromes and the hole-transporting CPE-K provides a driving force for electron transfer from the bacterium to the CPE. The lighter areas indicate areas of lower current while the darker areas indicate areas of higher current, clearly showing a defined area around the bacteria due to *G.*

sulfurreducens de-doping CPE-K. Height images of the CPE-K surface show a retention of surface morphology after casting *G. sulfurreducens* on top, and bacteria dimensions of approximately 1 µm x 2 µm are consistent with SEM images obtained of *G. sulfurreducens*.[173] AFM images suggest the extracellular electron transfer mechanism for *G. sulfurreducens* in this system happens *via* either direct contact with outer membrane cytochromes or *via* redox-mediators such as flavins as no pili are observed in the AFM images under these growth conditions for *G. sulfurreducens*. In addition, there has been work showing that the pili of *G. sulfurreducens* conduct holes as opposed to electrons.[162] This work shows the dominant charge present in *G. sulfurreducens* are electrons, as the charges that are transferred to the CPE-K surface are de-doping the CPE-K.

D. Inefficiencies in Bacterial Electron Transfer

Additional images of *G. sulfurreducens* on CPE-K show areas around the bacterium where the CPE-K is not de-doped, suggesting the bacteria's haem groups are not always homogenously distributed across the bacteria's surface, or that they are not all always functioning correctly, which could be a source of overpotential loss in MFCs (Figure 4-6). In addition, some cAFM images reveal bacterium that have not transferred any electrons to the surface at all. The morphology image shows that particular bacterium lacks the height of neighboring bacteria that were able to transfer electrons to the surface, suggesting that particular bacterium died before being drop-cast onto the CPE-K film.[174,175] Dead bacteria within the solution or even a biofilm would also lead to increased overpotential losses in MFCs.

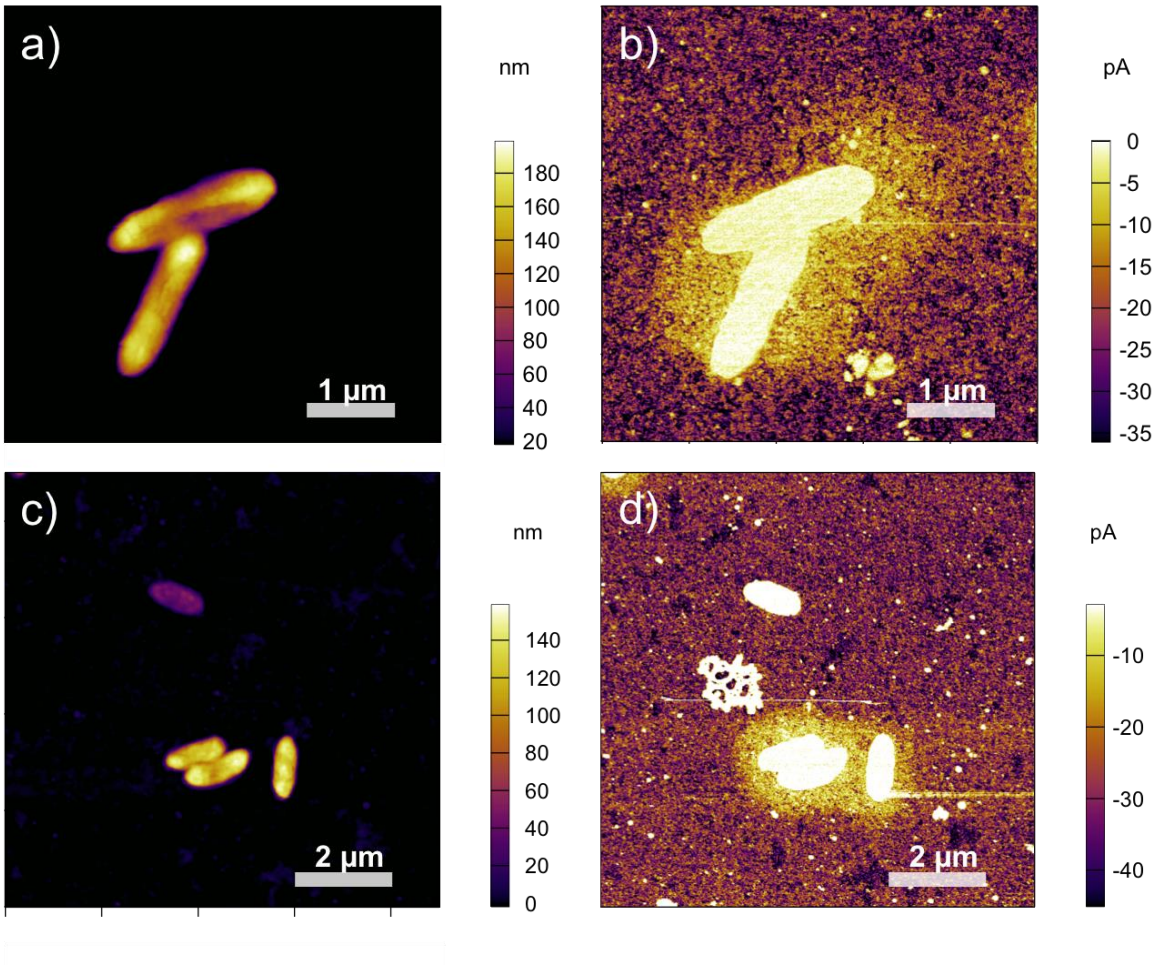

Figure 4-6. AFM (left) and cAFM (right) images of imperfect *G. sulfurreducens* on CPE-K

Control cAFM images of *E. coli* on top of CPE-K demonstrate that only electrogenic bacteria have the capability of de-dedoping the CPE-K film, and that the reduction in current seen around the *G. sulfurreducens* is due to electron transfer as opposed to leakage of organic material from the bacteria (Figure 4-7). In addition, filament-like structures are clearly seen coming out of the *E. coli* bacterium, confirming our instrument's capability to image them, which further confirms the non-existence of such structures in our images of *G. sulfurreducens*.

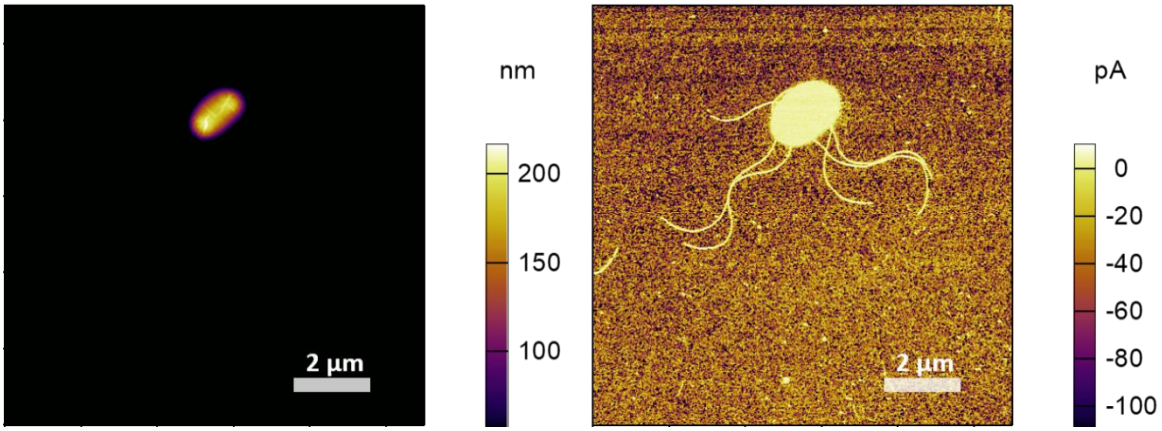

Figure 4-7. AFM (left) and cAFM (right) images of *E. coli* on CPE-K

High resolution atomic force microscopy images were also obtained showing no filament or pili growth in *G. sulfurreducens* (Figure 4-8). These results are in agreement with some literature suggesting the main electron transfer mechanism for *G. sulfurreducens* resides in their outer membrane cytochromes through either direct contact or *via* redox-mediated processes.[158,172]

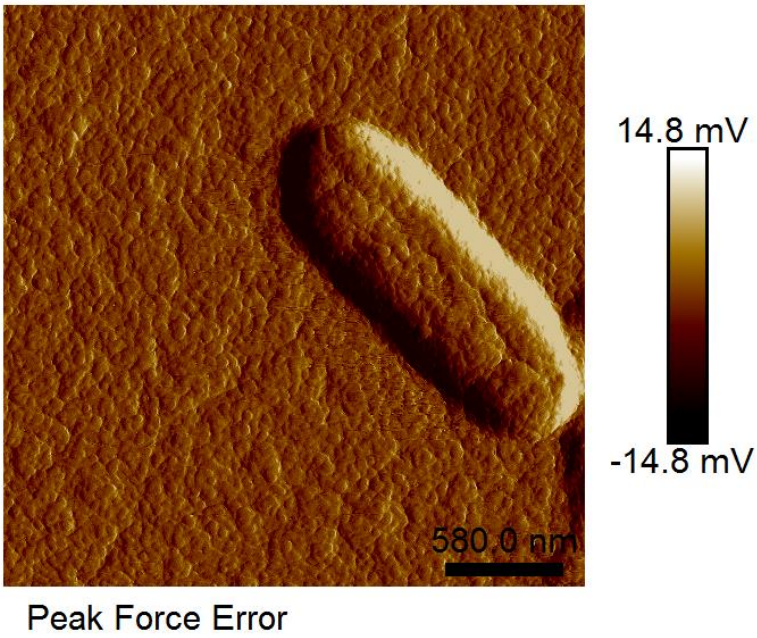

Figure 4-8. High resolution AFM image of *G. sulfurreducens* on CPE-K

E. Quantitative Electron Transfer Calculations

In order to quantitatively determine the number of electrons being transferred from *G. sulfurreducens* to the CPE-K film, bulk device current-voltage measurements were obtained of doped and undoped CPE-K as well as nanoscale current-voltage measurements of doped CPE-K. Due to the differences in electrode geometry between cAFM and bulk device measurements as well as the difference in electric field strength between nanoscale and bulk current-voltage measurements, care had to be taken in order to obtain the mobility of CPE-K on the nanoscale.[176] The mobility measured in a bulk device cannot be presumed equal to the mobility of CPE-K on the nanoscale. In addition, the mobility of doped CPE-K cannot be directly measured using cAFM because the high conductivity of the material precludes obtaining mobility of doped CPE-K *via* traditional methods such as space charge limited current – as such, the mobility of doped CPE-K on the nanoscale was estimated by employing the following ratio.

$$\frac{\mu_{cAFM\ undoped}}{\mu_{device\ undoped}} = \frac{\mu_{cAFM\ doped}}{\mu_{device\ doped}}$$

The "μ cAFM undoped" was obtained from SCLC fits to current-voltage curves obtained on the nanoscale using cAFM. To ensure an undoped CPE-K sample, the material was dissolved in water of pH = 7 which slightly de-dopes CPE-K by virtue of deprotonation of the polymer.[169] The solution was spuncast, and the resulting film was annealed at 300 ^{o}C to complete the de-doping process. The "μ device undoped" was obtained by SCLC fits to current-voltage curves from hole-only diodes with gold electrodes on the top and bottom. The CPE-K films for bulk device mobility measurements were prepared in the same manner as the films used to measure the mobility of undoped CPE-K by cAFM. In order to obtain "μ device doped", Hall effect measurements were performed on intrinsically doped CPE-K films. CPE-

K's high mobility and conductivity when doped preclude mobility measurement by more traditional methods such as SCLC. The mobilities obtained from each of these measurements are summarized in Table 4-1 and allow us to calculate the mobility for doped CPE-K on the nanoscale to be 4.18 x 10^3 $cm^2/V*s$.

$\mu_{cAFM\ undoped}$	$\mu_{device\ undoped}$	$\mu_{device\ doped}$	$\mu_{cAFM\ doped}$
3.48 x 10^{-4} $cm^2/V*s$	2 x 10^{-8} $cm^2/V*s$	2.4 x 10^{-1} $cm^2/V*s$	4.18 x 10^3 $cm^2/V*s$

Table 4-1. Mobility data from nano and bulk SCLC measurements

With the mobility of both doped and undoped CPE-K in the nanoscale, the number of charge carriers in a given area can be calculated by combining and rearranging Ohm's law and the differential form of Ohm's law – that is, $\sigma = nq\mu$ – to give equation (7)

$$n = \frac{It}{VAq\mu} \tag{7}$$

where I is the current, t is the film thickness, V is the voltage applied, A is the tip area, μ is the charge carrier mobility, and n is the charge carrier density. The number of electrons in the de-doped area around the bacteria is then determined by the area of the region under analysis, and the thickness of the film. The precise area around the bacteria to be used for analysis was determined by first counting only the pixels in the image with a negative value for current thus excluding the bacterium itself, which despite the current offset, registered a positive current value in the pA range. Then, pixels with a current value within one standard deviation of the average current in the area of interest were selected. The amount of area covered by each pixel, which was calculated by taking the area of the image and dividing it by the total number of pixels (512 x 512 pixels = 262144) was then multiplied by the number of pixels that met both current criteria as outlined above to give the actual area to be analyzed. The average current across the pixels around the bacteria identified for analysis was used to

calculate the volume in question, and the volume was multiplied by the carrier density to give the number of charges in that volume. The same analysis was done with an area of the image where there was no change in current on the CPE-K film due to the bacteria. The number of charges in the volume of CPE-K that has been de-doped was subtracted from the number of charges from the same volume of doped CPE-K to give the total number of electrons donated by the bacteria to CPE-K. *Via* this analysis on a number of different images and bacteria across multiple substrates, it is calculated that approximately $9 \times 10^5 \pm 6 \times 10^5$ electrons are transferred from the bacterium to the substrate, which is in line with previously reported estimates in literature that use microbial fuel cells. The large standard deviation is due to variation between the bacterium, which are living organisms, and to the presence of extracellular material on the surface, most likely riboflavin. An overlay of the current and morphology images, on the right in Figure 4-9, show areas of the CPE-K film that are slightly raised, which correspond to higher current areas in the film as seen in the image on the left in Figure 4-9.

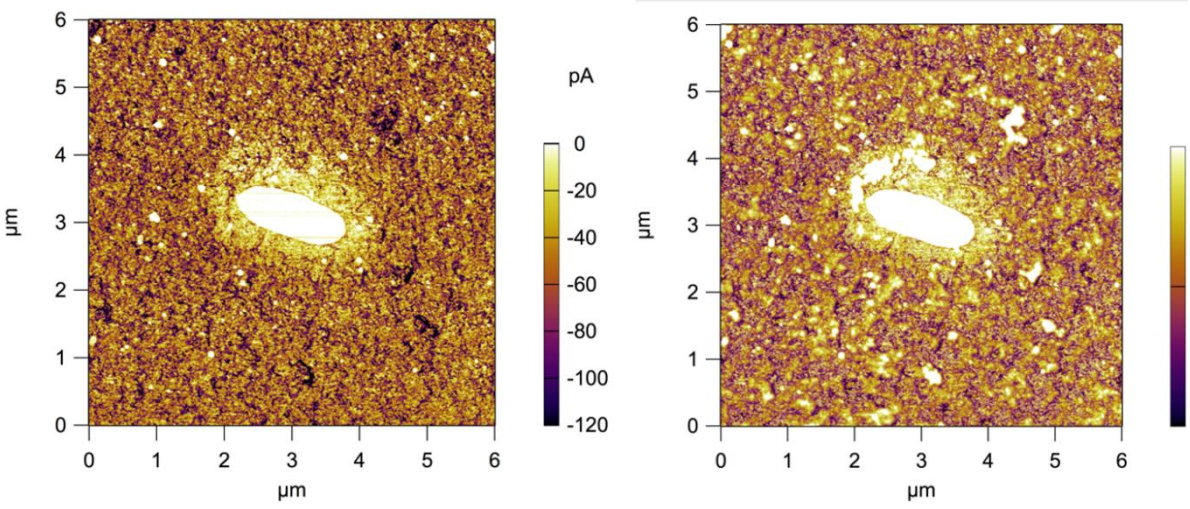

Figure 4-9. cAFM and morphology images of *G. sulfurreducens* on CPE-K

F. Experimental Section

1. Preparation of CPE-K films

2.25cm^2 glass substrates with a layer of indium tin oxide on top were cleaned via sonication in soapy DI water, DI water, acetone, and isopropanol. The substrates were then subjected to UV-ozone cleaning for 90 minutes (Jelite company UVO-cleaner Model #42). Approximately 5mg of CPE-K was weighed out in a dry 2mL glass vial cleaned by sonication in acetone and isopropanol, and then dissolved in Millipore water to give a 20mg/mL solution. This dark teal solution was heated with a heat gun to aid the dissolution of solids. Once cool, methanol was added to the solution to bring the concentration to 10 mg/mL. The dark teal solution was sonicated to create a homogenous solution, then 40 µL of the solution was spuncast onto the substrates at a speed of 1000 rpm for 2 minutes.

2. UV-vis-nIR Absorption Spectroscopy

All UV-vis-NIR absorption spectra were obtained using a Perkin-Elmer Lambda 750 UV-vis-NIR spectrometer. A 100% transmission blank was obtained using a clean indium tin oxide/glass substrate for all spectra with the exception of the spectrum of CPE-K in solution. A 100% transmission blank was obtained using a 50:50 mixture of Millipore water and methanol for the UV-vis-NIR spectrum of CPE-K in solution. All spectra were taken with a 1 nm resolution.

3. Preparation of G. sulfurreducens culture

Geobacter sulfurreducens (ATCC® 51573™) was purchased from American Type Culture Collection and cultured in anaerobic and sterile growth medium containing 1.5 g/L NH_4Cl, 0.6 g/L NaH_2PO_4, 0.1 g/L KCl, 2.5 g/L $NaHCO_3$, 0.82 g/L sodium acetate, 1.8 g/L

sodium fumarate, Wolfe's Vitamin and Modified Wolfe's Minerals as described in ATCC medium: ATCC® Medium 1957: Geobacter medium.[177] The culture was grown at 30 °C with anaerobic headspace containing 80% N_2 and 20% CO_2 for 5 days. Then the turbidity of the culture was measured by an OD meter to estimate cell concentration by assuming 10^8 bacteria cell/ml for 1 OD culture solution.

4. Preparation of G. sulfurreducens biofilm

CPE-K films were annealed at 300 ^oC for 30 minutes under a nitrogen atmosphere and then allowed to cool to room temperature. The CPE-K films were submerged in Millipore water of pH < 5 for 30 seconds, then dried under ambient conditions. 20mL of Millipore water was sparged with argon for 1 hour, then brought into an anaerobic chamber (Coy Vinyl Anaerobic Chamber) along with the CPE-K films, the G. *sulfurreducens* culture, a micropipetter, and small triangular pieces of cut filter paper. 20 µL of G. *sulfurreducens* culture at a concentration of approximately 6 x 10^5 cell/mL was dropcast onto a CPE-K film at O_2 concentrations less than 1000 ppm (0.1%). Excess solution was removed using the filter paper, taking care not to touch the surface of the film, leaving behind a small film of liquid on top. The same area onto which the G. *sulfurreducens* was dropcast was washed with 20 µL anaerobic Millipore water of pH > 6, and then the excess liquid was removed using procedure previously described. This washing procedure was repeated three times. The remaining liquid after washing was allowed to evaporate in the anaerobic chamber. Once dry, the films were transported under nitrogen to a separate glovebox that houses the atomic force microscope *via* a sealed transfer chamber.

5. Conductive-Atomic Force Microscopy (cAFM)

All topographic and current measurements were obtained using an Asylum MFP-3D operating in closed loop mode mounted atop an Olympus inverted optical microscope under an inert atmosphere. Pt/Cr coated silicon AFM tips with a resonant frequency of ~13 kHz and a force constant of ~0.2 N m^{-1} were used (Budget Sensors). All images were obtained at a force of 2 nN to ensure a constant electric field across all measurements at the same potential. Image flattening (1^{st} order to remove background slope) and processing was performed on Asylum Research AFM software, programmed using IGOR Pro. Local current-voltage curve measurements were obtained on the same system using the same tips at a force of 20 nN to ensure good electrical contact with the sample. The tip contact area was estimated using the Hertz model where the tip area was given by the manufacturer to be 25 nm, the Young's modulus of the Pt/Cr tip was 203 GPa, the Young's modulus of the polymer was 3 GPa, and the Poisson's ratio for Pt/Cr and the polymer was 0.35.[178] Samples were prepared by dissolving CPE-K into pH = 7 water, then spin-casting the solution onto cleaned indium tin oxide substrates to achieve a film with a thickness of 25 nm. The film was then annealed at 300 ^{o}C under nitrogen for 30 minutes, then allowed to cool before measurement.

6. High-resolution AFM

High resolution AFM image was obtained using a Bruker Multimode AFM operating under Bruker's ScanAsyst tapping mode. Silicon AFM tip on a nitride lever with a resonant frequency of ~70 kHz and a force constant of 0.4 N m^{-1} were used (Bruker ScanAsyst-Air).

7. Bulk-device current-voltage measurements

Bulk-device electrical measurements on undoped CPE-K were performed under N_2 using a Keithley 4200 semiconductor analyzer. Samples were prepared by dissolving CPE-K into pH = 7 water, then spin-casting the solution onto gold electrodes previously thermally evaporated onto glass to achieve a film with a thickness of approximately 350 nm. The film was then annealed at 300 ^oC under nitrogen for 30 minutes, then allowed to cool before gold electrodes were evaporated on top to give a diode area of 1 mm^2. The van der Pauw method was used in order to measure the Hall effect. It is a widely used method for measuring the Hall effect in thin films and two-dimensional materials.[135,136,179] The measurements of the Hall effect were carried out in a vacuum of 10-5 mbar. The magnetic field strength B and the electric current I were set to 0.63 T and 50 μA, respectively. Each experimental value of the Hall voltage VH was averaged by 15 successive measurements. The measurements of VH were carried out at different directions of electric current and orientations of the magnetic field in order to cancel out parasitic effects.

Chapter 5 − Conclusions

Understanding doping in its many forms and the parameters that govern doping, from the perspective of both the dopant and the OSC, is crucial for further progress towards a world where flexible organic electronics are ubiquitous and found in all different areas of our lives. This thesis builds upon the work of many others who have come before me and shows the community the benefit of Bronsted-acid doping and how we can employ it in different types of situations to dope unique classes of semiconductors. In addition, this thesis also provides an example of how p-doped organic semiconductors can also be used to help us better understand electron transfer processes between bacteria and their substrate by de-doping the polymer, and concept that can be extended to nano- and micro-catalysts and reductants. A summary of each section is provided below.

A. Understanding the doping mechanism of CPE-K

While the importance of having a pendant sulfonate side chain in the polymer for self-acid doping is known and recognized, the question of why it is necessary was unclear. With this work, we bring about a much better understanding of the importance of sulfonate and its role in the self-acid doping mechanism of CPE-K. By FTIR, we see new vibrational structures in the backbone that are consistent with increased rotational freedom of the CPDT unit due to protonation of CPDT, as well as a shift in the sulfonate peak, indicative of its role in stabilizing the polaron on the backbone. In addition, from the XPS data, we see a reduction in the K 2p peak with an increase in concentration of holes on the polymer backbone, which is consistent with sulfonate stabilizing the hole that is formed as the potassium counterion is no longer needed. The doping efficiency of CPE-K was also estimated, and though the doping efficiency is low, the mobility and conductivity of doped CPE-K is high. Given also the fact that water

is a ubiquitous solvent, CPE-K in a wide range of organic optoelectronic devices. In addition, the findings reveal that doping of CPE-K can be reversed by both heat and addition of a base, allowing for its use in a wide variety of applications including as a heat sensor and as a hole transporting layer to replace PEDOT:PSS in OLEDs, organic solar cells, and organic photodetectors. This work will help guide the synthetic design of new, highly conductive CPEs. Specifically, from this work we show the importance of having an electron-rich structural unit on the polymer that can be oxidized easily, as well as the necessity of having a pendant anionic group to stabilize the resulting positively charged backbone for self-doped polymer systems. This work also provides the experimental layout that is anticipated to promote efforts for conducting future studies on this class of materials.

B. Lewis acid doping

While Lewis acid doping is not a novel concept for the organic semiconductor community, it has not been commonly employed in the last couple of decades with the discovery and use of F_4TCNQ. After the discovery that BCF can be used for doping of organic semiconductors, interest in the area has grown. We have discovered not only that BCF dopes *via* formation of a BCF-water adduct that transfers a proton to the OSC followed by single electron transfer between a protonated and a non-protonated chain, we have also found that doping and Lewis acid-base reactions are direct competitors to each other.

In addition, stronger boron-based Lewis acids have been found, counterintuitively, to be worse dopants for OSCs primarily due to their inability to form stable complexes with water, a prerequisite to doping of OSCs. This also has a negative effect on the long-term doping stability for boron-based Lewis acids such as BCl_3 and BBr_3 since the doping mechanism is an equilibrium process that allows BCl_3 and BBr_3 to eventually degrade.

C. Using CPE-K to visualize electron transfer from bacteria

Our work has confirmed that *G. sulfurreducens* has the ability to transfer electrons to a surface without the use of electrically conductive pili, lending credence to work claiming electron transfer from *G. sulfurreducens* occurs mainly through direct contact with outer membrane cytochromes or *via* redox-mediators such as flavins. In addition, using CPEs as the surface onto which *G. sulfurreducens* was deposited has allowed for unique, single-cell qualitative and quantitative study on the electron transfer mechanism for *G. sulfurreducens* by cAFM. By visualizing how efficiently bacterium transfer electrons and some of the issues that underlie inefficiencies in electron transfer from bacterium to the substrate, a better understanding for how to improve the efficiency in microbial fuel cells can be obtained. More broadly, we envision this combined use of CPEs and cAFM to be applied not only to other electrogenic bacteria, but also to nano- and micro-catalysts, opening up new avenues of study for electron transfer reactions on the nanoscale.

Chapter 6 − References

1. Spear, W. E. & Comber, P. G. Le. Substitutional Doping of Amorphous Silicon. *Solid State Commun.* **17**, 1193–1196 (1975).
2. Fripp, A. L. Dependence of resistivity on the doping level of polycrystalline silicon. *J. Appl. Phys.* **46**, 1240–1244 (1975).
3. Wong, J. H., Royapoor, M. & Chan, C. W. Review of life cycle analyses and embodied energy requirements of single-crystalline and multi-crystalline silicon photovoltaic systems. *Renew. Sustain. Energy Rev.* **58**, 608–618 (2016).
4. Bhandari, K. P., Collier, J. M., Ellingson, R. J. & Apul, D. S. Energy payback time (EPBT) and energy return on energy invested (EROI) of solar photovoltaic systems : A systematic review and meta-analysis. *Renew. Sustain. Energy Rev.* **47**, 133–141 (2015).
5. Someya, T. *et al.* Conformable, flexible, large-area networks of pressure and thermal sensors with organic transistor active matrixes. *Proc. Natl. Acad. Sci. U. S. A.* **102**, 12321 LP – 12325 (2005).
6. Root, S. E., Savagatrup, S., Printz, A. D., Rodriquez, D. & Lipomi, D. J. Mechanical Properties of Organic Semiconductors for Stretchable, Highly Flexible, and Mechanically Robust Electronics. *Chem. Rev.* **117**, 6467–6499 (2017).
7. Yi, H. T., Payne, M. M., Anthony, J. E. & Podzorov, V. Ultra-flexible solution-processed organic field-effect transistors. *Nat. Commun.* **3**, 1259 (2012).
8. Galagan, Y. *et al.* Technology development for roll-to-roll production of organic photovoltaics. *Chem. Eng. Process. Process Intensif.* **50**, 454–461 (2011).
9. Brown, A. R., Jarrett, C. P., de Leeuw, D. M. & Matters, M. Field-effect transistors made from solution-processed organic semiconductors. *Synth. Met.* **88**, 37–55 (1997).
10. Brabec, C. J. Organic photovoltaics: technology and market. *Sol. Energy Mater. Sol. Cells* **83**, 273–292 (2004).
11. Brabec, C. J., Hauch, J. A., Schilinsky, P. & Waldauf, C. Production Aspects of Organic Photovoltaics and Commercialization of Devices. *MRS Bull.* **30**, 50–52 (2005).
12. Chiang, C. K. *et al.* Conducting polymers: Halogen doped polyacetylene. *J. Chem. Phys.* **69**, 5098 (1978).
13. Chiang, C. K. *et al.* Electrical conductivity in doped polyacetylene. *Phys. Rev. Lett.* **39**, 1098–1101 (1977).
14. Chiang, C. K., Gau, S. C., Park, Y. W., Macdiarmid, A. G. & Heeger, A. J. Polyacetylene , (CH) x : n-type and p-type doping and compensation. *Appl. Phys. Lett.* **33**, 18–20 (1978).
15. Heeger, A., MacDiarmid, A. G. & Shirakawa, H. The Nobel Prize in chemistry, 2000: conductive polymers. *Stock. Sweden R. Swedish Acad. Sci.* 1–16 (2000) doi:http://www.nobelprize.org/nobel_prizes/chemistry/laureates/2000/advanced-chemistryprize2000.pdf.
16. Fincher, C. R., Ozaki, M., Heeger, A. J. & MacDiarmid, A. G. Donor and acceptor states in lightly doped polyacetylene, (CH)x. *Phys. Rev. B* **19**, 4140–4148 (1979).
17. Shirakawa, H., Louis, E. J., MacDiarmid, A. G., Chiang, C. K. & Heeger, A. J. Synthesis of electrically conducting organic polymers: Halogen derivatives of polyacetylene, (CH)x. *J. Chem. Soc. Chem. Commun.* 578–580 (1977)

doi:10.1039/C39770000578.
18. Shirakawa, H., Ito, T. & Ikeda, S. Electrical properties of polyacetylene with various cis-trans compositions. *Die Makromol. Chemie* **179**, 1565–1573 (1978).
19. Warta, W. & Karl, N. naphthalene: High, electric-field-dependent. *Phys. Rev. B* **32**, 1172–1182 (1985).
20. Karl, N. Charge carrier transport in organic semiconductors. *Synth. Met.* **133**–**134**, 649–657 (2003).
21. Horowitz, G., Peng, X.-Z., Fichou, D. & Garnier, F. Role of the semiconductor/insulator interface in the characteristics of π-conjugated-oligomer-based thin-film transistors. *Synth. Met.* **51**, 419–424 (1992).
22. Gundlach, D. J., Lin, Y. Y., Jackson, T. N., Nelson, S. F. & Schlom, D. G. Pentacene organic thin-film transistors-molecular ordering and mobility. *IEEE Electron Device Lett.* **18**, 87–89 (1997).
23. Lin, Y.-., Gundlach, D. J., Nelson, S. F. & Jackson, T. N. Stacked pentacene layer organic thin-film transistors with improved characteristics. *IEEE Electron Device Lett.* **18**, 606–608 (1997).
24. Horowitz, G., Fichou, D., Peng, X. & Garnier, F. Thin-film transistors based on alpha-conjugated oligomers. *Synth. Met.* **41**, 1127–1130 (1991).
25. Klauk, H., Gundlach, D. J., Nichols, J. A. & Jackson, T. N. Pentacene organic thin-film transistors for circuit and display applications. *IEEE Trans. Electron Devices* **46**, 1258–1263 (1999).
26. Rang, Z. *et al.* Hydrostatic-pressure dependence of the photoconductivity of single-crystal pentacene and tetracene. *Appl. Phys. Lett.* **79**, 2731–2733 (2001).
27. Laquindanum, J. G., Katz, H. E. & Lovinger, A. J. Synthesis, Morphology, and Field-Effect Mobility of Anthradithiophenes. *J. Am. Chem. Soc.* **120**, 664–672 (1998).
28. Garnier, F. *et al.* Molecular engineering of organic semiconductors: design of self-assembly properties in conjugated thiophene oligomers. *J. Am. Chem. Soc.* **115**, 8716–8721 (1993).
29. Facchetti, A. *et al.* Building Blocks for N-Type Molecular and Polymeric Electronics. Perfluoroalkyl- versus Alkyl-Functionalized Oligothiophenes (nTs; n = 2−6). Systematic Synthesis, Spectroscopy, Electrochemistry, and Solid-State Organization. *J. Am. Chem. Soc.* **126**, 13480–13501 (2004).
30. Murphy, A. R., Fréchet, J. M. J., Chang, P., Lee, J. & Subramanian, V. Organic Thin Film Transistors from a Soluble Oligothiophene Derivative Containing Thermally Removable Solubilizing Groups. *J. Am. Chem. Soc.* **126**, 1596–1597 (2004).
31. Meng, H., Bao, Z., Lovinger, A. J., Wang, B.-C. & Mujsce, A. M. High Field-Effect Mobility Oligofluorene Derivatives with High Environmental Stability. *J. Am. Chem. Soc.* **123**, 9214–9215 (2001).
32. Li, X.-C. *et al.* A Highly π-Stacked Organic Semiconductor for Thin Film Transistors Based on Fused Thiophenes. *J. Am. Chem. Soc.* **120**, 2206–2207 (1998).
33. Bao, Z., Dodabalapur, A. & Lovinger, A. J. Soluble and processable regioregular poly(3-hexylthiophene) for thin film field-effect transistor applications with high mobility. *Appl. Phys. Lett.* **69**, 4108–4110 (1996).
34. Inganäs, O., Salaneck, W. R., Österholm, J.-E. & Laakso, J. Thermochromic and solvatochromic effects in poly(3-hexylthiophene). *Synth. Met.* **22**, 395–406 (1988).
35. Pron, A. & Rannou, P. Processible conjugated polymers: from organic

semiconductors to organic metals and superconductors. *Prog. Polym. Sci.* **27**, 135–190 (2002).
36. McCullough, R. D. The Chemistry of Conducting Polythiophenes. *Adv. Mater.* **10**, 93–116 (1998).
37. Usta, H., Lu, G., Facchetti, A. & Marks, T. J. Dithienosilole− and Dibenzosilole−Thiophene Copolymers as Semiconductors for Organic Thin-Film Transistors. *J. Am. Chem. Soc.* **128**, 9034–9035 (2006).
38. Chan, C. Y. H., Chow, C. M. & So, S. K. Using transistor technique to study the effects of transition metal oxide dopants on organic charge transporters. *Org. Electron.* **12**, 1454–1458 (2011).
39. Kröger, M. *et al.* P-type doping of organic wide band gap materials by transition metal oxides: A case-study on Molybdenum trioxide. *Org. Electron.* **10**, 932–938 (2009).
40. Lehnhardt, M. *et al.* Charge carrier densities in chemically doped organic semiconductors verified by two independent techniques. *Appl. Phys. Lett.* **96**, 193301 (2010).
41. Qi, Y. *et al.* A Molybdenum Dithiolene Complex as p-Dopant for Hole-Transport Materials: A Multitechnique Experimental and Theoretical Investigation. *Chem. Mater.* **22**, 524–531 (2010).
42. Kröger, M. *et al.* Role of the deep-lying electronic states of MoO3 in the enhancement of hole-injection in organic thin films. *Appl. Phys. Lett.* **95**, 123301 (2009).
43. Meyer, J. *et al.* A strategy towards p-type doping of organic materials with HOMO levels beyond 6 eV using tungsten oxide. *J. Mater. Chem.* **19**, 702–705 (2009).
44. Zhang, D. *et al.* Role of Fe3O4 as a p-Dopant in Improving the Hole Injection and Transport of Organic Light-Emitting Devices. *IEEE J. Quantum Electron.* **47**, 591–596 (2011).
45. Kao, C. Y. *et al.* Doping of Conjugated Polythiophenes with Alkyl Silanes. *Adv. Funct. Mater.* **19**, 1906–1911 (2009).
46. Ausserlechner, S. J. *et al.* Mechanism of surface proton transfer doping in pentacene based organic thin-film transistors. *Phys. status solidi* **209**, 181–192 (2012).
47. Ćirić-Marjanović, G. Recent advances in polyaniline research: Polymerization mechanisms, structural aspects, properties and applications. *Synth. Met.* **177**, 1–47 (2013).
48. Sharma, G. D., Sangodkar, S. G. & Roy, M. S. Influence of iodine on the electrical and photoelectrical properties of zinc phthalocyanine thin film devices. *Mater. Sci. Eng. B* **41**, 222–227 (1996).
49. Jakabovič, J. *et al.* Surface and interface analysis of iodine-doped pentacene structures for OTFTs. *Surf. Interface Anal.* **43**, 518–521 (2011).
50. Abdou, M. S. A., Orfino, F. P., Son, Y. & Holdcroft, S. Interaction of Oxygen with Conjugated Polymers: Charge Transfer Complex Formation with Poly(3-alkylthiophenes). *J. Am. Chem. Soc.* **119**, 4518–4524 (1997).
51. Lu, C.-K. & Meng, H.-F. Hole doping by molecular oxygen in organic semiconductors: Band-structure calculations. *Phys. Rev. B* **75**, 235206 (2007).
52. Meijer, E. J. *et al.* Dopant density determination in disordered organic field-effect transistors. *J. Appl. Phys.* **93**, 4831–4835 (2003).

53. Meyer, J. *et al.* Transition Metal Oxides for Organic Electronics: Energetics, Device Physics and Applications. *Adv. Mater.* **24**, 5408–5427 (2012).
54. Lee, J.-H., Kim, H.-M., Kim, K.-B. & Kim, J.-J. Origin of charge generation efficiency of metal oxide p-dopants in organic semiconductors. *Org. Electron.* **12**, 950–954 (2011).
55. Xu, M. *et al.* Improvement in Solid-State Dye Sensitized Solar Cells by p-Type Doping with Lewis Acid SnCl4. *J. Phys. Chem. C* **117**, 22492–22496 (2013).
56. Endo, J., Matsumoto, T. & Kido, J. Organic Electroluminescent Devices with a Vacuum-Deposited Lewis-Acid-Doped Hole-Injecting Layer. *Jpn. J. Appl. Phys.* **41**, L358–L360 (2002).
57. Genoud, F. *et al.* Lewis Acid Doped Polyaniline. Part II: Spectroscopic Studies of Emeraldine Base and Emeraldine Hydrochloride Complexation with FeCl3. *Chem. Mater.* **12**, 744–749 (2000).
58. Ganzorig, C. & Fujihira, M. Improved drive voltages of organic electroluminescent devices with an efficient p-type aromatic diamine hole-injection layer. *Appl. Phys. Lett.* **77**, 4211–4213 (2000).
59. Duclaux, L. Review of the doping of carbon nanotubes (multiwalled and single-walled). *Carbon N. Y.* **40**, 1751–1764 (2002).
60. Mathieu, B. & Ghosez, L. Trimethylsilyl bis(trifluoromethanesulfonyl)imide as a tolerant and environmentally benign Lewis acid catalyst of the Diels–Alder reaction. *Tetrahedron* **58**, 8219–8226 (2002).
61. Ishihara, K., Kubota, M., Kurihara, H. & Yamamoto, H. Scandium Trifluoromethanesulfonate as an Extremely Active Lewis Acid Catalyst in Acylation of Alcohols with Acid Anhydrides and Mixed Anhydrides. *J. Org. Chem.* **61**, 4560–4567 (1996).
62. Fringuelli, F., Pizzo, F. & Vaccaro, L. AlCl3 as an efficient Lewis acid catalyst in water. *Tetrahedron Lett.* **42**, 1131–1133 (2001).
63. Kovacic, P. & Lange, R. M. A Convenient , New Synthesis of p-Sexiphenyl from Biphenyl or p-Terphenyl in the Presence of Lewis Acid Catalyst-Oxidant1. **1**, 2416–2420 (1963).
64. Kovacic, P. & Oziomek, J. p-Polyphenyl from Benzene-Lewis Acid Catalyst-Oxidant . Reaction Scope and Investigation of the Benzene-Aluminum Chloride-Cupric Chloride System1. 100–104 (1963) doi:10.1021/jo01024a023.
65. Kuhn, S. J. & McIntyre, J. S. Reactions of Amides and Related Compounds. *Can. J. Chem.* **43**, 375–380 (1965).
66. Yang, X., Stern, C. L. & Marks, T. J. Cationic Zirconocene Olefin Polymerization Catalysts Based on the Organo-Lewis Acid Tris (pentafluorophenyl) borane. A Synthetic , Structural , Solution Dynamic , and Polymerization Catalytic Study. *J. Am. Chem. Soc.* **116**, 10015–10031 (1994).
67. Pingel, P. *et al.* p-Type Doping of Poly(3-hexylthiophene) with the Strong Lewis Acid Tris(pentafluorophenyl)borane. *Adv. Electron. Mater.* 1600204 (2016) doi:10.1002/aelm.201600204.
68. Han, Y. *et al.* Doping of Large Ionization Potential Indenopyrazine Polymers via Lewis Acid Complexation with Tris(pentafluorophenyl)borane: A Simple Method for Improving the Performance of Organic Thin-Film Transistors. *Chem. Mater.* **28**, 8016–8024 (2016).

69. Piers, W. E. & Chivers, T. Pentafluorophenylboranes: From obscurity to applications. *Chem. Soc. Rev.* **26**, 345–354 (1997).
70. Ye, T., Wang, J., Chen, W., Yang, Y. & He, D. Improved Performance and Reproducibility of Perovskite Solar Cells by Well-Soluble Tris(pentafluorophenyl)borane as a p-Type Dopant. *ACS Appl. Mater. Interfaces* **9**, 17923–17931 (2017).
71. Yurash, B. *et al.* Atomic-Level Insight into the Postsynthesis Band Gap Engineering of a Lewis Base Polymer Using Lewis Acid Tris(pentafluorophenyl)borane. *Chem. Mater.* (2019) doi:10.1021/acs.chemmater.9b01224.
72. Yurash, B. *et al.* Towards understanding the doping mechanism of organic semiconductors by Lewis acids. *Nat. Mater.* (2019) doi:10.1038/s41563-019-0479-0.
73. Brocks, G. Theoretical study of the charge transfer in the organic crystal of dimethylquaterthiophene and tetrafluoro-tetracyanoquinodimethane. *Phys. Rev. B* **55**, 6816–6819 (1997).
74. Pfeiffer, M., Beyer, A., Fritz, T. & Leo, K. Controlled doping of phthalocyanine layers by cosublimation with acceptor molecules: A systematic Seebeck and conductivity study. *Appl. Phys. Lett.* **73**, 3202–3204 (1998).
75. Gao, W. & Kahn, A. Controlled p doping of the hole-transport molecular material N,N′-diphenyl-N,N′-bis(1-naphthyl)-1,1′-biphenyl-4,4′-diamine with tetrafluorotetracyanoquinodimethane. *J. Appl. Phys.* **94**, 359–366 (2003).
76. Yim, K.-H. *et al.* Controlling Electrical Properties of Conjugated Polymers via a Solution-Based p-Type Doping. *Adv. Mater.* **20**, 3319–3324 (2008).
77. Hwang, J. & Kahn, A. Electrical doping of poly(9,9-dioctylfluorenyl-2,7-diyl) with tetrafluorotetracyanoquinodimethane by solution method. *J. Appl. Phys.* **97**, 103705 (2005).
78. Scholes, D. T. *et al.* The Effects of Crystallinity on Charge Transport and the Structure of Sequentially Processed F4TCNQ-Doped Conjugated Polymer Films. *Adv. Funct. Mater.* **27**, 1702654 (2017).
79. Lim, E., Peterson, K. A., Su, G. M. & Chabinyc, M. L. Thermoelectric Properties of Poly(3-hexylthiophene) (P3HT) Doped with 2,3,5,6-Tetrafluoro-7,7,8,8-tetracyanoquinodimethane (F4TCNQ) by Vapor-Phase Infiltration. *Chem. Mater.* **30**, 998–1010 (2018).
80. Scholes, D. T. *et al.* Overcoming Film Quality Issues for Conjugated Polymers Doped with F4TCNQ by Solution Sequential Processing: Hall Effect, Structural, and Optical Measurements. *J. Phys. Chem. Lett.* **6**, 4786–4793 (2015).
81. Jacobs, I. E. *et al.* Comparison of solution-mixed and sequentially processed P3HT:F4TCNQ films: effect of doping-induced aggregation on film morphology. *J. Mater. Chem. C* **4**, 3454–3466 (2016).
82. Han, C. C. & Elsenbaumer, R. L. Protonic acids: Generally applicable dopants for conducting polymers. *Synth. Met.* **30**, 123–131 (1989).
83. Chen, S.-A. & Hwang, G.-W. Water-Soluble Self-Acid-Doped Conducting Polyaniline: Structure and Properties. *J. Am. Chem. Soc.* **117**, 10055–10062 (1995).
84. Chen, S. A. & Hua, M.-Y. Structure and doping level of the self-acid-doped conjugated conducting polymers: poly [n-(3'-thienyl) alkanesulfonic acids]. *Macromolecules* **26**, 7108–7110 (1993).
85. Chang, E.-C., Hua, M. & Chen, S.-A. Synthesis and Properties of the Water-Soluble

Self-Acid-Doped Polypyrrole: Poly[4-(3-pyrrolyl)butanesulfonicacid]. *J. Polym. Res.* **5**, 249–254 (1998).
86. Chen, S.-A. & Lin, L.-C. Polyaniline Doped by the New Class of Dopant, Ionic Salt: Structure and Properties. *Macromolecules* **28**, 1239–1245 (1995).
87. Patil, A. O., Ikenoue, Y., Wudl, F. & Heeger, A. J. Water-Soluble Conducting Polymers. *J. Am. Chem. Soc.* **109**, 1858–1859 (1987).
88. Ikenoue, Y., Outani, N., Patil, A. O., Wudl, F. & Heeger, A. J. Electrochemical studies of self-doped conducting polymers: Verification of the 'cation-popping' doping mechanism. *Synth. Met.* **30**, 305–319 (1989).
89. Chayer, M., Faïd, K. & Leclerc, M. Highly Conducting Water-Soluble Polythiophene Derivatives. *Chem. Mater.* **9**, 2902–2905 (1997).
90. Hua, M.-Y., Yang, S.-W. & Chen, S.-A. Sensitive Thermal-Undoping Characteristics of the Self-Acid-Doped Conjugated Conducting Polymer Poly[2-(3'-thienyl)ethanesulfonic acid]. *Chem. Mater.* **9**, 2750–2754 (1997).
91. Shi, S. & Wudl, F. Synthesis and Characterization of a Water-Soluble Poly (p-phenylenevinylene) Derivative. *Am. Chem. Soc.* **23**, 2119–2124 (1990).
92. Mai, C. K. *et al.* SI - Facile doping of anionic narrow-band-gap conjugated polyelectrolytes during dialysis. *Angew. Chemie - Int. Ed.* **52**, 12874–12878 (2013).
93. Mai, C.-K. *et al.* Varying the ionic functionalities of conjugated polyelectrolytes leads to both p- and n-type carbon nanotube composites for flexible thermoelectrics. *Energy Environ. Sci.* **8**, 2341–2346 (2015).
94. Lee, W., Seo, J. H. & Woo, H. Y. Conjugated polyelectrolytes: A new class of semiconducting material for organic electronic devices. *Polymer (Guildf).* **54**, 5104–5121 (2013).
95. Seo, J. H. *et al.* Improved injection in n-type organic transistors with conjugated polyelectrolytes. *J. Am. Chem. Soc.* **131**, 18220–18221 (2009).
96. Luo, J. *et al.* Enhanced open-circuit voltage in polymer solar cells. *Appl. Phys. Lett.* **95**, 1–3 (2009).
97. Pu, K. Y. & Liu, B. Intercalating dye harnessed cationic conjugated polymer for real-time naked-eye recognition of double-stranded dna in serum. *Adv. Funct. Mater.* **19**, 1371–1378 (2009).
98. Cimrová, V. *et al.* Efficient blue light emitting devices based on rigid-rod polyelectrolytes. *Adv. Mater.* **8**, 585–588 (1996).
99. Hoven, C. V., Garcia, A., Bazan, G. C. & Nguyen, T. Q. Recent applications of conjugated polyelectrolytes in optoelectronic devices. *Adv. Mater.* **20**, 3793–3810 (2008).
100. Zhou, H. *et al.* Solution-processed pH-neutral conjugated polyelectrolyte improves interfacial contact in organic solar cells. *ACS Nano* **9**, 371–377 (2015).
101. Shin, Y. C. *et al.* Cell imaging and DNA delivery in fibroblastic cells by conjugated polyelectrolytes. *Biotechnol. Appl. Biochem.* **60**, 580–588 (2013).
102. Zhou, H. *et al.* Polymer homo-tandem solar cells with best efficiency of 11.3%. *Adv. Mater.* **27**, 1767–1773 (2015).
103. Sun, M., Lan, L., Wang, L., Peng, J. & Cao, Y. Synthesis of Novel Conjugated Polyelectrolytes for Organic Field-Effect Transistors Gate Dielectric Materials. *Macromol. Chem. Phys.* **209**, 2504–2509 (2008).
104. Lee, B. H. *et al.* Multi-Charged Conjugated Polyelectrolytes as a Versatile Work

Function Modifi er for Organic Electronic Devices. *Adv. Funct. Mater.* **24**, 1100–1108 (2014).
105. Kang, Q. *et al.* p - Doped Conducting Polyelectrolyte as an Anode Interlayer Enables High Efficiency for 1 cm 2 Printed Organic Solar Cells. *ACS Appl. Mater. Interfaces* **11**, 20205–20213 (2019).
106. Han, Y. W. *et al.* Vertical Phase Separation for Highly Efficient Organic Solar Cells Incorporating Conjugated-Polyelectrolytes. *Adv. Mater. Interfaces* **6**, 1–15 (2019).
107. Bi, S. *et al.* Interfacial Modification in Organic and Perovskite Solar Cells. *Adv. Mater.* **1805708**, 1–8 (2019).
108. Moon, S. *et al.* Hole transport layer based on conjugated polyelectrolytes for polymer solar cells. *J. Colloid Interface Sci.* **518**, 21–26 (2018).
109. Kim, S. *et al.* Improved Interfacial Crystallization by Synergic Effects of Precursor Solution Stoichiometry and Conjugated Polyelectrolyte Interlayer for High Open-Circuit Voltage of Perovskite Photovoltaic Diodes. *ACS Appl. Mater. Interfaces* (2020) doi:10.1021/acsami.9b22283.
110. Lee, B. R. *et al.* Conjugated Polyelectrolytes as Efficient Hole Transport Layers in Perovskite Light-Emitting Diodes. *ACS Nano* **12**, 5826–5833 (2018).
111. Brus, V. V. *et al.* Conjugated Polyelectrolyte/Graphene Hetero-Bilayer Nanocomposites Exhibit Temperature Switchable Type of Conductivity. *Adv. Electron. Mater.* **1600515**, 1–7 (2017).
112. Havinga, E. E., Hoeve, W. & W, E. Water-Soluble Self-Doped 3-Substituted Polypyrroles. *Chem. Mater.* **1**, 650–659 (1989).
113. Yue, J. & Epstein, A. J. XPS Study of Self-Doped Conducting Polyaniline and Parent Systems. *Macromolecules* **24**, 4441–4445 (1991).
114. Child, A. D. & Reynolds, J. R. Water-Soluble Rigid-Rod Polyelectrolytes: A New Self-Doped, Electroactive Sulfonatoalkoxy-Substituted Poly(p-phenylene). *Macromolecules* **27**, 1975–1977 (1994).
115. Havinga, E. E., van Horssen, L. W., Hoeve, W. ten, Wynberg, H. & Meijer, E. W. Self-doped water-soluble conducting polymers. *Polym. Bull.* **29**, 119–126 (1987).
116. Yue, J., Wang, Z. H., Cromack, K. R., Epstein, A. J. & MacDiarmid, A. G. Effect of Sulfonic Acid Group on Polyaniline Backbone. *J. Am. Chem. Soc.* **113**, 2665–2671 (1991).
117. Chen, S.-A. & Hwang, G.-W. Structure Characterization of Self-Acid-Doped Sulfonic Acid Ring-Substituted Polyaniline in Its Aqueous Solutions and as Solid Film. *Macromolecules* **29**, 3950–3955 (1996).
118. NIST X-ray Photoelectron Spectroscopy (XPS) Database. *US Department of Commerce* (2012).
119. Aygül, U. *et al.* Electronic Properties of Interfaces between PCPDTBT and Prototypical Electrodes Studied by Photoemission Spectroscopy. *ChemPhysChem* **12**, 2345–2351 (2011).
120. Salaneck, W. R. & Thomas, H. R. Energy-Gain Satellite Structure in the C(1s) X-ray Photoemission Spectra of Organic Macromolecules. *Solid State Commun.* **27**, 685–689 (1978).
121. Gardella, J. A., Ferguson, S. A. & Chin, R. L. Pi*<-pi shake-up satellites for the analysis of structure and bonding in aromatic polymers by X-ray photoelectron spectroscopy. *Appl. Spectrosc.* **40**, 224–232 (1986).

122. Xie, Y. & Sherwood, P. M. A. X-ray photoelectron-spectroscopic studies of carbon fiber surfaces. Part IX: the effect of microwave plasma treatment on carbon fiber surfaces. *Appl. Spectrosc.* **44**, 797–803 (1990).
123. Bubnova, O. *et al.* Optimization of the thermoelectric figure of merit in the conducting polymer poly(3,4-ethylenedioxythiophene). *Nat. Mater.* **10**, 429–433 (2011).
124. Zotti, G. *et al.* Electrochemical and XPS studies toward the role of monomeric and polymeric sulfonate counterions in the synthesis, composition, and properties of poly(3,4-ethylenedioxythiophene). *Macromolecules* **36**, 3337–3344 (2003).
125. Chia, P. J. *et al.* Direct evidence for the role of the madelung potential in determining the work function of doped organic semiconductors. *Phys. Rev. Lett.* **102**, 1–4 (2009).
126. Wu, K. *et al.* Thermoresponsiveness of hybrid micelles from poly(ethylene glycol)-block-poly(4-vinylpyridium) cations and so42- anions in aqueous solutions. *Langmuir* **22**, 1474–1477 (2006).
127. Socrates, G. *Infrared and Raman characteristic group frequencies : tables and charts*. (John Wiley & Sons Ltd, 2001).
128. Mai, C. K. *et al.* Facile doping of anionic narrow-band-gap conjugated polyelectrolytes during dialysis. *Angew. Chemie - Int. Ed.* **52**, 12874–12878 (2013).
129. Anderson, M. *et al.* Displacement of polarons by vibrational modes in doped conjugated polymers. *Phys. Rev. Mater.* **1**, 055604 (2017).
130. Beljonne, D. *et al.* Optical signature of delocalized polarons in conjugated polymers. *Adv. Funct. Mater.* **11**, 229–234 (2001).
131. Tsokkou, D. *et al.* Excited State Dynamics of a Self-Doped Conjugated Polyelectrolyte. *Adv. Funct. Mater.* **1906148**, 1–13 (2020).
132. Scholes, D. T. *et al.* Overcoming Film Quality Issues for Conjugated Polymers Doped with F4TCNQ by Solution Sequential Processing: Hall Effect, Structural, and Optical Measurements. *J. Phys. Chem. Lett.* **6**, 4786–4793 (2015).
133. Scholes, D. T. *et al.* The Effects of Crystallinity on Charge Transport and the Structure of Sequentially Processed F4TCNQ-Doped Conjugated Polymer Films. *Adv. Funct. Mater.* **27**, 1–13 (2017).
134. Vona, M. L. Di *et al.* Analysis of Temperature-Promoted and Solvent-Assisted Cross-Linking in Sulfonated Poly (ether ether ketone) (SPEEK) Proton-Conducting Membranes. *J. Phys. Chem. B* **113**, 7505–7512 (2009).
135. van der Pauw, L. J. A method of measuring the resistivity and Hall coefficient on lamellae of arbitrary shape. *Philips Technical Review* vol. 20 220–224 (1958).
136. Grundmann, M. *Physics of Semiconductors*. (Springer, 2010).
137. Berkefeld, A., Piers, W. E. & Parvez, M. Tandem frustrated lewis pair/tris(pentafluorophenyl)borane-catalyzed deoxygenative hydrosilylation of carbon dioxide. *J. Am. Chem. Soc.* **132**, 10660–10661 (2010).
138. Harlan, C. J., Hascall, T., Fujita, E. & Norton, J. R. The one-electron oxidation of an azazirconacyclobutene in the presence of B(C6F5)3 [7]. *J. Am. Chem. Soc.* **121**, 7274–7275 (1999).
139. Fărcaşui, D. & Ghenciu, A. Evaluation of acidity of strong acid catalysts I. The strength of boron trifluoride-water systems. *J. Catal.* **134**, 126–133 (1992).
140. Jonas, V., Frenking, G. & Reetz, M. T. Comparative Theoretical Study of Lewis Acid-Base Complexes of BH3, BF3, BCl3, AlCl3, and SO2. *J. Am. Chem. Soc.* **116**,

8741–8753 (1994).
141. Kulszewicz-Bajer, I. *et al.* Lewis Acid Doped Polyaniline: Preparation and Spectroscopic Characterization. *Chem. Mater.* **11**, 552–556 (1999).
142. Müller, L. O. *et al.* Simple access to the non-oxidizing Lewis superacid PhF→Al(OR F) 3 (R F = C (CF 3) 3). *Angew. Chemie - Int. Ed.* **47**, 7659–7663 (2008).
143. Sivaev, I. B. & Bregadze, V. I. Lewis acidity of boron compounds. *Coord. Chem. Rev.* **270**–**271**, 75–88 (2014).
144. Welch, G. C., Coffin, R., Peet, J. & Bazan, G. C. Band Gap Control in Conjugated Oligomers via Lewis Acids. *J. Am. Chem. Soc.* **131**, 10802–10803 (2009).
145. Welch, G. C. & Bazan, G. C. Lewis Acid Adducts of Narrow Band Gap Conjugated Polymers. *J. Am. Chem. Soc.* **133**, 4632–4644 (2011).
146. Yurash, B. *et al.* Complete Picture of Bandgap Engineering in a Lewis Basic Polymer Using the Lewis Acid Tris(pentafluorophenyl)borane, B(C6F5)3. *Prep.*
147. Kwaan, R. J., Harlan, C. J. & Norton, J. R. Generation and characterization of the tris(pentafluorophenyl)borane radical anion. *Organometallics* **20**, 3818–3820 (2001).
148. Sze, S. M. & Ng, K. K. *Physics of Semiconductor Devices*. (John Wiley & Sons, Inc, 2007).
149. Phan, H., Wang, M., Bazan, G. C. & Nguyen, T. Q. Electrical Instability Induced by Electron Trapping in Low-Bandgap Donor-Acceptor Polymer Field-Effect Transistors. *Adv. Mater.* **27**, 7004–7009 (2015).
150. Beckett, M. A., Strickland, G. C., Holland, J. R. & Sukumar Varma, K. A convenient n.m.r. method for the measurement of Lewis acidity at boron centres: correlation of reaction rates of Lewis acid initiated epoxide polymerizations with Lewis acidity. *Polymer (Guildf).* **37**, 4629–4631 (1996).
151. Gutmann, V. Solvent effects on the reactivities of organometallic compounds. *Coord. Chem. Rev.* **18**, 225–255 (1976).
152. Ying, L. *et al.* Regioregular Pyridal[2,1,3]thiadiazole π-Conjugated Copolymers. *J. Am. Chem. Soc.* **133**, 18538–18541 (2011).
153. Rabaey, K. & Verstraete, W. Microbial fuel cells: Novel biotechnology for energy generation. *Trends Biotechnol.* **23**, 291–298 (2005).
154. Strycharz-Glaven, S. M., Snider, R. M., Guiseppi-Elie, A. & Tender, L. M. On the electrical conductivity of microbial nanowires and biofilms. *Energy Environ. Sci.* **4**, 4366 (2011).
155. Reguera, G. *et al.* Extracellular electron transfer via microbial nanowires. *Nature* **435**, 1098–1101 (2005).
156. Shi, L. *et al.* The roles of outer membrane cytochromes of Shewanella and Geobacter in extracellular electron transfer. *Environ. Microbiol. Rep.* **1**, 220–227 (2009).
157. Mehta, T., Coppi, M. V, Childers, S. E. & Lovley, D. R. Outer Membrane c -Type Cytochromes Required for Fe (III) and Mn (IV) Oxide Reduction in Geobacter sulfurreducens. *Appl. Environ. Microbiol.* **71**, 8634–8641 (2005).
158. Okamoto, A. *et al.* Uptake of self-secreted flavins as bound cofactors for extracellular electron transfer in Geobacter species. *Energy Environ. Sci.* **7**, 1357–1361 (2014).
159. Phan, H. *et al.* Biofilm as a redox conductor: a systemic study of moisture and temperature dependence of its electrical properties (SI). *Phys. Chem. Chem. Phys.* 1–8 (2014) doi:10.1039/b000000x/Fig.
160. Yates, M. D. *et al.* Thermally activated long range electron transport in living

biofilms. *Phys. Chem. Chem. Phys.* **17**, 32564–32570 (2015).
161. Lampa-Pastirk, S. *et al.* Thermally activated charge transport in microbial protein nanowires - SI. *Sci. Rep.* **6**, 23517 (2016).
162. Malvankar, N. S., Yalcin, S. E., Tuominen, M. T. & Lovley, D. R. Visualization of charge propagation along individual pili proteins using ambient electrostatic force microscopy. *Nat. Nanotechnol.* **9**, 1012–1017 (2014).
163. Malvankar, N. S. *et al.* Tunable metallic-like conductivity in microbial nanowire networks. *Nat. Nanotechnol.* **6**, 573–579 (2011).
164. Gross, B. J. & El-Naggar, M. Y. A combined electrochemical and optical trapping platform for measuring single cell respiration rates at electrode interfaces. *Rev. Sci. Instrum.* **86**, 064301 (2015).
165. Kirchhofer, N. D., McCuskey, S. R., Mai, C.-K. & Bazan, G. C. Anaerobic Respiration on Self-Doped Conjugated Polyelectrolytes: Impact of Chemical Structure. *Angew. Chemie Int. Ed.* 6619–6622 (2017) doi:10.1002/anie.201701964.
166. Lu, L. *et al.* Biocidal activity of a light-absorbing fluorescent conjugated polyelectrolyte. *Langmuir* **21**, 10154–10159 (2005).
167. Steuerman, D. W. *et al.* Imaging the interfaces of conjugated polymer optoelectronic devices. *Adv. Mater.* **20**, 528–534 (2008).
168. Schaller, R. D. *et al.* The nature of interchain excitations in conjugated polymers: Spatially-varying interfacial solvatochromism of annealed MEH-PPV films studied by near-field scanning optical microscopy (NSOM). *J. Phys. Chem. B* **106**, 9496–9506 (2002).
169. Cao, D. X. *et al.* The Importance of Sulfonate to the Self-doping Mechanism of the Water-Soluble Conjugated Polyelectrolyte PCPDTBT-SO3K. *Mater. Chem. Front.* (2020) doi:10.1039/d0qm00073f.
170. Schrott, G. D., Bonanni, P. S., Robuschi, L., Esteve-Nuñez, A. & Busalmen, J. P. Electrochemical insight into the mechanism of electron transport in biofilms of Geobacter sulfurreducens. *Electrochim. Acta* **56**, 10791–10795 (2011).
171. Esteve-Núñez, A., Sosnik, J., Visconti, P. & Lovley, D. R. Fluorescent properties of c-type cytochromes reveal their potential role as an extracytoplasmic electron sink in Geobacter sulfurreducens. *Environ. Microbiol.* **10**, 497–505 (2008).
172. Bonanni, P. S., Schrott, G. D., Robuschi, L. & Busalmen, J. P. Charge accumulation and electron transfer kinetics in Geobacter sulfurreducens biofilms. *Energy Environ. Sci.* **5**, 6188 (2012).
173. Bond, D. R. & Lovley, D. R. Electricity Production by Geobacter sulfurreducens Attached to Electrodes. *Appl. Environ. Microbiol.* **69**, 1548–1555 (2003).
174. Hoskins, C., Cuschieri, A. & Wang, L. The cytotoxicity of polycationic iron oxide nanoparticles : Common endpoint assays and alternative approaches for improved understanding of cellular response mechanism. *J. Nanobiotechnology* **10**, 1–11 (2012).
175. Liu, S. *et al.* Antibacterial action of dispersed single-walled carbon nanotubes on Escherichia coli and Bacillus subtilis investigated by atomic force microscopy. *Nanoscale* **2**, 2744–2750 (2010).
176. Reid, O. G., Munechika, K. & Ginger, D. S. Space Charge Limited Current Measurements on Conjugated Polymer Films using Conductive Atomic Force Microscopy. *Nano Lett.* **8**, 1602–1609 (2008).

177. ATCC medium: 1957 Geobacter medium. *American Type Culture Collection* 1–2 http://www.atcc.org/~/media/571F8EAEE87745E5B7AED501737748D2.ashx (2013).
178. Bressloff, N. W. Multi-Objective Design of a Biodegradable Coronary Artery Stent. in *Cardiovascular and Cardiac Therapeutic Devices* (ed. Franz, T.) 1–28 (Springer, 2014). doi:10.1007/978-3-642-53836-0.
179. van der Pauw, L. J. A method of measuring the resistivity and hall coefficient of discs of arbitrary shape. *Philips Res. Reports* **13**, 1–9 (1958).

Chapter 7 − Appendix

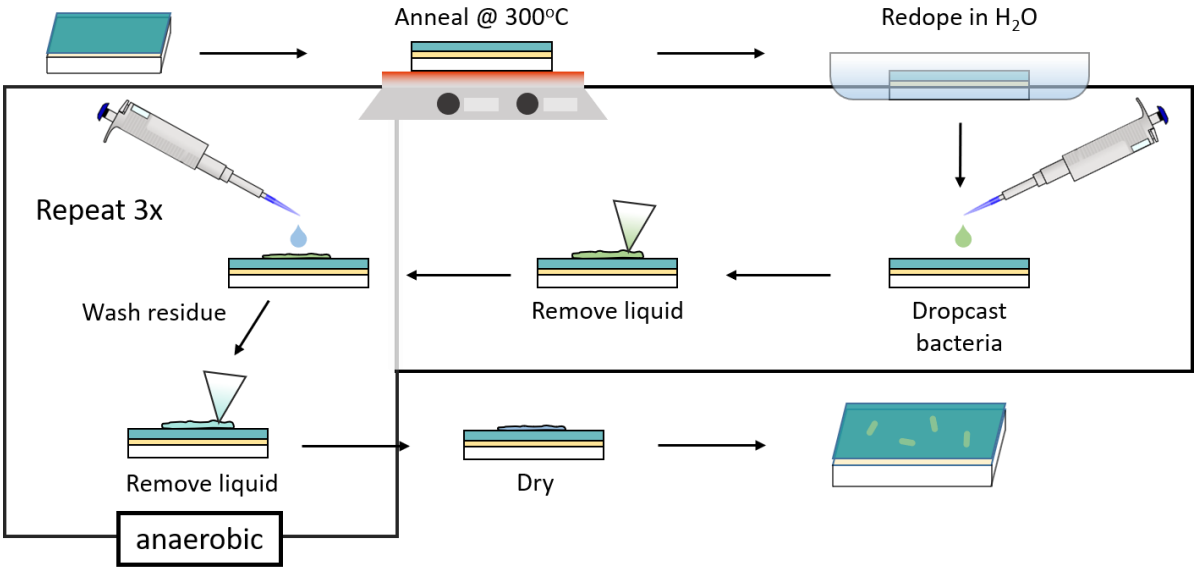

Figure 7-1. Schematic for preparation of *G. sulfurreducens* CPE-K sample